Vol. 2 No. 2 (2022): ENP Engineering Science Journal

DOI: https://doi.org/10.53907/enpesj.v2i2

ENP Engineering Science Journal, Vol. 2, No. 2, December, 2022

A review of Stall Delay Models and their Application on Hybrid Methods

Mohamed Nadjib Hamlaoui, Arezki Smaili, and Hachimi Fellouah

Abstract—This paper is a review on the stall delay phenomenon that Horizontal Axis Wind Turbines (HAWT) encounter under typical flow conditions and its numerical modelling. Aerodynamic performance predictions of HAWT have been often carried out through Computational Fluid Dynamics method with the combination of the concept of actuator disk i.e. hybrid method. For this purpose, the hybrid method is presented in details together with the numerical modelling of such stall delay phenomenon. Despite modern wind turbines are equipped with sophisticated control systems for avoiding stall, nevertheless, stall is still inevitable in the near root region of the rotor blade. This paper focuses on recent research development materials which have been undertaken on the stall delay phenomenon where the engineering models (stall delay models) of the literature being presented and criticized based on the predictions obtained from the NREL Phase VI wind turbine experiments.

***Keywords*—Actuator disk, Horizontal Axis Wind Turbine, Stall delay, Hybrid method**

NOMENCLATURE

HAWT	Horizontal Axis Wind Turbine.
CFD	Computational Fluid Dynamics.
ADM	Actuator Disk Method.
SDM	Stall Delay Models.
B	Number of blades.
c	Local chord.
r	Local radius.
α	Angle of attack.
β	Twist angle.
ϕ	Flow angle.
θ_p	Pitch angle.
Ω	Rotational speed.
U_∞	Free stream velocity (m/s).
a	Axial induction factor.
a'	Tangential induction factor.
Q	Mechanical torque (N.m).
T_h	Thrust force (N).
F	Tip loss correction factor.
C_l, C_d	The corrected lift and drag coefficients.
C_n, C_t	Normal and tangential force coefficients.

I. INTRODUCTION

The rapid drop of wind energy cost has provided motivation for manufacturers and researchers to conduct several research on Horizontal Axis Wind Turbines (HAWTs) optimization and performance predictions [1]. For HAWTs optimization and performance predictions, the actuator disk concept used for the first time by Rankine [2] and Froude [3] is one of the widely used approaches. It consists of permeable surface, instead of the real geometry, on which the rotor exerted forces act upon the incoming flow providing pressure jump and discontinuities on the flow field properties [4].

The computational application of the actuator disk concept has been used, at first, in its analytical approaches such as the Blade Element Momentum (BEM) method. It is the combination of the Blade Element (BE) and the momentum theories where it has been used for the first time by Glauert [5]. Many wind turbines design companies use codes to predict the aerodynamic performances of Horizontal Axis Wind Turbines (HAWT). These codes are usually based on the BEM method. For HAWTs design, Vaz et al. [6] proposed an extension of the BEM method to take into account the influence of the wake on the rotor plane in the general form. Dai et al. [7] coupled the BEM method with a modified Dynamic Stall (DS) model in which some influence factors such as wind shear, tower and blade vibration are considered in order to calculate the aerodynamic loads for large scale HAWT. Monteiro et al. [8] have conducted wind tunnel measurements for 1.2 m diameter HAWT and compared the experimental data with two well-known design codes of WT_Perf and Qblade which are based on the BEM method, a pretty encouraging predictions have been recorded. Yang et al. [9] have used the airfoil characteristics, extracted from full Computational Fluid Dynamics (CFD) calculation method, in the BEM method where good agreement have been found compared with the measured data. Sun et al. [10] proposed an improvement for the BEM method where both the influences from wake rotation and radial flow have been considered yielding new BEM relations for Glauert's and Shen's tip loss correction; also, the correction of Spera has been extended for the new BEM for large thrust coefficient where good agreement has been obtained against the MEXICO measurements. Dehouk et al. [11] used the BEM method to optimize the HAWT blade profile for specific initial condition of 7 m/s where new empirical relation for the chord distribution over the blade span has been proposed.

Manuscript received November 1, 2021; revised November 14, 2022.

M. N. Hamlaoui is with University of Ferhat Abbas, Setif 1, Algeria. (e-mail: mohammed_nadjib.hamlaoui@g.enp.edu.dz).
A. Smail is with the Mechanical Engineering Department, Ecole Nationale Polytechnique, Algiers, ALGERIA. (e-mail: arezki.smaili@g.enp.edu.dz).
H. Fellouah is with the Mechanical Engineering Department, University of Sherbrooke, Quebec, Canada. (e-mail: Hachimi.Fellouah@usherbrooke.ca).

Digital Object Identifier (DOI): 10.53907/enpesj.v2i2.65

With the development of CFD techniques and effective calculation hardwares, the Actuator Disk Method (ADM) has been used by combining the BE theory with 3D Navier-Stokes equations in a CFD solver where the forces have been inserted as sink in the momentum equation. Sørensen et al. [12–14] have been the first to use the actuator disk concept where the blade forces are computed through the blade element approach. Masson et al. [15, 16] used the ADM to investigate, at first, the tower-shadow impacts on HAWT and then studied the unsteady flow phenomena around the rotor operating on an Atmospheric Boundary Layer (ABL) flow. Based on the last approach, later, authors works on the nacelle anemometry of typical HAWT rotors have been reported [17–19]. Mainly, they tackled the impact of rotor aerodynamic key parameters upon the flow features within the nacelle region, especially, around the anemometer location. Alinot et al. [20] presented numerical method, based on the ADM, for predicting the ABL flow under stratified and neutral conditions where they proposed original expression for one of the closure coefficients related to the buoyancy production term of the k-ϵ turbulence model. Ameur et al. [21] used the 2D and 3D ADM computations in order to study the wind rotor/nacelle interaction in a neutral ABL flow, they found that for complex nacelle geometries the 3D ADM computations are required. Tata et al. [22] also performed a simulation study on nacelle anemometer using the ADM approach, with the emphasis on the effect of grid topology upon numerical predictions accuracy. Recently, Amini et al. [24] proposed modifications of Snel et al. [25] stall delay model empirical coefficients than studied the effect of the proposed modifications on the MEXICO rotor using the ADM implemented in OpenFOAM where a certain improvements has been noticed. Nevertheless, important discrepancies are still recorded for the loads prediction and no validation using another HAWT type has been carried out. Furthermore, notice that two different actuator approaches have been developed based on the ADM, Sørensen et al. [26] proposed the Actuator Line Method (ALM), while, Massouh et al. [27] proposed the Actuator Surface Method (ASM). Through comparison between the ALM and the ASM, Nathan [28] concluded that an ADM would be much better and less expensive approach for HAWT performance predictions; Because in the ADM, the computed forces are inserted directly in the mesh cell center unlike the ALM and the ASM approaches where the forces distribution projection is required providing different velocity distributions downstream from the rotor which could lead to unrealistic numerical solutions.

For specific flows corresponding to an attached flow regimes, the hybrid method provides reliable and consistent performance and wake predictions of HAWT rotors. Nevertheless, for high incoming wind speeds stall occurs (stall conditions) and such method breakdown due to the appearance of the effect of rotation (stall delay). It is, mainly, based on the airfoil characteristics extracted from wind tunnel measurements for a non-rotating blade along the calculation process. Nevertheless, in real flows and for typical incoming wind speeds stall occurs and the effect of rotation appears leading to the performances under-prediction. Himmelskamp [29] have been the first to record the aerodynamic loads increase through a qualitative analysis on a propeller blades, they postulated that this phenomenon is due to the centrifugal and Coriolis forces appearance. Banks and Gadd [30], Wood [31], Du and Selig [32] and Chaviaropoulos and Hansen [33] concluded that, for a rotating blade, the centrifugal and Coriolis forces appear causing an alleviation of the adverse pressure gradient acting on the boundary layer; as a results, delaying the separation point. McCroskey [34] and Madsen and Rasmussen [35] suggest that the centrifugal and Coriolis forces acting on the separated flow region, create radial pressure gradient which move the mass flow outboard comparing the process as a centrifugal pumping. Narramore and Vermeland [36] carried out a CFD analysis on a helicopter blade, they concluded that the angle of attack in which the separation point begins to stall is much higher in rotation compared to the stationary case. Through a CFD analysis of a rotating and a stationary blade, Shen et al. [37] showed that the effect of rotation causes a pressure change in the separated region with no influence on the separation point location. Snel et al. [25] and Lindenburg [38] proposed, later, correction models for the 2D lift coefficient where it has been shown that the dominant cause of the stall delay is the reduction of the adverse pressure due to centrifugal forces appearance. Through an experimental study of the turbulence effects on the stall delay phenomenon, Sicot et al. [39] concluded that the free stream turbulence is the primary cause of the delay of the boundary layer separation where the rotation have no influence. Dumitrescu and Cardoş [40] have been the first to call the phenomenon "stall delay" by suggesting that the Coriolis forces causes the movement of the separation point toward the trailing edge in rotation.

The effect of rotation causes the lift increase in the separated flow region of the rotor blade; however, its effect on the drag coefficient is still unknown where two different results have been presented in the literature. Du and Selig [32] suggested that the drag force decreases in the blade region when the effect of rotation is present. Corten [41] based his analysis on the Navier-Stokes equations for non-inertial boundary layer, he noted that the flow-separation point moves toward the trailing edge which reduces the blade wake and leads to a reduced sectional drag force. Nevertheless, Chaviaropoulos and Hansen and Sørensen [33, 42] suggested an increase of the drag force on a rotating blade. Based on full CFD study, Guntur [43] found that there is a slight increase of the drag coefficient between the 2D and the 3D cases; consequently, he assumed that there is no variation of the drag coefficient in a rotational case.

The aim of this paper consists on performing a review on the stall delay phenomenon where it has been discussed and detailed. Also, the proposed engineering models, presented in the literature, have been presented then criticized based on the predictions obtained from the mostly well-known NREL Phase VI wind turbine experiments.

II. THE BEM METHOD

The BEM is 1D analytical method as shown in Fig. 1, based on the combination of the BE and the momentum theories, used for HAWT performance predictions. For typical HAWT of B number of blades, local chord c, local radius r, twist angle β, pitch angle θ_p and rotational speed Ω subjected to a wind speed U_∞, the algorithm defining this method can be summarized as follows:

1. Initialize the axial and tangential induction factors a and a$'$, typically a=a$'$=0.
2. Compute the flow angle ϕ using Eq. (1).

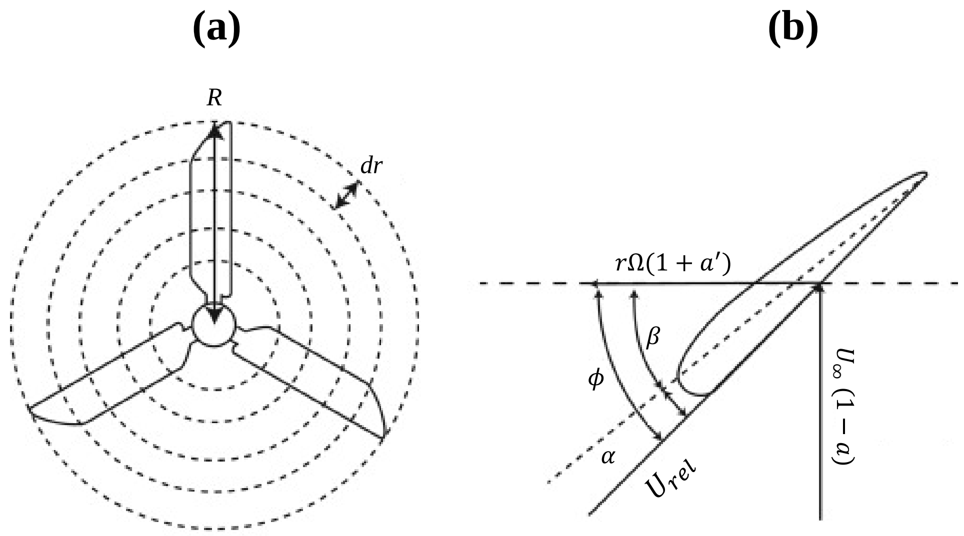

Fig. 1: BEM concept.

3. Compute the Angle of Attack (AoA) α using Eq. (2).
4. Read $C_l(\alpha)$ and $C_d(\alpha)$ from table look-up.
5. Compute the normal and tangential coefficients C_n and C_t from Eq. (3) respectively.
6. Calculate a and a$^{'}$ from Eq. (4) and Eq (5).
7. If a and a$^{'}$ has changed more than a certain tolerance, go to step (2) or else finish.
8. Compute the local loads at each blade segment, torque Q and thrust T from Eq. (6).

$$\phi = \arctan(\frac{(1-a)U_\infty}{(1+a^{'})\Omega r}) \tag{1}$$

$$\alpha = \phi - (\beta + \theta_p) \tag{2}$$

$$\begin{cases} C_n = C_l\cos(\phi) + C_d\sin(\phi) \\ C_t = C_l\sin(\phi) - C_d\cos(\phi) \end{cases} \tag{3}$$

$$a = \begin{cases} \frac{\sigma C_n}{4F\sin^2(\phi)+\sigma C_n} & if \;\; a < a_c = 0.2 \\ \frac{1(2+K(1-2a_c))-\sqrt{(K(1-2a_c)+2)^2+4(Ka_c^2-1))}}{2} & otherwise \end{cases} \tag{4}$$

where $K = \frac{2F\sin^2(\phi)}{\sigma C_n}$

$$a^{'} = \frac{\sigma C_t}{4F\sin(\phi)\cos(\phi) - \sigma C_t} \tag{5}$$

$$\begin{cases} dF_n = \frac{1}{2}\rho B\frac{U_\infty^2(1-a)^2}{\sin^2(\phi)}C_n c dr \\ dF_t = \frac{1}{2}\rho B\frac{U_\infty(1-a)\Omega r(1+a^{'})}{\sin(\phi)\cos(\phi)}C_t c dr \\ T_h = \sum_1^n dF_n \\ Q = \sum_1^n dF_t \times r \end{cases} \tag{6}$$

A. *Stall delay models*

To obtain accurate sectional aerodynamic characteristics and loads predictions, the 2D airfoil data needs to be corrected to take into account the effect of rotation. Owing to the complexity of the rotational augmentation effects, several researchers tried to model and to explain this problem with different approaches by proposing several solutions based on different assumptions. Some models were based in theoretical analyses [32,38] while the other models were developed empirically from experimental measurements [40,44].

Snel et al. [25] have been the first to propose a simple model based on the ratio of the local chord to the local radius in order to correct the 2D airfoil data to take into account the 3D effect. Many stall delay models have been developed later where Du and Selig [32] proposed a model for the drag and the lift coefficients correction which include a modified tip speed ratio, the local chord, the local radial station and empirical factors. Chaviaropoulos and Hansen [33] proposed corrections for both the 2D lift and drag coefficients which depends on the local blade twist angle, the local chord, the local radial span wise position and several empirical coefficients. Dumitrescu and Cardoş [40] developed a stall delay model, having an exponential form, which depends on the local chord and the local radial position. Corrigan and Schillings [44] developed an empirical model rooted on experimental helicopter data and simplified boundary-layer equations. Lindenburg [38] proposed a model, for the lift coefficient correction, rooted on the centrifugal forces and the radial flow modeling; mainly, it depends on the local chord, local radial ratio and a modified tip speed ratio. To get (3D) airfoil characteristics, Bak et al. [45] corrected the pressure difference between a rotating and a non rotating blade at each radial station of the rotor blade. Eggers et al. [46] developed their model by relying the axial, angular induction factors and the tip speed ratio. Breton et al. [49] conducted deep study of six well-knowns stall delay models presented on literature through the NREL Phase VI HAWT measurements, they found that none of the presented approaches are able to reproduce correctly the rotational augmentation phenomenon due to the lack of generality. It means that the proposed solutions are still incomplete and unable to explain and model adequately the present phenomenon.

The rotational augmentation effect is still an unknown phenomenon, several researchers tried to model and to explain this problem with different approaches by proposing several solutions based on different assumptions. Some models were based on theoretical analyses [32, 38] while the other models were developed empirically from experimental measurements [40, 44]. The mostly used and well-known stall delay models have been used and expressed as follows:

$$C_l = C_{l,2d} + f_l \Delta C_l \tag{7}$$

$$C_d = C_{d,2d} + f_d \Delta C_d \tag{8}$$

where the specific functions f_l and f_d represent, respectively, the variation of the lift and the drag coefficients. $\Delta C_l = C_{l,inviscid} - C_{l,2d}$. The inviscid lift coefficient $C_{l,inviscid} = 2\pi(\alpha - \alpha_0)$, α_0 is the AoA at the zero lift coefficient and $C_{l,2d}$ is the 2D lift coefficient. $\Delta C_d = C_{d,2d} - C_{d,0}$ is the difference between the 2D drag coefficient and the drag coefficient at zero AoA.

In the present study, the mostly well-knowns correction models of Snel et al. [25] and Du and Selig [32] have been used.

Recently, Hamlaoui et al. [48] have proposed a new model for the lift coefficient correction based on the shift parameter expressed as follows

$$Cl = C_{l,2d}(1 + f_s) \tag{9a}$$

$$f_s = a\exp(-(\frac{\alpha - \alpha_s}{d})^2) \tag{9b}$$

Where a, α_s and d are constants which represent the amplitude, the specific AoA that corresponds to the peak (delayed stall angle) and the controlling peak width respectively. The constants a, α_s and d appropriate to the model are equal, respectively, to 1.45, 0.575 (33°), 0.28 (16°) for radial positions $r/R \leq 0.30$ and 0.55, 0.38 (22°), 0.12 (6.88°) for radial positions $r/R > 0.30$.

III. Application of Stall Delay models to the NREL Phase VI wind turbine

Fig. 2 shows the predicted results, extracted from the work of Hamlaoui et al. [48], of the stall delay models of Snel et al. [25], Du and Selig [32] and Hamlaoui et al. [48] compared with those of data fields. It can be seen that the predicted power, using the new proposed model, agree well with the measured data in contrary to those of both Du and Selig [32] and Snel et al. [25] models where it can be noticed that for free stream velocities lower than 16 m/s, all the models provide good predictions. However, for free stream velocities higher than 16 m/s, significant over-estimations have been provided using the models of both Du and Selig [32] and Snel et al. [25] in contrary to the new proposed model of Hamlaoui et al. [48] which provides good predictions.

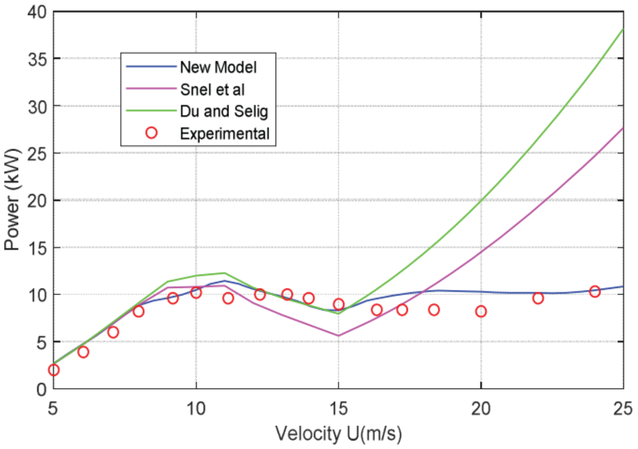

Fig. 2: Power curve: Comparison of the stall delay model predictions with the experimental data [48].

IV. Conclusion

The purpose of the present work is a review of the stall delay phenomenon, mostly encountered during HAWT operations, and its modeling using hybrid methods i.e. ADM. Firstly, the hybrid methods have been introduced where mainly their limitations have been tackled. Secondly, the stall delay phenomenon has been detailed and the mostly well-known engineering models (stall delay models) presented in the literature have been presented then criticized based on the predictions obtained from the NREL Phase VI wind turbine experiments. It has been found, from the work of Hamlaoui et al. [48], that the existing stall delay models fail to predict the aerodynamic performances of the NREL Phase VI wind turbine, for high incoming wind speeds, due to their lack of generality; the new model of Hamlaoui et al. [48] has shown good predictions and more realistic modeling of the stall delay phenomenon compared to the existing models.

References

[1] M. Hansen, Aerodynamics of Wind Turbines: Second edition, Earthscan, 2008.

[2] W. J. M. Rankine, On the mechanical principles of the action of propellers, Transactions of the Institution of Naval Architects, 1865, pp. 6.

[3] R.E. Froude, On the part played in propulsion by differences of fluid pressure, *Transactions of the Institution of Naval Architects 30*, pp. 390, 1889.

[4] J.H. Horlock, Actuator disk theory-discontinuities in thermo-fluid dynamics, McGraw-Hill International Book Co, NewYork, 1978, pp. 256.

[5] H. Glauert, Airplane propellers, *Aerodynamic theory. Springer*, 1935, pp. 169–360.

[6] J.R.P. Vaz, J.T. Pinho & A.L.A. Mesquita. An extension of bem method applied to horizontal-axis wind turbine design. "*Renewable Energy*", vol. 36, pp. 1734 – 1740, 2010, doi:https://doi.org/10.1016/j.renene.2010.11.018.

[7] J. Dai, Y. P. Hu, D. S. Liu & X. Long, Aerodynamic loads calculation and analysis for large scale wind turbine based on combining bem modified theory with dynamic stall model, "*Renewable Energy*", vol. 36, pp. 1095 – 1104, 2011, doi:https://doi.org/10.1016/j.renene.2010.08.024.

[8] J.P. Monteiro, M. R. Silvestre, H. Piggott & J. C. Andre, Wind tunnel testing of a horizontal axis wind turbine rotor and comparison with simulations from two blade element momentum codes, "*Journal of Wind Engineering and Industrial Aerodynamics*", vol. 123, pp. 99 – 106, 2013, doi:https://doi.org/10.1016/j.jweia.2013.09.008.

[9] H. Yang, W. Shen, H. Xu, Z. Hong & C. Liu, Prediction of the wind turbine performance by using bem with airfoil data extracted from cfd. "*Renewable Energy*", vol. 70, pp. 107 – 115, 2016, doi:https://doi.org/10.1016/j.renene.2014.05.002.

[10] Z. Sun, J. Chen, W. Z. Shen & W. J. Zhu, Improved blade element momentum theory for wind turbine aerodynamic computations, "*Renewable Energy*", vol. 96, pp. 824 – 831, 2016, doi:https://doi.org/10.1016/j.renene.2016.05.035.

[11] V. Dehouck, M. Lateb, J. Sacheau & H. Fellouah, Application of the blade element momentum theory to design horizontal axis wind turbine blades, "*Journal of Solar Energy Engineering*", vol. 140, 2018.

[12] J.N. Sørensen & A. Myken, Unsteady actuator disc model for horizontal axis wind turbines. "*Journal of Wind Engineering and Industrial Aerodynamics*", vol. 39, pp. 139–149, 1992.

[13] J.N. Sørensen & C. W. Kock, A model for unsteady rotor aerodynamics. "*Journal of Wind Engineering and Industrial Aerodynamics*", vol. 58, pp. 259–275, 1995.

[14] J.N. Sørensen, W.Z. Shen & X. Munduate, analysis of wake states by a full-field actuator disc model. "*Wind Engergy*", vol. 1, pp. 73–88, 1998.

[15] C. Masson, A. Smaili, I. Ammara & C. Leclerc, Aerodynamic investigations on tower-shadow impacts for hawts, "*Proceedings of the ASME Wind Energy Symposium, AIAA*", 2000, doi:10.2514/6.2000-41.

[16] C. Masson, A. Smaili & C. Leclerc, Aerodynamic analysis of hawts operating in unsteady conditions, "*Wind Energy*", vol. 4, pp. 1–22,2001.

[17] A. Smaili, C. Masson, Numerical Investigations of Nacelle Anemometry for Horizontal Axis Wind Turbines, "*Wind Energy Symposium*", pp. 389–398, 2003, doi:10.1115/WIND2003-1185.

[18] A. Smaili, C. Masson, On the rotor effects upon nacelle anemometry for windturbines, "*Wind Engineering*", vol. 28, pp. 695–713, 2004, doi:10.1260/0309524043729958.

[19] C. Masson, A. Smaili, Numerical study of turbulent flow around a wind turbine nacelle, "*Wind Energy*", vol. 9, pp. 281–298, 2006, doi:10.1002/we.171.

[20] C. Alinot & C. Masson, k-epsilon model for the atmospheric boundary layer under various thermal stratifications, "*Journal of Solar Energy Engineering*", vol. 127, pp. 438–443, 2005, doi:10.1115/1.2035704.

[21] K. Ameur, C. Masson & P. J. Eecen, 2d and 3d numerical simulation of the wind-rotor/nacelle interaction in an atmospheric boundary layer, "*Journal of Wind Engineering and Industrial Aerodynamics*", vol. 99, pp. 833 – 844, 2011, doi:https://doi.org/10.1016/j.jweia.2011.06.002.

[22] M. Tata, A. Smaili & C. Masson, Effect of grid topology on numerical simulations of flow fields around wind turbine nacelle anemometer, "*Journal of Applied Fluid Mechanics*" vol. 11, pp. 1569–1578,2018.

[23] J.N. Sørensen, K. Nilsson, S. Ivanell, H. Asmuth & R. F. Mikkelsen, Analytical body forces in numerical actuator disc model of wind turbines, "*Renewable Energy*", vol. 147, pp. 2259 – 2271, 2020, doi:https://doi.org/10.1016/j.renene.2019.09.134.

[24] S. Amini, M. R. Golzarian, E. Mahmoodi, A. Jeromin & M.H. Abbaspour-Fard, Numerical simulation of the mexico wind turbine using the actuator disk model along with the 3d correction of aerodynamic coefficients in openfoam, "*Renewable Energy*", vol. 163, pp. 2029 – 2036, 2020, doi:https://doi.org/10.1016/j.renene.2020.10.120.

[25] H. Snel, R. Houwink, & J. Bosschers, Sectional prediction of lift coefficients on rotating wind turbine blades in stall, "*Netherlands Energy Research Foundation Petten*", Netherlands, 1995.

[26] J.N. Sørensen & W. Z. Shen, Numerical modeling of wind turbine wakes, "*J. Fluids Eng*", vol. 124, pp.393–399, 2002.

[27] F. Massouh, I. Dobrev & M. Rapin, Numerical simulation of wind turbine performance using a hybrid model, "*44th AIAA Aerospace Sciences Meeting and Exhibit*", p. 782, 2006.

[28] J. Nathan (Ph.D. Dissertation), Application of actuator surface concept in LES simulations of the near wake of wind turbines, École de technologie supérieure, Quebec, Canada, 2018.

[29] H. Himmelskamp, Profile Investigations on a Rotating Airscrew, MAP, 1947, URL:https://books.google.dz/books?id=VlK3tgAACAAJ.

[30] W. Banks & G. Gadd, Delaying effect of rotation on laminar separation, "*AIAA journal*", vol. 1, pp. 941–941, 1963.

[31] D. Wood, A three-dimensional analysis of stall-delay on a horizontal-axis wind turbine, "*Journal of wind engineering and Industrial aerodynamics*", vol. 37, pp. 1–14, 1991.

[32] Z. Du & M. Selig, A 3-d stall-delay model for horizontal axis wind turbine performance prediction, "*ASME Wind Energy Symposium*", pp. 21, 1998.

[33] P. Chaviaropoulos & M.O. Hansen, Investigating three-dimensional and rotational effects on wind turbine blades by means of a quasi 3d navier-stokes solver. "*Journal of Fluids Engineering*", vol. 122, pp. 330–336,2000.

[34] W.J. McCroskey, Measurements of boundary layer transition, separation and streamline direction on rotating blades, pp. 6321, 1971.

[35] H.A. Madsen & F. Rasmussen, Derivation of three-dimensional airfoil data on the basis of experiment and theory, "*Proceedings Wind power*", pp. 166–174, 1988.

[36] J. Narramore & R. Vermeland, Navier-stokes calculations of inboard stall delay dueto rotation, "*Journal of Aircraft*", vol. 29, pp. 73–78, 1992.

[37] W.Z. Shen & J.N. Sørensen, Quasi-3d navier–stokes model for a rotating airfoil, "*Journal of Computational Physics*", vol. 150, pp. 518–548, 1999.

[38] C. Lindenburg, Modelling of rotational augmentation based on engineering considerations and measurements, "*European Wind Energy Conference*", London, pp.22–25, 2004.

[39] C. Sicot, P. Devinant, S. Loyer & J. Hureau, Rotational and turbulence effects on a wind turbine blade, investigation of the stall mechanisms, "*Journal of Wind Engineering and Industrial Aerodynamics*", vol. 96, pp. 1320–1331, 2008.

[40] H. Dumitrescu, V. Cardoş & A. Dumitrache, Modelling of inboard stall delay dueto rotation, "*Journal of Physics: Conference Series, IOP Publishing*", pp. 012022, 2007.

[41] G.P. Corten (Ph.D. Dissertation), Flow separation on wind turbines blades, University of Utrecht, Rotterdam, Netherlands, 2001.

[42] N. Sørensen, Evaluation of 3d effects from 3d cfd computations, "*IEA JointAction Committee on Aerodynamics Annex IV Aero Experts meeting*", 2000.

[43] S. Guntur (Ph.D. Dissertation), A detailed study of the rotational augmentation and dynamic stall phenomena for wind turbines, DTU Wind Energy, Denmark, 2013.

[44] J.J. Corrigan & J. Schillings, Empirical model for stall delay due to rotation, "*American Helicopter Society Aero-mechanics Specialists Conference*", San Francisco, CA, 1994.

[45] C. Bak, J. Johansen & P. B. Andersen, Three-dimensional corrections of airfoil characteristics based on pressure distributions, "*Proceedings of the European Wind Energy Conference*", pp. 1–10, 2006.

[46] A. Eggers, K. Chaney & R. Digumarthi, An assessment of approximate modeling of aerodynamic loads on the uae rotor, "*ASME Wind Energy Symposium*", American Society of Mechanical Engineers, pp. 283–292, 2003.

[47] S.P. Breton, F. N. Coton & G. Moe, A study on rotational effects and different stall delay models using a prescribed wake vortex scheme and NREL Phase VI experiment data. "*Wind Energy: An International Journal for Progress and Applications in Wind Power Conversion Technology*", vol. 11, pp. 459–482, 2003.

[48] M.N. Hamlaoui, A. Smaili & H. Fellouah, Improved bem method for hawt performance predictions, "*International Conference on Wind Energy and Applications in Algeria (ICWEAA), IEEE*", pp. 1–6, 2018.

[49] S.P. Breton, F.N. Coton & G. Moe, A study on rotational effects and different stall delay models using a prescribed wake vortex scheme and nrel phase vi experiment data. "*Wind Energy: An International Journal for Progress and Applications in Wind Power Conversion Technology*", vol. 11, pp. 459–482, 2003.

Mohamed Nadjib Hamlaoui is an assistant professor of Mechanical Engineering at University of Ferhat Abbas, Setif 1. He received his M.S. in Energy Mechanics from the Ecole Nationale Polytechnique of Algiers in 2016, and his PhD in Mechanical Engineering (major in: Clean and Renewable Energies-Mechanical Systems) in 2021. He joined, recently, the University of Ferhat Abbas, Setif 1 in 2021. His research field deals with the different methodologies applied for the aerodynamic performance predictions of horizontal axis wind turbines and wind farms optimization.

Arezki Smaili is a Professor of Mechanical Engineering and Director of Research Laboratory of Mechanical Engineering (Laboratoire de ‘’Génie Mécanique et Développement-LGMD”, at Ecole Nationale Polytechnique (ENP), Algiers. He received his engineer diploma in Mechanical Engineering from University of Sciences and Technologies Houari Boumediene (USTHB), Algiers in 1988, M.S. in Mechanical Engineering from Laval University, Québec (Canada) in 1991, and his PhD in Energy Sciences from University of Québec (Canada) in 1998. He joined the ENP in 2006. He was formerly research scientist at “Ecole de Technologie Supérieure”, Montreal (Canada). He has been involved with wide range of energy conversion applications, particularly in the area of thermal analysis of clean and renewable energy systems and aerodynamics of wind turbines since the 1992.

Hachimi Fellouah is with University of Sherbrooke, Quebec, Canada as full professor since 2021. In 2005, he defended his PhD thesis at University of Nantes, France. He has been a postdoctoral fellow with Queen’s University at Kingston. Canada, from 2007 to 2010. He has been an associate professor from 2015 to 2021 and an assistant professor from 2010 to 2015 at University of Sherbrooke, Quebec, Canada. His research interests are in are fluid mechanics, wind and solar energy, clean technologies and Heat transfer.

Speed estimation of a Doubly Fed Induction Machine controlled by a Field Oriented Control Strategy

Tahar Djellouli and Mohamed Seghir Boucherit

Abstract−This paper studies the estimation problem of speed in a Doubly Fed Induction Machine (DFIM) controlled by a Field Oriented Control (FOC) Strategy. The DFIM is the most responsive in variable speed. The chosen configuration uses two voltage inverters connected to the stator and rotor windings, to adopt the power distribution between them through the pulses distribution of the stator and the rotor in motor operating mode. It is necessary to model the DFIM in three-phase equations and then in two-phase equations faithfully representing the characteristics of the machine. From this model, we can design and simulate the control. The control by oriented rotor flux can be realized by using the speed provided by sensors or estimators. In this paper, we have used the Extended Kalman Filter (EKF) in order to avoid problems caused by the motor speed sensor and improve the robustness of the control and its performance without using any speed sensor.

***Keywords*− Doubly Fed Induction Machine, Field Oriented Control, speed sensor, voltage inverter**

NOMENCLATURE

Msr, M	Mutual inductance between a stator phase and a rotor phase, M:maximum value of the Mrs
Ls, Lr	Stator and Rotor self-inductancesrespectively
σ	dispersion coefficient (σ=1-$M^{\wedge 2}/L_sL_r$)
R_s,R_r	stator and rotor resistances.
T_s, T_r	Stator and rotor time-constants (Ts = Ls,/Rs ;Tr = Lr,/Rr)
θ_s ,θ_r	Angle tracking of the stator flux and rotor relative to the benchmark
θ	Electrical angle between the axis of the stator windings and the rotor windings
I_{ds}, I_{qs}	d-axis and q-axis component of stator current in stationary reference frame
I_{dr}, I_{qr}	d-axis and q-axis component of rotor current in stationary reference frame
V_{ds}, V_{qs}	d-axis and q-axis component of stator voltage in stationary reference frame
V_{dr}, V_{qr}	d-axis and q-axis component of rotor voltage in stationary reference frame
ω_s ,ω_r	The stator and rotor pulsation
Ω	Mechanical speed of rotor
ϕ_{ds},ϕ_{qs}	Stator flux two phase in a rotating frame
ϕ_{dr},ϕ_{qr}	Rotor flux two phase in a rotating frame
T_{em}	Electromagnetic Torque.
C_r	Load torque.
J	Total inertia.
k_f	Coefficient of friction
p	Number of pole pairs of the machine
T	Sampling time, =0.00001s

Manuscript received January 8, 2022; revised December 1, 2022.

T. Djellouli is with Ghardaia university, Ghardaia, Algeria.
(e-mail: djelloulitaha@yahoo.fr)
M. S. Boucherit with Ecole Nationale Polytechnique.
(e-mail: yassine.mahamdi@g.enp.edu.dz).

Digital Object Identifier (DOI): 10.53907/enpesj.v2i2.77

I. INTRODUCTION

The Doubly Fed Induction Machine (DFIM) presents several advantages as well as a generator mode in wind energy conversion systems, like wind-turbine or pumped storage systems, and as a motor mode in high power applications such as traction and marine propulsion [1]. The DFIM operates in motor mode and is powered by two voltage inverters, one is feeding the stator and the other is for the rotor [2] (Fig.1). The inverters are controlled by the Pulse Width Modulation (PWM) technique [3]. The control strategy proposed in this paper is a Field Oriented Control (FOC). This control strategy is applied to ensure good dynamic performance, stability and motor current decoupling in synchronous reference frame (*d*, *q*) [4]. The strategy is achieved without using any information about the rotor's position or speed.

In most cases, a mechanical sensor measures the speed. Although this requires a location installation that causes difficulties access and requires additional space that reduces reliability in harsh environments and increases the cost of the machine [5]. To remove this sensor, the most technical ones are based on estimation theory combined with the mathematical machine model. The extended Kalman filter is used to estimate the speed of the DFIM as a function of the measured stator and rotor currents and voltages. The estimated speed is used overall. The simulation results obtained by the control with speed sensor and by estimated speed are presented in a comparative table.

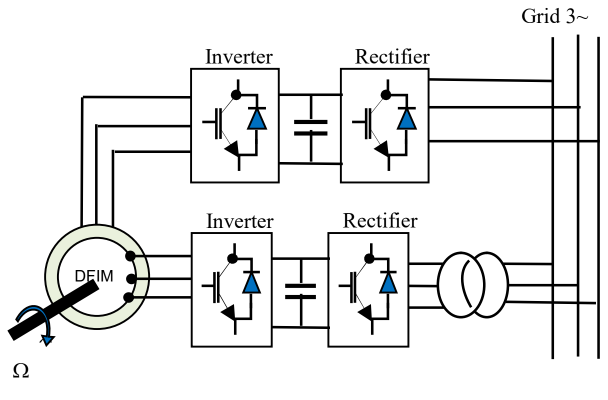

Fig. 1: General principle of a DFIM powered by two inverters.

The paper is organized as follows: Section II and III summarize the mathematical model and vector control by rotor field oriented of the DFIM with speed sensor. Section IV is devoted to estimate the rotor speed by the extended Kalman filter used in the developed strategy.

The rest of the paper is organized as follows. Section II and III summarize the mathematical model and vector control by rotor field oriented of the DFIM with speed sensor. Section IV is devoted to estimate the rotor speed by the extended Kalman filter used in the developed strategyThe last section presents the simulation results obtained by the application of the control with and without speed sensor presented in a comparative table.

II. MATHEMATICAL MACHINE MODEL

To achieve good dynamic performance in the control of a DFIM, it is necessary to have a model that faithfully represents the machine's behavior, not only in permanent regimes, but also in transient regimes.

The induction machine consists of three windings located symmetrically in the notches of stator and rotor. DFIM comprises three stator coils and three rotor coils offset by an identical distribution angle.

Vectors equations of voltages, currents and total stator and rotor fluxes are given as follow [6]:

$$\begin{cases}[V_s] = [R_s][I_s] + \frac{d}{dt}[\varphi_s] \\ [V_r] = [R_r][I_r] + \frac{d}{dt}[\varphi_r]\end{cases} \tag{1}$$

$$Where \begin{cases}[R_s] = \begin{bmatrix} R_s & 0 & 0 \\ 0 & R_s & 0 \\ 0 & 0 & R_s \end{bmatrix} \\ [R_r] = \begin{bmatrix} R_r & 0 & 0 \\ 0 & R_r & 0 \\ 0 & 0 & R_r \end{bmatrix}\end{cases} \tag{2}$$

$$\begin{cases}[V_s] = [V_{as}\ V_{bs}\ V_{cs}]^T \\ [V_r] = [V_{ar}\ V_{br}\ V_{cr}]^T \neq [0\ 0\ 0]^T\end{cases} \tag{3}$$

$$\begin{cases}[I_s] = [I_{as}\ I_{bs}\ I_{cs}]^T \\ [I_r] = [I_{ar}\ I_{br}\ I_{cr}]^T\end{cases} \tag{4}$$

$$\begin{cases}[\phi_s] = [\phi_{as}\ \phi_{bs}\ \phi_{cs}]^T \\ [\phi_r] = [\phi_{ar}\ \phi_{br}\ \phi_{cr}]^T\end{cases} \tag{5}$$

The following matrix relations give the expressions of the total fluxes through the stator and rotor windings:

$$\begin{bmatrix}[\Phi_s] \\ [\Phi_r]\end{bmatrix} = \begin{bmatrix}[L_{ss}] & [M_{sr}] \\ [M_{rs}] & [L_{rr}]\end{bmatrix}\begin{bmatrix}[I_s] \\ [I_r]\end{bmatrix} \tag{6}$$

$[M_{rs}] = [M_{sr}]^T$.

$[L_{ss}], [L_{rr}], [M_{sr}]\ and\ [M_{rs}]$ are sub-matrices of inductances given by:

$$\begin{cases}[L_{ss}] = \begin{bmatrix} L_{ss} & M_s & M_s \\ M_s & L_{ss} & M_s \\ M_s & M_s & L_{ss} \end{bmatrix} \\ [L_{rr}] = \begin{bmatrix} L_{rr} & M_r & M_r \\ M_r & L_{rr} & M_r \\ M_r & M_r & L_{rr} \end{bmatrix}\end{cases} \tag{7}$$

$$[M_{sr}] = M\begin{bmatrix} \cos\theta & \cos(\theta + \frac{2\pi}{3}) & \cos(\theta - \frac{2\pi}{3}) \\ \cos(\theta - \frac{2\pi}{3}) & \cos\theta & \cos(\theta + \frac{2\pi}{3}) \\ \cos(\theta + \frac{2\pi}{3}) & \cos(\theta - \frac{2\pi}{3}) & \cos\theta \end{bmatrix} \tag{8}$$

The modeling of the DFIM is based on the general equations in the Park transformation applied on the stator and rotor windings, these equations are resulted as following [6]:

$$\begin{cases}V_{ds} = R_s I_{ds} + \frac{d\phi_{ds}}{dt} - \omega_s \phi_{qs} \\ V_{qs} = R_s I_{qs} + \frac{d\phi_{qs}}{dt} + \omega_s \phi_{ds}\end{cases} \tag{9}$$

$$\begin{cases}V_{dr} = R_r I_{dr} + \frac{d\phi_{dr}}{dt} - \omega_r \phi_{qr} \\ V_{qr} = R_r I_{qr} + \frac{d\phi_{qr}}{dt} + \omega_r \phi_{dr}\end{cases} \tag{10}$$

$$\begin{cases}\phi_{ds} = L_s I_{ds} + M I_{dr} \\ \phi_{qs} = L_s I_{qs} + M I_{qr}\end{cases} \tag{11}$$

$$\begin{cases}\phi_{dr} = L_r I_{dr} + M I_{ds} \\ \phi_{qr} = L_r I_{qr} + M I_{qs}\end{cases} \tag{12}$$

where ω_s, ω are the stator and rotor pulsations respectively, $\omega = p\Omega$; Ω is the mechanical rotating speed.

The dynamical equation and the electromagnetic torque T_{em} are given by equations (13) and (14) respectively:

$$J\frac{d\Omega}{dt} = T_{em} - C_r - K_f.\Omega \tag{13}$$

$$T_{em} = p\frac{M}{L_r}(\phi_{dr} I_{qs} - \phi_{qr} I_{ds}) \tag{14}$$

The machine is powered directly by double three phase voltages perfect sources: as it is represented in Fig. 1.

III. FIELD ORIENTED CONTROL OF DFIM

For the Field Oriented Control (FOC) of the DFIM, it is necessary to choose a reference frame (d, q) for obvious reasons of simplifications. This technique consists of the orientation of the stator and rotor flux.

The (d) axis orientation in the direction of the stator flux is the most used in DFIM control as shown in (Fig. 2) [7,8].

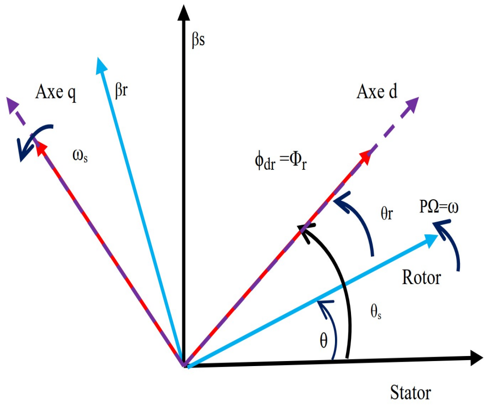

Fig. 2: DFIM axis orientation in d-q reference

The relative angular position of the (d) axis of the rotating reference d-q is given by:

$$\theta_s = \theta_r + \theta \tag{15}$$

Where,
θ_r: is the angular position relative to d axis
θ : represents the electrical angular position of the rotor relative to the stator reference frame.
With,

$$\begin{cases} \dfrac{d\theta_s}{dt} = \omega_s \\ \dfrac{d\theta}{dt} = \omega \\ \omega_s = \omega + \omega_r \end{cases} \tag{16}$$

From equations (9) and (10), and by replacing the fluxes by their values and introducing the intermediate voltages [7], we obtain the follow equations:

$$\begin{cases} V_{tds} = V_{ds} - \dfrac{M}{L_r} V_{dr} \\ V_{tdr} = V_{dr} - \dfrac{M}{L_r} V_{ds} \\ V_{tqs} = V_{qs} - \dfrac{M}{L_r} V_{qr} \\ V_{tqr} = V_{qr} - \dfrac{M}{L_r} V_{qs} \end{cases} \tag{17}$$

$$\begin{cases} V_{tds} = V_{tdsc} + V_{tdsc1} = R_s I_{ds} + \sigma L_s \dfrac{dI_{ds}}{dt} + V_{tdsc} \\ V_{tqs} = V_{tqsc} + V_{tqsc1} = R_s I_{qs} + \sigma L_s \dfrac{dI_{qs}}{dt} + V_{tqsc} \\ V_{tdr} = V_{tdrc} + V_{tdrc1} = R_r I_{dr} + \sigma L_r \dfrac{dI_{dr}}{dt} + V_{tdrc} \\ V_{tqr} = V_{tqrc} + V_{tqrc1} = R_r I_{qr} + \sigma L_r \dfrac{dI_{qr}}{dt} + V_{tqrc} \end{cases} \tag{18}$$

With: $T_s = \frac{L_s}{R_s}$; $T_r = \frac{L_r}{R_r}$.
Where: V_{tdsc1} V_{tqsc1}; V_{tdrc1}; V_{tqrc1} are compensation terms given by

$$\begin{cases} V_{tdsc1} = -\dfrac{M}{L_r} R_r I_{dr} - \omega_s \phi_{qs} + \omega_r \dfrac{M}{L_r} \emptyset_{qr} \\ V_{tqsc1} = -\dfrac{M}{L_r} R_r I_{qr} + \omega_s \phi_{ds} - \omega_r \dfrac{M}{L_r} \emptyset_{dr} \\ V_{tdrc1} = -\dfrac{M}{L_s} R_s I_{ds} + \omega_s \dfrac{M}{L_s} \phi_{qs} - \omega_r \emptyset_{qr} \\ V_{tqrc1} = -\dfrac{M}{L_s} R_s I_{qs} - \omega_s \dfrac{M}{L_s} \phi_{ds} + \omega_r \emptyset_{dr} \end{cases} \tag{19}$$

This method gives us the transfer functions between currents and voltages of the stator and the rotor respectively :

$$\begin{cases} \dfrac{I_{qs}(s)}{V_{tqsc}(s)} = \dfrac{I_{ds}(s)}{V_{tds}(s)} = \dfrac{1}{R_s + \sigma L_s . s} \\ \dfrac{I_{qr}(s)}{V_{tqrc}(s)} = \dfrac{I_{rd}(s)}{V_{tdr}(s)} = \dfrac{1}{R_r + \sigma L_r . s} \end{cases} \tag{20}$$

With s is Laplace operator.
Hence, the application of stator FOC allows us to obtain the following equation

$$\{\Phi_{dr} = \Phi_r, \ \Phi_{qr} = 0 \tag{21}$$

This choice makes it possible to write system equations as follows:

$$\begin{cases} \Phi_{dr} = \Phi_r \\ \Phi_{qr} = 0 \end{cases} \rightarrow \begin{cases} I_{qr} = -\dfrac{M}{L_r} I_{qs} \\ I_{dr} = \dfrac{V_{dr}}{R_r} \\ i_{ds} = \dfrac{1}{M}\left(\phi_r - \dfrac{L_r}{R_r} V_{dr}\right) \end{cases} \tag{22}$$

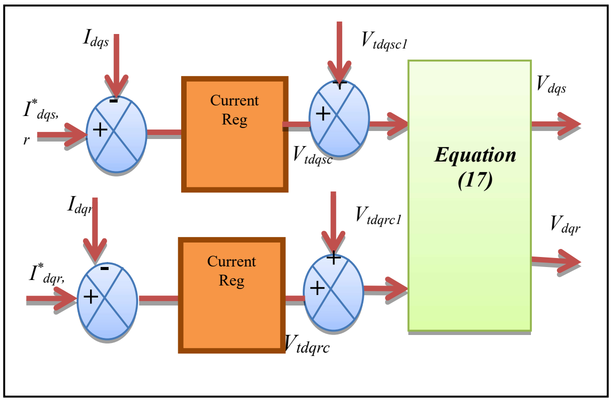

Fig. 3: Compensation terms in FOC strategy of DFIM

The different references of the currents to be regulated for an orientation of the rotor flux and unit power factor operation (with cos φ = 1) at the rotor are given by [9].

$$T^*_{em} = P \frac{M}{L_r} \phi^*_r I^*_{qs} \tag{23}$$

$$\begin{cases} I^*_{ds} = \dfrac{1}{M} \phi^*_r \quad ; \quad I^*_{dr} = \dfrac{V_{dr}}{R_r} \\ I^*_{qs} = \dfrac{L_r}{PM\phi^*_r} T^*_{em}; \ I^*_{qr} = -\dfrac{1}{P\phi^*_r} C^*_{em} \end{cases} \tag{24}$$

The stator flux depends on rotor flux.

Finally, one can summarize the vector control strategy with oriented rotor flux of the machine in the overall diagram presented in Fig. 4.

IV. ESTIMATION OF SPEED BY THE KALMAN FILTER

The position or the speed of the DFIM information on the rotor is very important in the control. It is generally obtained through a mechanical speed sensor. However, this sensor requires a place for its installation and leads to difficulties in its mounting; it is sensitive to noises and vibrations. Several strategies have been proposed in the literature to eliminate this mechanical sensor. Among these strategies, there is the estimation by the Extended Kalman Filter (EKF). This Kalman filter is an observer for a nonlinear closed-loop with a variable gain matrix. At each calculation step, this Kalman filter predicts the new values of state variables of the DFIM. The prediction of values is made by minimizing the noise effects and modeling errors of the parameters or variables state. The noises are supposed to be white, Gaussian, and not correlated with the estimated states [10].

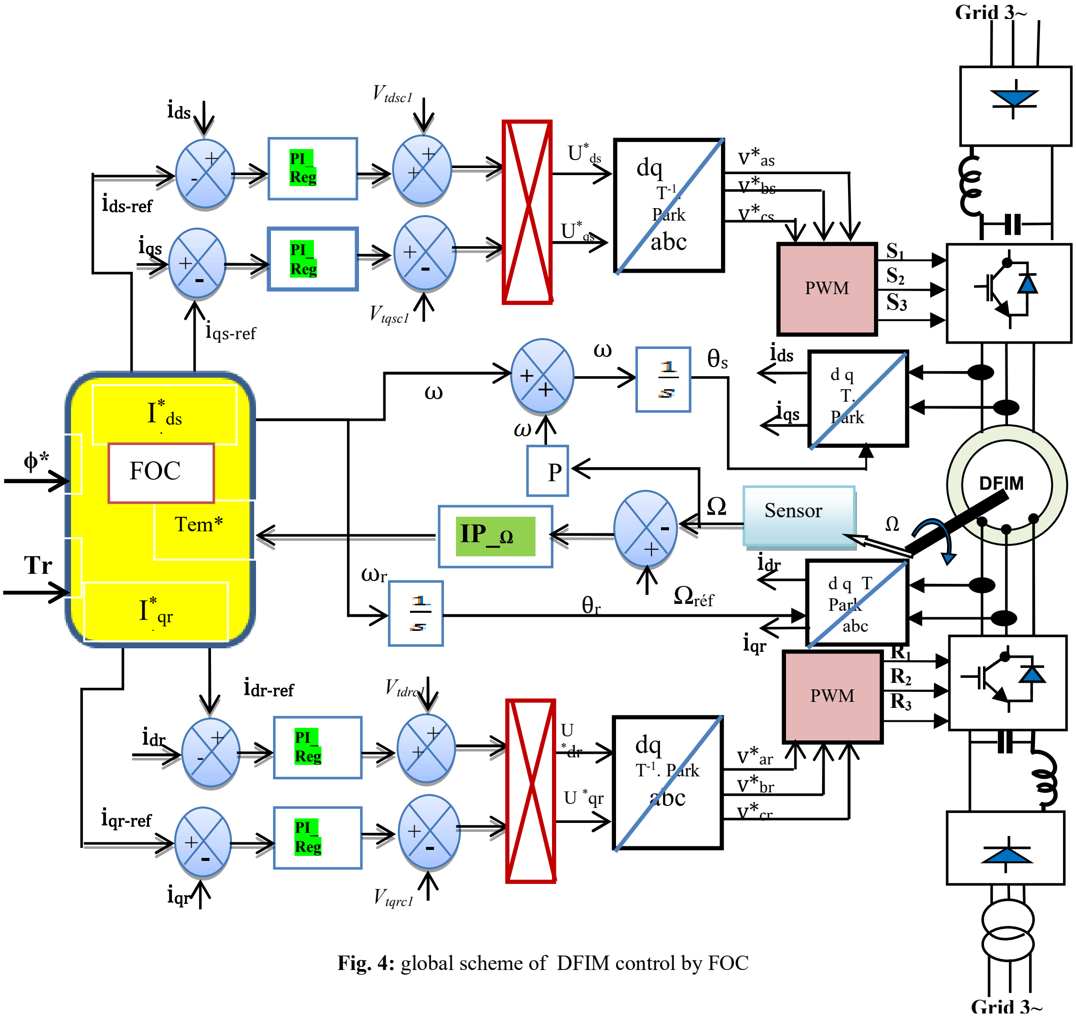

Fig. 4: global scheme of DFIM control by FOC

IV.1. SELECTION OF DFIM MODEL

The state equation of motor model is given as following [11]:

$$\dot{x} = f(x,u) = Ax + Bu \tag{25}$$

$$y = Cx \tag{26}$$

$$A = \begin{bmatrix} a_1 & a_2 p\Omega & a_3 & a_4 p\Omega & 0 \\ -a_2 p\Omega & a_1 & -a_4 p\Omega & a_3 & 0 \\ a_5 & -a_6 p\Omega & a_7 & -a_8 p\Omega & 0 \\ a_6 p\Omega & a_5 & a_8 p\Omega & a_7 & 0 \\ 0 & 0 & 0 & 0 & 0 \end{bmatrix} \tag{27}$$

$$B = \begin{bmatrix} b_1 & 0 & b_2 & 0 \\ 0 & b_1 & 0 & b_2 \\ b_2 & 0 & b_3 & 0 \\ 0 & b_2 & 0 & b_3 \\ 0 & 0 & 0 & 0 \end{bmatrix} \tag{28}$$

$$C = \begin{bmatrix} 1 & 0 & 0 & 0 & 0 \\ 0 & 1 & 0 & 0 & 0 \end{bmatrix} \tag{29}$$

Where a_i and b_i parameters are given by:

$$a_1 = -\frac{R_s}{\sigma L_s};\ a_2 = \frac{(1-\sigma)}{\sigma};\ a_3 = \frac{R_r M}{\sigma L_s L_r};\ a_4 = \frac{M}{\sigma L_s},$$
$$a_5 = \frac{R_s M}{\sigma L_s L_r};\ a_6 = \frac{-M}{\sigma L_r};\ a_7 = -\frac{R_r}{\sigma L_r};\ a_8 = \frac{1}{\sigma}.$$
$$b_1 = \frac{1}{\sigma L_s};\ b_2 = -\frac{M}{\sigma L_s L_r};\ b_3 = \frac{1}{\sigma L_r}$$

The dimension of the state vector is increased by adding the angular speed of the rotor, in this case, the angular speed of the rotor is considered in the state variable. The state vector becomes:

$$x = [i_{\alpha s}\ i_{\beta s}\ i_{\alpha r}\ i_{\beta r}\ \omega]^T \tag{30}$$

$$u = [v_{\alpha s}\ v_{\beta s}\ v_{\alpha r}\ v_{\beta r}\ ]^T \tag{31}$$

IV. 2. DISCRETIZATION OF THE MODEL

The time-discrete state space model of the DFIM model obtained from equations (25) and (26) can be written as follow [11]:

$$\begin{cases} X_{k+1} = f(k, X_k, U_k, W_k) = A_k X_k + B_k U_k + W_k \\ Y_k = h(k, X_k, V_k) = C_k X_k + V_k \end{cases} \tag{32}$$

k: represents the number of an iteration in the discrete of state equation

$W\ and\ V$ are the state noise which corresponds to the non-deterministic part the measurement noise respectively

With: $X_k = \begin{bmatrix} I_{\alpha s}(k) \\ I_{\beta s}(k) \\ I_{\alpha s}(k) \\ I_{\beta s}(k) \\ \omega(k) \end{bmatrix}$; $X_{k+1} = \begin{bmatrix} I_{\alpha s}(k+1) \\ I_{\beta s}(k+1) \\ I_{\alpha s}(k+1) \\ I_{\beta s}(k+1) \\ \omega(k+1) \end{bmatrix}$, $U_k = \begin{bmatrix} V_{\alpha s}(k) \\ V_{\beta s}(k) \\ V_{\alpha r}(k) \\ V_{\beta r}(k) \end{bmatrix}$

Where A_k, B_k and C_k are the discrete system matrix, input matrix and output matrix respectively:

$$\begin{cases} A_k = \mathrm{I} + T.A \\ B_k = \mathrm{T.B} \\ C_k = \mathrm{C} \end{cases} \tag{33}$$

In the equation (33), T and I are the sampling time and the identity matrix respectively. The discrete state space model is therefore defined by:

$$\begin{cases} A_k = \begin{bmatrix} 1+a_1T & a_2p\Omega\mathrm{T} & a_3T & a_4p\Omega\mathrm{T} & 0 \\ -a_2p\Omega\mathrm{T} & 1+a_1T & -a_4p\Omega\mathrm{T} & a_3T & 0 \\ a_5T & -a_6p\Omega\mathrm{T} & 1+a_7T & -a_8p\Omega\mathrm{T} & 0 \\ a_6p\Omega\mathrm{T} & a_5T & a_8p\Omega\mathrm{T} & 1+a_7T & 0 \\ 0 & 0 & 0 & 0 & 1 \end{bmatrix} \\ B_k = T\begin{bmatrix} b_1 & 0 & b_2 & 0 \\ 0 & b_1 & 0 & b_2 \\ b_2 & 0 & b_3 & 0 \\ 0 & b_2 & 0 & b_3 \\ 0 & 0 & 0 & 0 \end{bmatrix} \\ C_k = \begin{bmatrix} 1 & 0 & 0 & 0 & 0 \\ 0 & 1 & 0 & 0 & 0 \end{bmatrix} \end{cases} \tag{34}$$

The Kalman filter considers that the state and the measurement noises vector as Gaussian white noise of zero mean.
The covariance matrices are, respectively, Q and R*;* defined by:

$$\begin{cases} Q_k = cov(W_k) = E\{W_k{W_k}^T\} \\ R_k = cov(V_k) = E\{V_k{V_k}^T\} \end{cases} \tag{36}$$

With the noises W_k and V_k are white noises uncorrelated Gaussian, characterized by zero mean of the covariance matrices Q_k and R_k

IV.3. IMPLEMENTATION OF THE KALMAN FILTER ALGORITHM

In the first time, it is necessary to use initial values of the covariance system matrices of the measurement noises and the state noises (*Q*) and (*R*), respectively, to obtain the best considerable speed value [12]. They have important results on the stability filter and convergence time. These matrices are supposed diagonal covariances.
Initialization: There are two steps to implement the EKF algorithm, the first is the prediction, the second is the correction, and these two steps are introduced by an initialization of state vector X_0 and the covariance matrix P_0,Q_0 and R_0.
- State vector prediction at time (k +1):

- The filtering algorithm contains two principal steps, a prediction step and a filtering step [12*;* 13]. In the first one, the predicted states values $\hat{X}(k+1)$ are obtained by using a mathematical model (state-variable equations), and also the previous values of the estimated states:

$$\hat{X}(k+1) = f[\hat{X}(k), U(k), k\,] \tag{37}$$

Therefore, the predicted state covariance matrix (*P*) is obtained before the new measurement values.
At the end, the mathematical model and also the covariance matrix of the system (Q) are used.

- During the second step, which is the filtering, the estimated states $\hat{X}(k+1)$ are obtained from the predicted ones, they estimate $\mathrm{X}(k+1)$ by adding a correction term $K(y-\hat{y})$ to the predicted value. This correction term is a weighted variety between the current output vector y and the predicted output vector $\hat{y}$. Here K is the Kalman gain [13].

V. RESULTS AND DISCUSSION

The simulations of the DFIM control and speed estimation method with the extended Kalman filter have been done using the MATLAB/Simulink software. Simulation results are shown in Figures from Fig5 to Fig8. Figure 5(a) represents the speed response using the mechanical sensor after applying a reference step of speed at (t = 0.1s); then the load torque is applied at (t = 0.6s). After that, the reversal of the rotation direction is applied at (t = 1.2s). Figure 5(b) presents the estimated speed by EKF resembling to the real speed it. Electromagnetic torque with a sensor of speed and with EKF are shown in Figures 6(a) and 6(b) respectively.
The same things are applied in the stator Currents in Figures 7 (a) and 7(b), and Rotor currents in Figures 8 (a) and 8(b). Except in the case of a sensor-less control, there is a small fluctuation due to the estimation by the Kalman filter. These results are shown in the diagram; we develop a speed estimation of the DFIM using the EKF, eliminating the mechanical speed sensor. Note that the Kalman Filter estimator presents a good tracking for the rotor speed with a weak error in steady state, the EKF is still robust during the load application and reversal of the speed.

VI. CONCLUSION

In this paper, a vector Control strategy of DFIM with and without mechanical sensor by estimation using EKF is presented. It has been shown that oriented rotor flux vector control combined with a speed sensor has been realized in order to obtain good decoupling between flows and a good regulation of motor currents, in order to ensure a good dynamic performance of the global system. In the same time, it solves the problems of the speed control with mechanical sensor. The interesting simulation results obtained on the control show the efficiency, the convergence and the stability of the system in case of load noise or change variation. The use of the EKF in the vector control allows obtaining a good decoupling and a good regulation of the currents in order to ensure a good dynamic performance of the global system in the speed control by estimation .In this work a robust sensor-less control combined with an EKF approach has been shown.

FOC results **with** speed sensor	**FOC** results **with** speed estimation

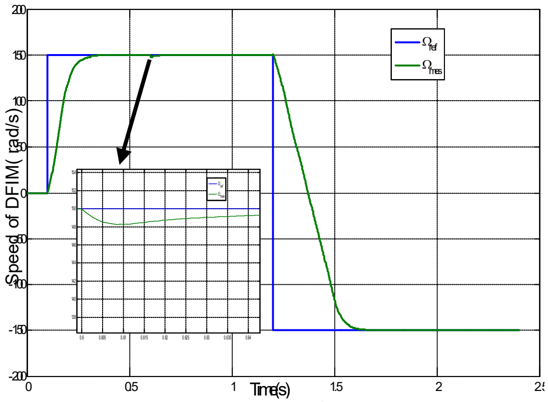

Fig .5 (a) Step Speed Response

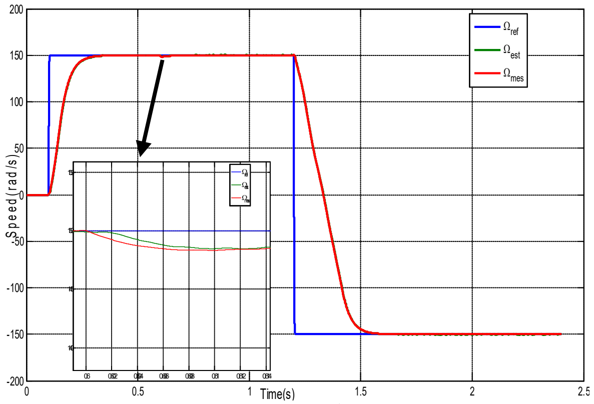

Fig .5. (b) Step Speed Response

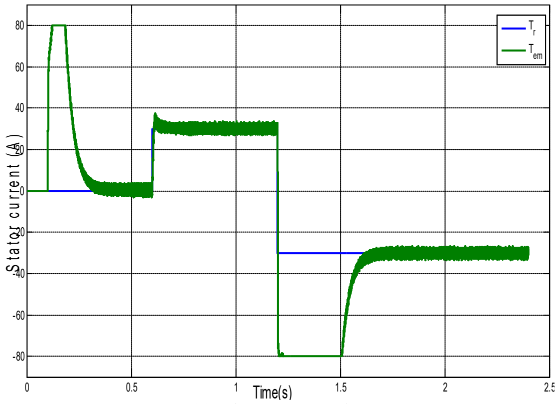

Fig .6. (a) Electromagnetic Torque

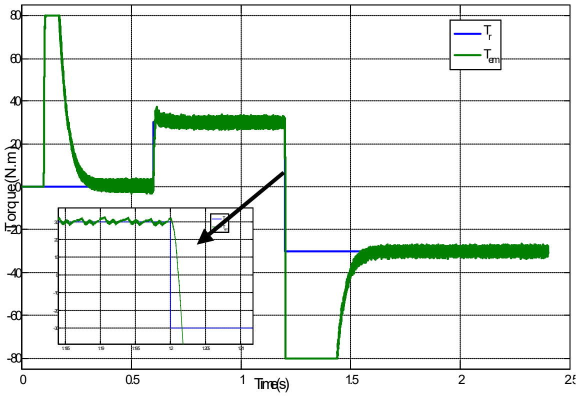

Fig .6. (b) Electromagnetic Torque

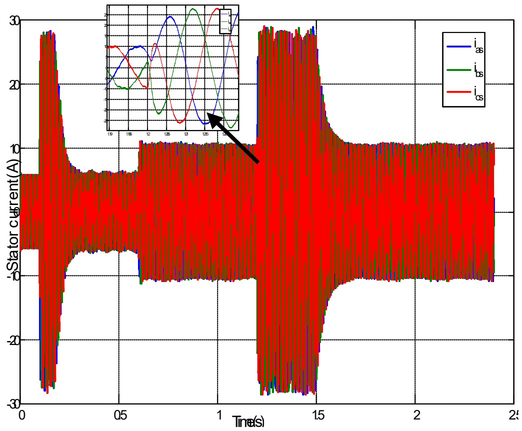

Fig .7 (a) Stator current

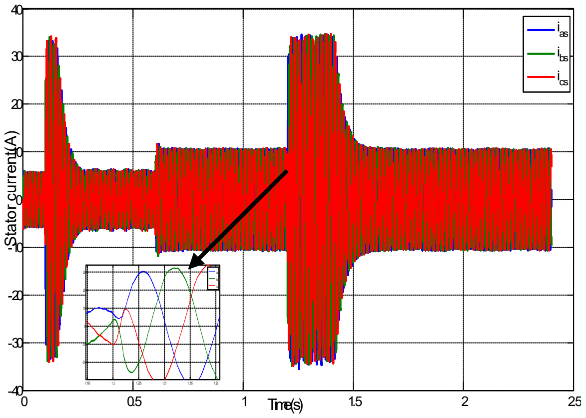

Fig .7. (b) Stator current

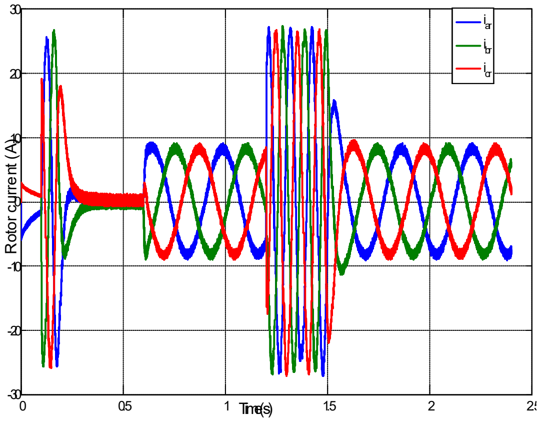

Fig .8 (a) Rotor current

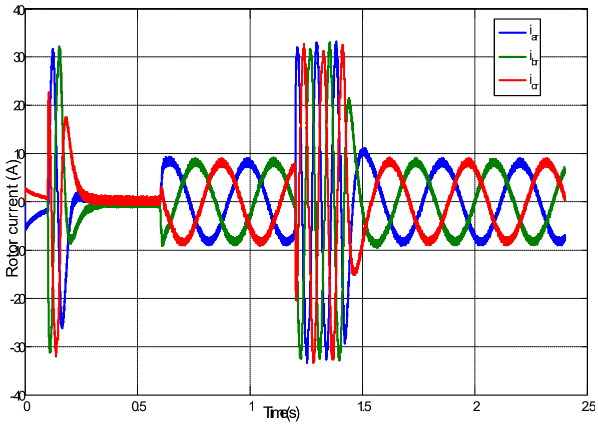

Fig .8. (b) Rotor current

APPENDIX

- DFIM parameters used in simulation

Stator resistance	Rs=1.20 Ω
Rotor resistance	Rr=1.80 Ω
Stator inductance	Ls = 0.1568 H
Rotor inductance	Lr = 0.1554 H
mutual inductance	M=0.150H
Inertia moment	J=0.070 Kg.m^2
Coefficient of viscous	f=0.001
Number of pairs of poles	P=2

ACKNOWLEDGMENT

The research is a part of the first author thesis PhD, realized, respectively, in the Laboratory of Electrical Engineering and Automatic LREA Research, University of Dr, Yahia Fares, Medea, and the Laboratory of Process Control (LCP), Ecole Nationale Polytechnqiue.

REFERENCES

[1] S. Khojet El Khil, I. Slama–Belkhodja, M.Pietrzak–David & B. de Fornel « A Fault Tolerant Operating System in a Doubly Fed Induction Machine Under Inverter Short-circuit Faults »1-4244-0136-4/06/$20.00 '2006 IEEE. https://doi.org/10.1109/IECON.2006.347954

[2] F.BONNET, 'Contribution à l'Optimisation de la Commande d'une Machine Asynchrone à Double Alimentation utilisée en mode Moteur thèses de doctorat, Institut national polytechnique de Toulouse, 2008.

[3] D. Lecocq, Ph. Lataire, ' The Indirect-Controlled Double Fed Asynchronous Motor for Variable-Speed Drives ', EPE 1995, pages 3.405 – 3.410.

[4] S. Lekhchinea, T. Bahib , I. Aadliab , Z. Layateb , H. Bouzeriac, "Speed control of doubly fed induction motor " Energy Procedia 74, 575 – 586, 2015.

[5] E. Levi, M. Wang "A speed estimator for high performance sensor-less control of induction motors in the field weakening region", IEEE trans. on Power Electronics, vol.17, no. 3, pp. 365-378, May 2002. https://doi.org/10.1109/PESC.2004.1355479

[6] H. Rahali, S. Zeghlache, L. Benalia "Adaptive Field-Oriented Control Using Supervisory Type-2 Fuzzy Control for Dual Star Induction Machine". International Journal of Intelligent Engineering and Systems, Vol.10, No.4, 2017. https://doi 10.22266/ijies2017.0831.04

[7] P. E. Vidal, « Commande non linéaire d'une machine asynchrone à double alimentation», Thèse de Doctorat de l'Institut National Polytechnique de Toulouse, Décembre 2004.

[8] D.Ben Attous, Y. Bekakra. "Speed control of a doubly fed induction motor using fuzzy logic technique. International on Electrical Engineering and Informatics"; 2010, Vol.2,No.3 .p. 179-189. https://doi.org/10.15676/ijeei.2010.2.3.2

[9] Sejir Khojet El Khil, « commande vectorielle d'une machine asynchrone doublement alimentée (MADA) », thèse de doctorat, Institut national polytechnique de Toulouse, 2006.

[10] Bennassar, A. Abbou, A. Akherraz, M. "Speed sensorless indirect field oriented control of induction motor using an extended kalman filter", Journal of Electrical Engineering March 2013. https://doi.org/10.1109/IRSEC.2015.7455046

[11] Leite, A.V. Araujo, R.E. Freitas, D. "Full and reduced order extended kalman filter for speed estimation in induction motor drives: a comparative study", 35th Annual IEEE Power Electronics Specialists Conference, IEEE, pp. 2293-2299, 2004. https://doi.org/10.1109/PESC.2004.1355479

[12] Y-Rl. Kim, S-K. Sul, M-H. Park « Speed Sensorless Vector Control of an Induction Motor Using an Extended Kalman Filter »594 - 599 vol.1, IEEE, August 2002. https://doi.org/10.1109/28.315233

[13] M. Benziane, Y., Mokhtari, N., and Lousdad, A. "Vold-Kalman Filter Order Tracking for the Detection of Stator Fault in Vector Controlled Induction Motor", *Majlesi Journal of Electrical Engineering*, Vol. 12, No. 4, pp. 75-84, 2018

Tahar DJELLOULI was born in Djelfa, Algeria, in 1970. He received the Engineer Diploma degree from Iben Khaldoun University, Tiaret, in Jun 1993, the Magister degree from the University of Dr. Yahia Fares, Médéa, in 2010, and the Ph.D degree from ENP, in 2022. He is currently an assistant professor at Ghardaia university. His current research interests are oriented towards the modeling and sensorless control of electrical machines.

Mohamed Seghir BOUCHERIT was born in Algiers, Algeria. He is a Professor and University Research Professor in the Ecole Nationale Polytechnique. His fields of research are nonlinear control, power electronics, and variable-speed drives. He has contributed to several national and international journals and conferences for several years.

Production of hydrogen and carbon nanofilaments using a novel reactor configuration: hydrodynamic study and experimental results

Abir Azara, Jasmin Blanchard, Faroudja Mohellebi, El Hadi Benyoussef, François Gitzhofer and Nicolas Abatzoglou

Abstract− A novel reactor configuration combining two beds, a central fluidized bed and an annular mobile bed, was designed for the production of hydrogen and carbon nanofilaments via dry reforming of gases produced from the pyrolysis of plastic waste. This combination allows for easy recovery of these nanomaterials and, since the mixture of catalyst and carbon formed is continuously fluidized, it prevents blockage.

Understanding the hydrodynamics is crucial for choosing the optimal operating conditions. Thus, a cold mock-up unit of the same size has been built and used. Since the gases produced by plastic pyrolysis are mainly composed of unsaturated hydrocarbons, the prototype reactor setup has been operated using ethylene as a surrogate molecule. The preliminary experimental results of the reactor operation with ethylene obtained so far are very promising and confirm the operability of the process. Next step is to operate continuously for longer time and reach a production of 1kg/h of carbon nanofilaments.

***Keywords*− Carbon nanofilaments, Fluidized bed, Hydrodynamics, Hydrogen, Reactor.**

NOMENCLATURE

CNF	Carbon Nanofilaments.
DR	Dry reforming
FBR	Fluidized bed reactor
FEG	Field emission gun
FCC	Fluid catalytic cracking
SBE	Spouted bed reactor
SEM	Scanning electron microscopy
TOS	Time-on-stream
XRD	X-Ray diffraction

I. INTRODUCTION

Various types of reactors are used for thermocatalytic reactions such as dry reforming (DR). The most conventional ones are: fixed bed [1–3], fluidized bed (FBR) [4–6], rotary [7–9] and membrane reactors [10–12]. Fixed bed reactors have several problems, and their use remains limited on a laboratory scale because it is easier at this scale to provide a high energy supply in order to overcome the endothermicity of DR reaction. Nevertheless, this heat transfer represents a major drawback at industrial scale and still remains a major techno-economic challenge for the large-scale industrial processes [13].

Fluidized bed reactor (FBR) is also widely studied [5]. This type of reactor promotes heat and mass exchange between the gas and catalyst particles, thus ensuring a good mass transfer and a nearly uniform temperature in the reactor. In addition, this type of configuration makes it easy to add and remove catalyst, allowing for easier process scale-up [14–17].

There are also membrane reactors which have been extensively studied in the literature and applied to reforming processes of hydrocarbons and oxygenated hydrocarbons [10,18–21]. The interest of this type of reactor consists in the selective separation of the hydrogen from the products in order to push the balance in the direction of the products and, thus, increase the yields. This is particularly interesting for industrial reforming because at the desired high pressure operation the conversion even at equilibrium is typically lower than 75%.

When it comes to produce carbon, the fixed bed also presents the risk of blockage due to the accumulation of carbon on the catalyst particles. In the case of fluidized beds, the friction between the catalyst particles allows the carbon to detach and be carried away with the gas. There are several types of FBR configurations, such as: fluid catalytic cracking FCC riser reactors, spouted bed reactors SBR [22] and SPR with a draft tube which are called also Wurster type FBR [23]. However, FBR also presents some drawbacks, such as the variation of the bed density, particles attrition and the rupture of carbon nanostructures are the main drawbacks [7,9].

Researchers have long wanted to improve conventional fluidized bed reactors to ensure and optimize the operability of the process at industrial scale, which has resulted in many innovative reactor configurations. For example, Bajad et al. [15] developed a new reactor configuration consisting of co-central compartments for the conversion of plastic waste into

Manuscript received August 31, 2022; revised December 3, 2022.

This work was supported by PRIMA Québec (grant R10-010) and the National Science & Engineering Research Council of Canada (grant CRDPJ 500331-16).

A. Azara from department of Chemical and Biotechnological Engineering, Université de Sherbrooke, Sherbrooke, CANADA and also from Laboratoire de Valorisation des Énergies Fossiles, École Nationale Polytechnique. (e-mail: abir.azara@usherbrooke.ca / abir.azara@g.enp.edu.dz).

J. Blanchard from KWI polymers, Canada (e-mail: jblanchard@kwipolymers.ca).

E.H Benyoussef and F.Mohellebi are from Laboratoire de Valorisation des Énergies Fossiles, École Nationale Polytechnique. (e-mails:Elhadi.benyoussef@g.enp.edu.dz, ferroudja.iddir@g.enp.edu.dz).

F. Gitzhofer and N. Abatzoglou are from department of chemical and Biotechnological Engineering, Université de Sherbrooke, Sherbrooke, CANADA (e-mails:François.gitzhofer@usherbrooke.ca, Nicolas.abatzoglou@usherbrooke.ca).

Digital Object Identifier (DOI): 10.53907/enpesj.v2i2.115

liquid hydrocarbons, carbon nanotubes and hydrogen-rich syngas (**Fig. 1**). The advantage of this configuration is that the heat has been provided in the annulus to heat both compartments and reduce the need for energy. The reactor presented in this work is also a novel configuration. It is a combination of a fixed bed and a moving bed. The advantage of this configuration is that it facilitates the recovery of CNF which is done mechanically during the fluidized bed phase.

Understanding the hydrodynamics of reactors with new configuration is important for choosing the optimal operating conditions for appropriate operation. Using a cold mock-up on Plexiglas is an efficient means to visualize the complex phenomena that occur between the gas phase and solid particles. It helps also when retrofit modifications to an existing reactor is required [24].

The purpose of this work is to present a comprehensive study of the reactor hydrodynamics and to present the proof of the scale-up process operability by presenting the first experimental results.

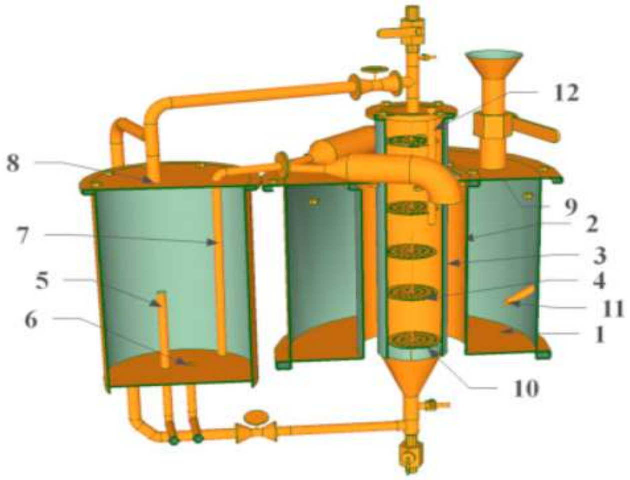

Fig. 1: Reactor cut section showing inner chambers and catalyst tray arrangement. (1 – pyrolysis chamber, 2 – heating chamber, 3 – CNT chamber, 4 – catalyst tray, 5 – oil drain line, 6 – water drain line, 7 – pyrolysis gas line to condenser, 8–non condensable gases to CNT chamber, 9 – Plastic feeder, 10 – first tray, 11 & 12 – thermo well) [15].

II. COLD MOCK-UP AND HYDRODYNAMIC STUDY

A. *Experimental set-up*

The prototype of a plexiglass reactor, used in this study to analyze the behavior of the gas phase and the solid phase inside the reactor, is presented in **Fig. *2*Erreur ! Source du renvoi introuvable.** and the dimensions are presented in **Erreur ! Source du renvoi introuvable.**. it is composed of two concentric cylinders, two lateral outlets and a conical base. The gas enters from the bottom through a distribution grid to ensure a uniform supply and exits through one of the two side outlets, the other outlet being closed. A grid is also located at the outlet to prevent the catalyst from being carried outside, however allowing the gas to exit freely.

Fig. 2 : Reactor mock-up.

Table I
Prototype dimensions

External cylinder diameter (cm)	12
Internal cylinder diameter (cm)	3.8
Entrance diameter (cm)	3.8
Exit diameter (cm)	4
External cylinder height (cm)	38
Internal cylinder height (cm)	27
Wall thickness (cm)	0.16
Angle of the conic base	45 °

B. *Experimental conditions*

The study of the pressure drop of the bed as a function of the superficial gas velocity is the conventional method which can give an idea of the fluidization regime.

The compressed air from the main line first passes through a mass flow meter (0-100 LPM), then passes through the pipe towards the reactor inlet; the gas flow is distributed using a perforated plate located at the reactor inlet. The outlet is linked to a pipe which is connected to the vacuum. The reactor has two gauges to measure the pressure at the top and bottom and therefore calculate the pressure drop. The two pressure sensors are connected to the computer via two acquisition cards. The pressure measurements are read directly on the screen. Particles of 300 microns and density equal to 1657 kg/m^3 were used as solid phase. A graduated scale was stuck at the external surface to measure the height of the reactor.

C. *Results and Discussion*

There are three different regions in the reactor (**Fig. 3**): the spout (S), the annulus (A) and the fountain (F).

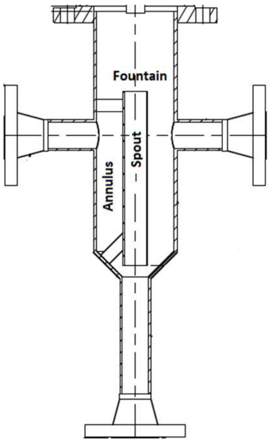

Fig. 3: Different regions in the reactor.

First, the movement of the catalyst was observed by visually following the profile over time of a layer of the same material but of a different color which was deposited at the surface of the bed in the annular section before the beginning of the tests. We observed that the movement of the solid is circular. The gas has two ways to reach the outlets: (a) by passing through the catalytic bed in the annular section towards the two outlets or (b) continue vertically to the end of the inner cylinder and then change direction towards the two outlets. If the gas flow is high enough along the entire length of the inner cylinder, the solid particles are fluidized (spout region S) and spring out like a fountain (fountain region F). In parallel with this movement, the solid particles in the annular region fall into the part below the inner cylinder to be entrained again allowing a slow downward movement of the catalyst in the annular part (region A). The latter, as shown in **Fig. 4** has been clearly proven by the descent of the colored layer. Over time, the color of particles becomes homogenous; because the colored layer reaches the bottom, and it is fluidized too; this oscillatory movement finishes by homogenizing the fluidized granular material. Since one of the two outlets has been used in our runs, the descent on one side is faster than the other. In fact, at industrial scale this lack of symmetry can be remedied by collecting the outlet gas flow through a radially positioned grid into another external annular section.

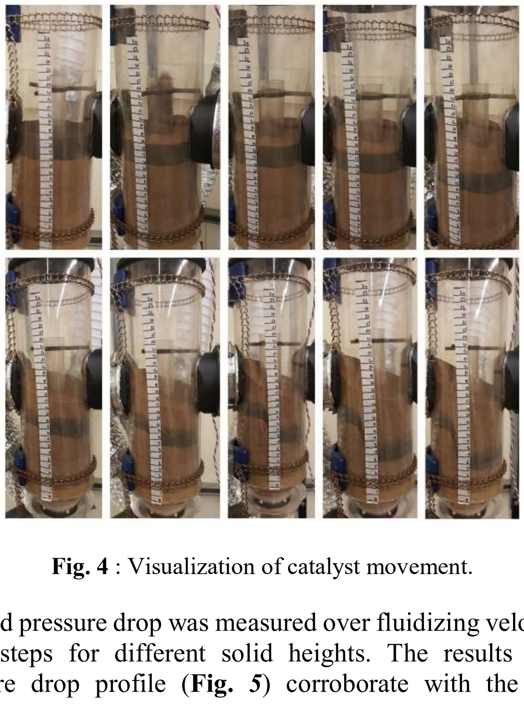

Fig. 4 : Visualization of catalyst movement.

The bed pressure drop was measured over fluidizing velocity in small steps for different solid heights. The results of the pressure drop profile (**Fig. 5**) corroborate with the visual observations. We observe the existing of three distinct zones:

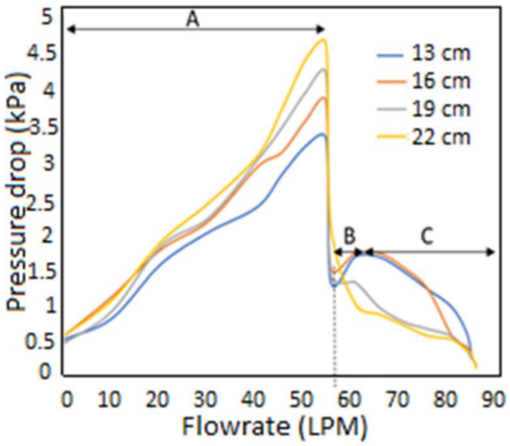

Fig. 5 : Pressure profile.

Zone A: blocking period

We notice that the pressure drop increases with the flow rate for the four bed heights; and it is higher with a higher height (mass) of the bed. The explanation is that the catalyst particles that are below the inner cylinder block the flow of gas as long as the weight of the catalytic bed is higher than the pressure drop due to the flow through the bed. Thus, pressure drop increases over flow rate.

Zone B: explosion period

We notice that after the plug, the pressure drop drops suddenly, because the plug is pushed away.

13 and 16 cm: the pressure drop increases a little bit.

19 cm: the pressure drop remains constant.

22 cm: the pressure drop continues to fall with the same slope.

For this period, the pressure is high enough to burst the plug and its force exceeds the weight of the bed in the inner cylinder causing the bed to expand rapidly in the inner cylinder and the solids to spurt out. The net decrease is attributed to the fact that the mass of the fluidized material in the inner cylinder is lower during the operation in zone B than that during zone A conditions. In other words, the amount of the fluidized material expelled equals the amount of that re-entering the inner concentric tube and it is lower than the amount placed initially in the bed.

Zone C: recirculation period

13 and 16 cm: pressure drop remains constant for a while and then decreases.

19 cm: after the explosion period, pressure drop decreases directly for high flow rates.

22 cm: after the explosion period, pressure drop decreases with a slower slope when increasing the flow rate.

During this period, the solids of the annular region fall in the lower part of the inner cylinder to be fluidized and entrained which makes a periodic oscillatory movement of entrainment of the solids characterized by a slow downward movement of the bed in the annular part and an entrainment in the inner cylinder .

The minimum flow rate to pass from zone A to zone B is near 55 SLPM for nearly all heights tested.

III. SCALE UP PROCESS

A. Materials

The targeted feedstock is gases derived from plastic pyrolysis, which are largely composed of unsaturated HC. The initial step, which is presented in this work, is the use of ethylene as a surrogate molecule.

The catalyst used is Fe supported on alumina. Since the aim is to test the operation of the reactor, the use of a well-known catalyst was recommended.

B. P&ID

The set-up presented in **Fig. 6** is composed of three operation sections, the first one is reaction section, where the reaction is conducted in the novel reactor vessel (R1), covered by a heating jacket with temperature control. The catalyst is deposited inside the reactor and gases are fed from commercial gas cylinders (supplied by LINDE): C_2H_4 (99%), CO_2 (99%) and then preheated. Three ALICAT mass flow controllers were used to control the gas flows at the inlet. The CNF are removed from the catalyst due to the friction and entrained with the exiting gas to enter the filtration section where they are retrieved from the gas using metallic filters at an efficiency as high as approximately 90%. This filter is cleaned up periodically using N_2 pulsations and the CNF are collected in reservoir R2 in the recovery section. The filtration section and recovery sections are inside an appropriate designed space with negative pressure that is suitable for handling nanomaterials. The last section comprises the exchanger for the quenching of gaseous stream and the final conditioning through the glycol bath for the complete removal of water vapors prior to final disposal through a flameless and smokeless flare. The flow rate of the products is measured using a totalizer and its composition is analyzed by gas chromatography (Scion 400 Series GC).

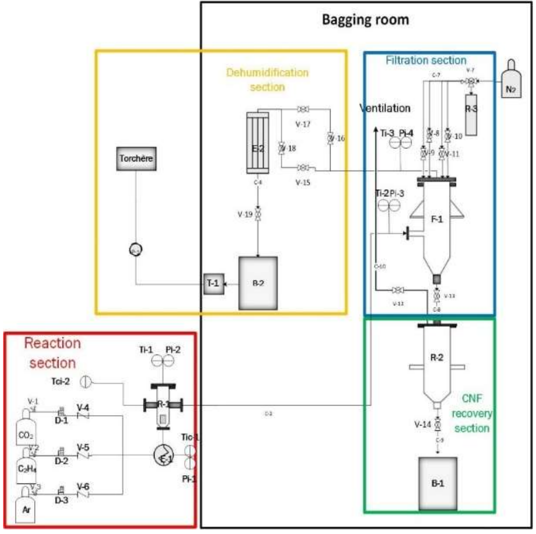

Fig. 6 : P&ID of the scale up process

C. Experimental methodology

Preparation of the catalyst

The catalyst used is Fe supported on alumina and it was prepared via wet impregnation. Iron nitrate ($Fe(NO_3)_3.9H_2O$) is dissolved in water (volume greater than pore volume) then the alumina is added. The mixture is stirred for 4 hours until it becomes a “slurry”. The slurry is dried at 105°C overnight to remove remaining solvent. The catalyst is then calcined under an air atmosphere for 3 hours at 750 at 2° C./min. Finally, the catalyst is crushed and sieved down to 250 microns.

Activation of the catalyst

The catalyst was activated under a flow of 50% H_2 and 50% Ar for a time-on-stream (TOS) of 0.5 hour. **Table *II*** shows the activation test conditions.

Table II
Activation conditions

Catalyst	H_2 flow rate (SLPM)	N_2 flow rate (SLPM)	Catalyst Weight (kg)	TOS (h)	T(°C)
Fe/Al_2O_3 (10 wt%)	**1**	**3**	**0.5**	**0.5**	**550**

Reaction and CNF and H_2 production

CNF were produced via ethylene DR reaction. The reaction conditions are presented in **Table *III.***

The reaction temperature was chosen following a study of thermodynamic equilibrium at temperatures ranging from 350 °C to 850 °C. The study is presented in the Results and Discussion section. Even though it was found in the hydrodynamic study that the minimum fluidization flow (transition from zone A to zone B) is approximately 55 SLPM, the total flow used is four SLPM. This is due to the high pressure generated by the very high flow rate feed, that the reactor is designed to operate at a pressure of 2.5 atm. On the other hand, to ensure the detachment of the carbon from the catalyst particles, pulses were made every 10 minutes using nitrogen to fluidize the bed for two minutes.

Table III
Reaction conditions

Catalyst	C_2H_4 flow rate (S LPM)	CO_2 flow rate (S LPM)	Catalyst Weight (kg)	TOS (h)	T(°C)
Fe/Al_2O_3 (10 wt%)	**3**	**1**	**0.5**	**6**	**600**

Characterization techniques

Two techniques were used to characterize the catalysts and carbon produced:

X-Ray diffraction (XRD) analysis was used to identify the catalyst crystalline structure before and after reaction. The diffractograph used is Philips X'pert PRO equipped with a Cu tube as its X-ray source and a Ni filter which is used to only let through Kα1 radiations from Cu (1.5418 Å) produced at 40 kV and 50 mA. The anti-dispersion slit was set at 1/2 and the divergence slit at 1/4. The analysis is carried out with a scanning angle 2θ ranging from 15 to 90°.

Scanning electron microscopy (SEM) was used to characterize the carbons formed and to study their morphology. The microscope used is a S-4700 Hitachi with field emission gun (FEG). It is equipped with detectors for secondary electrons (SE) and backscattered electrons (BSE). the working distance is 2.5-12mm and the accelerating voltage ranges from 1kV to 30kV. The magnification is up to 200,000X with resolution down to 5nm.

Reaction metrics

The extent of the reaction is evaluated by calculating: C_2H_4 conversions ($X_{C_2H_4}$), H_2 yield (Y_{H_2}) and carbon yield (Y_C).

$$X_{C_2H_4}\,(\%) = \frac{(F_{C2H4,in} - F_{C2H4,out})}{F_{C2H4,in}}$$

$$Y_{H_2}\,(\%) = \frac{F_{H2}}{2 \times F_{C2H4,in}} \times 100$$

$$Y_C\,(\%) = \frac{m_{C\,deposit}}{m_{C,in}} \times 100$$

$m_{C_{deposit}}$= $m_{catalyst,tf}$ - $m_{catalyst,t0}$

$m_{C,in}$= ((2×$F_{C2H4,in}$ ×time+ $F_{CO2,in}$×time)) *M_C

Where:
$F_{C2H4,in}$ and $F_{C2H4,out}$ respectively denote the molar flow rates of C_2H_4 at the inlet and the outlet of the reactor,
F_{H2} the molar flow rate of H_2 at the outlet of the reactor,
$m_{C,in}$ the mass of carbon fed,
$m_{c\ deposit}$ the mass of solid carbon deposit on the catalyst,
$m_{catalyst,tf}$ the mass of the catalyst after reaction,
$m_{catalyst,t0}$ the mass of the catalyst before reaction,
M_C the molar mass of C = 12.0107 g.mol^{-1}.

D. *Results and Discussion*

Thermodynamic investigation

FactSage software was used to study the thermodynamic equilibrium of the C_2H_4 DR reactions at different conditions of temperature (450-850 °C) and molar ratios C_2H_4/CO_2 (1/1-3/1), at atmospheric pressure. Equilibrium composition as well as the amount of deposited carbon were estimated. This investigation allowed us to choose the experimental conditions which optimize carbon and synthesis gas (CO+H_2) yields. The most useful results are shown in **Fig.** *7* and **Fig. 8**.

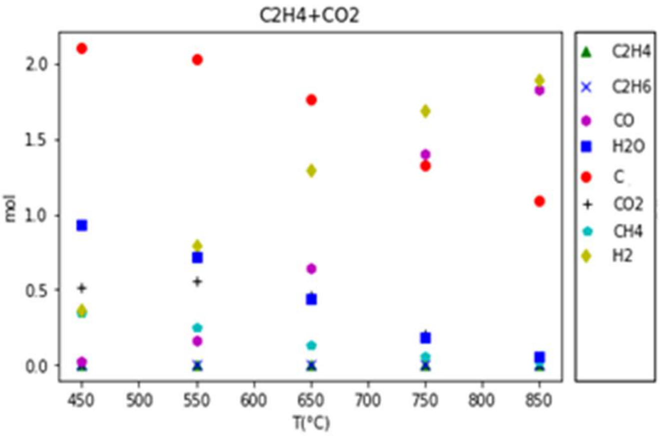

Fig. 7: Product composition for ethylene DR at ratio 1/1

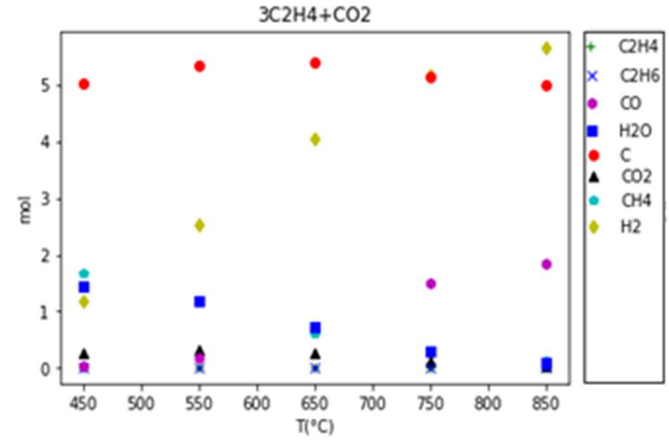

Fig. 8: Product composition for ethylene DR at ratio 3/1

We can observe that H_2 amount increases with temperature for both ratios, while C amount decreases with temperature at ratio 1/1; and reaches its maximum at temperature between 600-650 °C at a ratio of 3/1. Based on these results, 600 °C was chosen as the reaction temperature. Since we want to maximize carbon and H_2 production, a 3/1 ratio of C_2H_4/CO_2 was chosen.

Experimental results

The results of the reaction at 600 °C and ratio 3/1 are presented in **Table *IV***.

Table IV
General experimental results for the DR reaction at 600 °C and Fe-Al_2O_3 10% for 4h TOS.

C_2H_4 (SLPM)	3
CO_2 (SLPM)	1
Catalyst weight (kg)	0.5
TOS (hours)	6
$GHSV_{STP}$ (l.h^{-1}. kg^{-1})	480
C_2H_4/CO_2	3
Carbon (g)	615
Carbon growth rate (kg$_C$.kg$_{cat}^{-1}$.h^{-1})	0.2
Carbon yield (%)	53.2
Total H_2 yield (%)	46.4
Total C_2H_4 conversion (%)	73.0
Total CO_2 conversion (%)	69.9
Mass balance error for C (%)	6.3
Mass balance error for H (%)	4.0
Mass balance error for O (%)	4.3

The carbon formed was analyzed by SEM and it has been proven that it is filamentous as shown in **Fig. 9**.

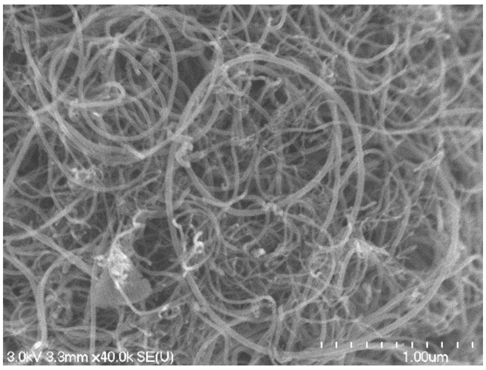

Fig. 9: SEM of deposited carbon

Fig. 10 and **Fig. 11** show the XRD of the fresh catalyst and deposited carbon on used catalyst after the DR reactions, respectively.

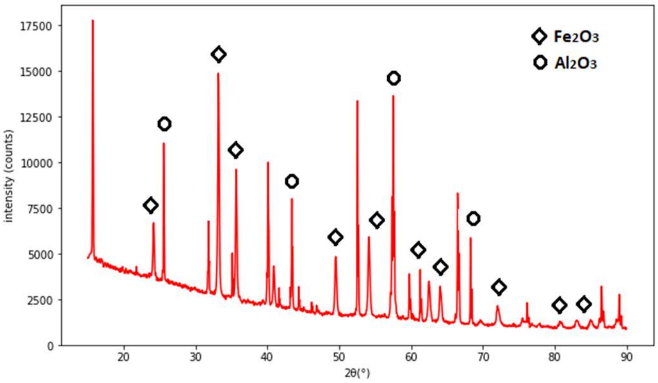

Fig. 10 : XRD of fresh catalyst

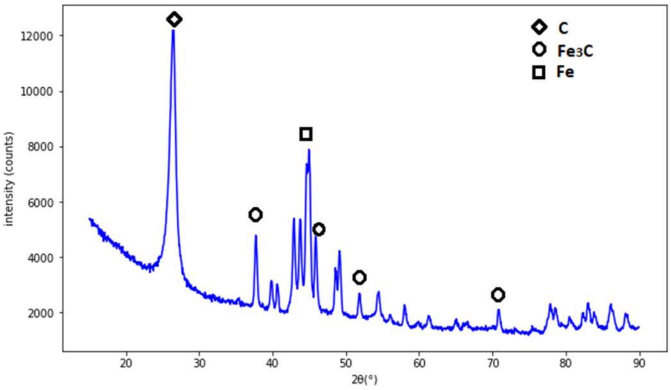

Fig. 11 : XRD of the spent catalyst

Discussion

The production of CNF at a pilot scale in a continuous mode has not been reported in the literature. In this work, we managed to operate a kilo lab scale reactor. The carbon produced in the reactor has been removed from the catalyst particles thanks to the friction between the particles which are in continuous movement between the two beds. The CNF with nanometric size were entrained with the existing gaseous stream and retrieved in the filter.

The carbon and H_2 yields are 53% and 46% respectively. These high rates are due to the suitable activity of the iron-based catalyst. Although the first reduction step with H_2 activated the catalyst, the H_2 formed at the beginning of the reaction contributes to catalyst activation by further reduction of iron oxides. This is proven by the presence of Fe metal peaks and the disappearance of iron oxide peaks on used catalyst XRD (**Fig. 11**). Also, carbon itself may contribute to the catalytic activity. It has been demonstrated that the carbon under the form of catalytically induced CNF itself has catalytic properties [25].

The XRD of used catalyst after the reaction, proves the deposition of carbon. The peak at $2\theta=26°$ confirms that the carbon formed is graphitic. Moreover, no peaks of oxides have been found and only Fe was present in the diffractograms; the latter prove that Fe oxides were reduced during the reactions. Carbide formation was expected, because carbides are known to be the precursor of CNF especially with iron based catalyst; Fe_3C is metastable under the reaction conditions and it is decomposed to CNF and α-Fe [26]. Consequently, carbides co-exist along with CNF and Fe^0.

The SEM analyses reported above help us to identify the morphology of carbon produced. It is well known that there are different types of carbon that can be produced, pyrolytic, encapsulating and filamentous. Filamentous carbon is formed from the catalytic decomposition of HC, pyrolytic carbon is formed from HC thermal decomposition at high T, and encapsulating carbon is usually formed at relatively low T when the adsorbed HC accumulate on the surface of the catalyst and the C_nH_m* radicals slowly polymerize [27]. **Fig. 9** shows clearly that the carbon formed is filamentous with different width and length.

IV. CONCLUSION

Compared with waste plastics, CNF and H_2 are high-added-value products. Many efforts have been deployed to produce them at industrial scale with an optimized process in terms of energy efficiency, continuity and the facility of the system operation. This work is part of such an endeavor. The reactor conceived, built and operated is a novel configuration which has several advantages: especially in terms of recovery of carbon nanofilaments.

The process development unit used in this study is at pilot kg-lab scale, with the use of half a kg of catalyst and a total flow rate of reactants of four SLPM. Even though some problems occurred, the system worked very well, and more than 600 g of carbon was produced. The main drawback is that the scale is still low and after some hours of operation, there is a tendency of carbon accumulation at the relatively small orifices. Nevertheless, this study proved the concept at nearly kg-lab scale and further improvement will come along with a bigger scale up which is the intention of the research and industrial partner for the next steps towards commercialization.

ACKNOWLEDGMENT

The authors are indebted to PRIMA Québec (grand R10-010), the National Science & Engineering Research Council of Canada (grand CRDPJ 500331-16), as well as the companies KWI Polymers Solutions Inc. and Soleno Inc. for funding related to this project.

REFERENCES

[1] A.H. Fakeeha, A.A. Ibrahim, W.U. Khan, K. Seshan, R.L. Al Otaibi, A.S. Al-Fatesh, Hydrogen production via catalytic methane decomposition over alumina supported iron catalyst, Arab. J. Chem. 11 (2018) 405–414. https://doi.org/10.1016/j.arabjc.2016.06.012.

[2] Y. Binhang, Y. Xiaofang, W. Jie, Y. Siyy, M. MyatNeoZin, G. Elaine, X. Zhenhua, K. Shyam, X. Wenquian, C. Jingguang G., Dry Reforming of Ethane and Butane with CO2 over PtNi/CeO2 Bimetallic Catalysts, ACS Catal 6 11 7283-7292. (2016).

[3] A. Drif, N. Bion, R. Brahmi, S. Ojala, L. Pirault-Roy, E. Turpeinen, P.K. Seelam, R.L. Keiski, F. Epron, Study of the dry reforming of methane and ethanol using Rh catalysts supported on doped alumina, Appl. Catal. Gen. 504 (2015) 576–584. https://doi.org/10.1016/j.apcata.2015.02.019.

[4] J.L. Pinilla, M.J. Lázaro, I. Suelves, R. Moliner, J.M. Palacios, Characterization of nanofibrous carbon produced at pilot-scale in a fluidized bed reactor by methane decomposition, Chem. Eng. J. 156 (2010) 170–176. https://doi.org/10.1016/j.cej.2009.10.032.

[5] J.L. Pinilla, R. Moliner, I. Suelves, M.J. Lázaro, Y. Echegoyen, J.M. Palacios, Production of hydrogen and carbon nanofibers by thermal decomposition of methane using metal catalysts in a fluidized bed reactor, Int. J. Hydrog. Energy. 32 (2007) 4821–4829. https://doi.org/10.1016/j.ijhydene.2007.08.013.

[6] P. Ugarte, P. Durán, J. Lasobras, J. Soler, M. Menéndez, J. Herguido, Dry reforming of biogas in fluidized bed: Process intensification, Int. J. Hydrog. Energy. 42 (2017) 13589–13597. https://doi.org/10.1016/j.ijhydene.2016.12.124.

[7] J.L. Pinilla, R. Utrilla, M.J. Lázaro, I. Suelves, R. Moliner, J. M. Palacios, A novel rotary reactor configuration for simultaneous production of hydrogen and carbon nanofibers, Int. J. Hydrog. Energy. 34 (2009) 8016–8022. https://doi.org/10.1016/j.ijhydene.2009.07.057.

[8] J.L. Pinilla, R. Utrilla, M.J. Lázaro, R. Moliner, I. Suelves, A.B. García, Ni- and Fe-based catalysts for hydrogen and carbon nanofilament production by catalytic decomposition of methane in a rotary bed reactor, Fuel Process. Technol. 92 (2011) 1480–1488. https://doi.org/10.1016/j.fuproc.2011.03.009.

[9] S.L. Pirard, A. Delafosse, D. Toye, J.-P. Pirard, Modeling of a continuous rotary reactor for carbon nanotube synthesis by catalytic chemical vapor deposition: Influence of heat exchanges and temperature profile, Chem. Eng. J. 232 (2013) 488–494. https://doi.org/10.1016/j.cej.2013.07.077.

[10] A.V. Alexandrov, N.N. Gavrilova, V.R. Kislov, V.V. Skudin, Comparison of membrane and conventional reactors under dry methane reforming conditions, Pet. Chem. 57 (2017) 804–812. https://doi.org/10.1134/S0965544117090031.

[11] J. Múnera, S. Irusta, L. Cornaglia, E. Lombardo, CO2 reforming of methane as a source of hydrogen using a membrane reactor, Appl. Catal. Gen. 245 (2003) 383–395. https://doi.org/10.1016/S0926-860X(02)00640-3.

[12] Improved hydrogen production from dry reforming reaction using a catalytic packed-bed membrane reactor with Ni-based catalyst and dense PdAgCu alloy membrane - ScienceDirect, (n.d.). https://www.sciencedirect.com/science/article/pii/S0360319915306923?via%3Dihub (accessed May 11, 2018).

[13] R. Aiello, J. E Fiscus, H.-C. Zur Loye, M. D Amiridis, Hydrogen production via the direct cracking of methane over Ni/SiO2: Catalyst

deactivation and regeneration, Appl. Catal. Gen. 192 (2000) 227–234. https://doi.org/10.1016/S0926-860X(99)00345-2.

[14] I. Barbarias, G. Lopez, M. Artetxe, A. Arregi, J. Bilbao, M. Olazar, Valorisation of different waste plastics by pyrolysis and in-line catalytic steam reforming for hydrogen production, Energy Convers. Manag. 156 (2018) 575–584. https://doi.org/10.1016/j.enconman.2017.11.048.

[15] G.S. Bajad, R.P. Vijayakumar, A.G. Gupta, V. Jagtap, Y. pal Singh, Production of liquid hydrocarbons, carbon nanotubes and hydrogen rich gases from waste plastic in a multi-core reactor, J. Anal. Appl. Pyrolysis. 125 (2017) 83–90. https://doi.org/10.1016/j.jaap.2017.04.016.

[16] A. Azara, S. Belbessai, N. Abatzoglou, A review of filamentous carbon nanomaterial synthesis via catalytic conversion of waste plastic pyrolysis products, J. Environ. Chem. Eng. 10 (2022) 107049. https://doi.org/10.1016/j.jece.2021.107049.

[17] R.-X. Yang, K.-H. Chuang, M.-Y. Wey, Effects of Nickel Species on Ni/Al2O3 Catalysts in Carbon Nanotube and Hydrogen Production by Waste Plastic Gasification: Bench- and Pilot-Scale Tests, Energy Fuels. 29 (2015) 8178–8187. https://doi.org/10.1021/acs.energyfuels.5b01866.

[18] K. El, S. Da, D. Ja, P. Wd, M. Le, C. Jgg, B. Dj, The role of rhenium in the conversion of glycerol to synthesis gas over carbon supported platinum-rhenium catalysts, J. Catal. 260 (2008) 164–177.

[19] H.R. Godini, S. Xiao, M. Kim, O. Görke, S. Song, G. Wozny, Dual-membrane reactor for methane oxidative coupling and dry methane reforming: Reactor integration and process intensification, Chem. Eng. Process. Process Intensif. 74 (2013) 153–164. https://doi.org/10.1016/j.cep.2013.09.007.

[20] B. Lee, S. Lee, H. Lim, Numerical modeling studies for a methane dry reforming in a membrane reactor, J. Nat. Gas Sci. Eng. 34 (2016) 1251–1261. https://doi.org/10.1016/j.jngse.2016.08.019.

[21] S. Sumrunronnasak, S. Tantayanon, S. Kiatgamolchai, T. Sukonket, Improved hydrogen production from dry reforming reaction using a catalytic packed-bed membrane reactor with Ni-based catalyst and dense PdAgCu alloy membrane, Int. J. Hydrog. Energy. 41 (2016) 2621–2630. https://doi.org/10.1016/j.ijhydene.2015.10.129.

[22] F.J. Weinberg, T.G. Bartleet, F.B. Carleton, P. Rimbotti, J.H. Brophy, R.P. Manning, Partial oxidation of fuel-rich mixtures in a spouted bed combustor, Combust. Flame. 72 (1988) 235–239. https://doi.org/10.1016/0010-2180(88)90124-1.

[23] D.E. Wurster, Particle coating process, US3253944A, 1966. https://patents.google.com/patent/US3253944A/en (accessed March 15, 2020).

[24] S. Sundaresan, Role of hydrodynamics on chemical reactor performance, Curr. Opin. Chem. Eng. 2 (2013) 325–330. https://doi.org/10.1016/j.coche.2013.06.003.

[25] S. Jankhah, N. Abatzoglou, F. Gitzhofer, J. Blanchard, H. Oudghiri-Hassani, Catalytic properties of carbon nano-filaments produced by iron-catalysed reforming of ethanol, Chem. Eng. J. 139 (2008) 532–539. https://doi.org/10.1016/j.cej.2007.08.031.

[26] M.A. Ermakova, D.Y. Ermakov, A.L. Chuvilin, G.G. Kuvshinov, Decomposition of Methane over Iron Catalysts at the Range of Moderate Temperatures: The Influence of Structure of the Catalytic Systems and the Reaction Conditions on the Yield of Carbon and Morphology of Carbon Filaments, J. Catal. 201 (2001) 183–197. https://doi.org/10.1006/jcat.2001.3243.

[27] A.-C. Dupuis, The catalyst in the CCVD of carbon nanotubes—a review, Prog. Mater. Sci. 50 (2005) 929–961. https://doi.org/10.1016/j.pmatsci.2005.04.003.

ABIR AZARA is an engineer and a holder of Master 2 in chemical engineering; she has graduated from Ecole Nationale Polytechnqiue of Algiers in 2016. Since 2017, she is a PhD candidate in Sherbrooke University in Canada. Her project is a synergistic work between the university and two industrial partners. It focuses on the production of carbon nanostructures using a gas produced from waste plastic pyrolysis. She has published so far three articles and has participated on several conferences across Canada and worldwide.

Jasmin Blanchard is Chief Technology Officer at KWI Polymers located in Boisbriand, Canada. He has a master and a PhD degree in chemical engineering from Sherbrooke University in Canada completed in 2005 and 2014 respectively. The PhD is a project on Fischer-Tropsch synthesis using a catalyst generated by plasma. His field of expertise include methane reforming, carbon nanofiber synthesis, pyrolysis of plastic, synthesis of black carbon by plasma and graphene synthesis by plasma.

Faroudja Mohellebi is Professor at the department of chemical engineering of the Ecole Nationale Polytechnique, Algiers, Algeria and was head of department of chemical engineering from February 2009 to December 2021. Professor Mohellebi works on the mobility and bioavailability of traditional contaminants like cadmium and nickel and on compounds of emerging interest like drugs. Her work focuses on analyzing contaminants, their chemical speciation, environmental fate and potential impacts. She has participated in the training of many students and has proposed many research topics directly related to the depollution of water loaded with emerging products and pesticides. She has numerous collaborations and projects at national and international level. Her scientific production includes publications, reviews, keynotes, and three book chapters.

El Hadi Benyoussef is professor at the department of chemical engineering of the Ecole Nationale Polytechnique, Algiers, and head of the laboratory ‘laboratoire de valorisation des energies fossils LAVALEF’.

François Gitzhofer is full professor at the Department of Chemical & Biotechnological Engineering of the Université de Sherbrooke since 1991. He also served as Vice-Dean of Academic Affairs as well as Secretary of the Faculty of Engineering at the University of Sherbrooke. His main research contributions are related to materials synthesis including catalysts using Suspension Plasma Technology He is the co-applicant with professor Abatzoglou on the grant which funded this study.

Nicolas Abatzoglou is Professor and ex-Head of the Department of Chemical & Biotechnological Engineering of the Université de Sherbrooke. He is Adjunct Professor at the University of Saskatchewan and Fellow of the Canadian Academy of Engineering. He is a specialist in *Process Engineering involving particulate systems in reactive and non-reactive environments*. He is the Director of the GRTP (Group of Research on Technologies and Processes). The GRTP operates a brand new R&D and Scale-up facility at the Université de Sherbrooke and is financed by both Canadian & Quebec institutional funding and industrial partners such as Rio Tinto Iron & Titane, KWI and Soleno. From May 2008 to March 2021, he has been the holder of the Pfizer Industrial Research Chair in Pharmaceutical Processes. The highly successful output of this Chair led to a continuation of this association, which is now focusing on Process intensification, Analytical Technologies development and industrial applications. He has numerous collaborations and projects at national and international level and he served as one of the Leaders in Canada’s NCE Network BioFuelNet on Biorefining. He is presently the Leader of the Canadian side of the project GOLD funded by HORIZON 2020 and comprising 18 partners from EU, China and Canada. He is co-founder of the company *Enerkem Technologies*, precursor of Enerkem, a spin-off commercializing technologies in the field of energy from renewable resources. He has received many academic and professional awards and he is a world-renowned researcher and technology transfer expert. His scientific production includes 200+ publications, reviews, conferences, keynotes, plenaries and invited lectures, patents and three book chapters.

Microstructural, Mechanical and Electrochemical Characterization of a Flame Sprayed NiFeCrBSi/WC Cermet Coating

Rabah AZZOUG, Yamina MEBDOUA, and Fatah HELLAL

Abstract− To increase the lifetime of drilling bits, these components are usually covered with hard metal matrix composites. Nowadays, nickel-based metal matrix composites arise as substitutes to cobalt-based ones. The challenge now is to provide an efficient coating with low cost. The aim of this paper is to exploit the characteristics of a newly designed flame sprayed NiFeCrBSi-WC composite coatings. The experimental activities were carried out using the scanning electron microscopy, for the microstructural analysis of coating. Additionally, micro-hardness and nano-indentation tests were carried out to evaluate the resistance of the coatings against penetration. Moreover, the electrochemical behavior was assessed in NaCl and Na_2SO_4 aqueous solutions. The ionic concentrations were varied between 1 g/l to 35 g/l. The results show that the microstructure is dendritic and characterized by the presence of hard chromium carbides and nickel grains in the inter-dendritic space. The coating was subject to a slight decarburization. The presence of carbides and the decarburization make the microhardness of the matrix fluctuates between 300 HV to 900 HV. For the electrochemical response, the increase in ion concentration induces a decrease in the corrosion resistance. In Na_2SO_4 aqueous solutions, the charge transfer is roughly constant for the concentrations above 1 g/l.

***Keywords*− Flame spraying, nickel composite coatings, indentation, corrosion.**

I. INTRODUCTION

In the oil and gas industry, the research for inexpensive versatile materials with a long longevity has become an essential task to increase the drilling bits efficiency and to alleviate the impact of the unsteady oil price fluctuations on the production progress. The nature of the encountered rock formations and the severity of the operational drilling conditions are decisive factors in the choice of materials that best matches the requirements. Therefore, one cost effective way of improvement is to develop a new generation of metal matrix composites that can adapt in various harsh fields due to their upgraded performance.

Over the past decades, tungsten carbides cermet, containing as binder phase a cobalt-based alloy, were the materials that had been settled to lessen the degradation of the implemented PDC cutters and to protect the drilling bit body against corrosion and erosion. In either sintered or in a sprayed coating form, these materials have shown high anti-tribocorrosion properties combined with excellent toughness, hardness and strength. Their characteristics may be improved either by varying their chemical composition and the nature of the processing techniques, or by applying post-processing treatments. This improvement possibility had put them forward as exceptional candidate materials for the extreme drilling operations.

More recently, and beside the ongoing optimization on this kind of cermet, the fierce critics beyond the noxious cobalt effects on health and environment have promoted the exploration of novel alternatives that can exhibit more enhanced features and assure better functionality to the sintered and the coated parts. However, owing to the remarkable similarities between cobalt and nickel, in term of their physical properties, and the gap between their prices, the nickel self-fluxing alloys reinforced with tungsten carbides have won the favor [1-5].

Researchers tackled the microstructure of nickel self-fluxing alloys. Reinaldo and D'Oliveira [6] showed that in the case of Colmonoy coatings, the chemistry of the used steel substrates has a strong influence on coating performance. Depending on the deposition parameters, the microstructure of coatings may be of eutectic, dendritic or martensitic type. The more the dilution is low, the more the microstructure is complex, the more the coating is harder.

Gil, et al. [7] examined the microstructure of NiWCrBSiC coatings processed on 1020 steel substrates using the HVOF technique. The results revealed that the coating consists of a multiphase microstructure with inhomogeneous distribution of precipitates in a γ nickel matrix. The coatings also contain a set of hard precipitates embedded in a nickel-based matrix.

Hemmati, et al. [8] inferred that the rapid cooling rate promotes the nucleation and the growth of floret shape of nickel and chromium borides. They have also established that the proportion of NiBSi eutectic is influenced by the type of borides and can be affected by varying the amount of boron that remain in the melting pool.

Rodriguez, et al. [9] demonstrated that the post heat treatment using either oxy-acetylene flame, vacuum or

Manuscript received July 11, 2022; revised December 16, 2022.

R. AZZOUG and F. HELLAL are with Laboratoire science et génie des matériaux, Départment de Metallurgy, Ecole Nationale Polytechnique, Algiers, ALGERIA.
(e-mail: rabah.azzoug@g.enp.edu.dz, fatah.hellal@g.enp.edu.dz).

Y. MEBDOUA is with The Center for the Development of Advanced Technologies, Algiers, ALGERIA. (e-mail: ymebdoua@cdta.dz).

Digital Object Identifier (DOI): 10.53907/enpesj.v2i2.107

argon atmosphere can significantly affect the microstructure and increase the hardness and the density of NiCrBSiW (Colmonoy 88) coatings deposited via HVOF process.

Tokarev [10] studied the heat treatment of plasma sprayed coatings. The author inferred that the use of intense heat sources increases the efficiency of deposition for the treatment of the coatings.

Serres, et al. [11] proved that with diode laser source associated with an APS plasma gun induce a laser remelting that densify the deposits and promote the formation of dendritic microstructure. The laser remelting contributes to the increase of adhesion, hardness and elastic modulus of the coatings.

Zhang, et al. [12, 13] confirmed that the addition of tungsten carbides decreases the size of the dendritic crystal and the eutectic.

Liyanage, et al. [14] showed that the coatings obtained via plasma transferred arc welding exhibit a multiphase microstructure consisting of Ni dendrites with harder eutectics and chromium based borides. They demonstrated that the change in chemical composition of the NiCrBSi alloy could disturb the formation of different phases.

Sudha, et al. [15] revealed the existence of three regions in the overlays, depending on the distance from the interface.

Sidha, et al. [16] showed that thermally sprayed HVOF coatings on Fe-based superalloy~~.~~ The study the coatings had a layered microstructure. For NiCrBSi, Cr_3C_2-NiCr, Ni-20Cr, the principal phase was a nickel-base phase while in the case of Stellite-6 coatings, the main phase was a cobalt-rich matrix. The coatings are also characterized by the presence of inclusions, porosities (<2%) and unmelted or partially unmelted particles.

Otsubo, et al. [17] concluded that Fe_2B borides of lumpy shape can be formed near the interface. Owing to the interdiffusion, the formation of this type of borides doesn't affect the increase of adhesion.

Currently, the focus of research is to improve the nickel based self-fluxing coating to be more efficient under the more severe and aggressive conditions [18].

The aim of this study is to characterize the microstructure, the mechanical and the electrochemical behavior of a flame sprayed nickel based composite coating which will be used to cover the drilling bits in the Algerian fields.

II. EXPERIMENTAL PROCEDURE

A. *Presentation of the studied materials*

To carry out this study, we have used X18 carbon steel as substrates and MB40 powder as coating material for performing the bonding layer. We have also used a NiFeCrBSi-WC composite wire to realize the deposits. The feedstock wire contains WC particles that are embedded in NiFeCrBSi powder. The steel substrates have 50 mm in diameter and 5mm in thickness. They were cut from rods which had 60 mm in diameter.

B. *Spraying conditions*

Before the thermal spraying, the steel substrates were cleaned from any oxide, oil, grease, impurity or other material deposited thereon with a chemical solvent (acetone) so as to avoid the formation of defects.

The realization of coatings was performed in the open atmosphere using the acetylene as fuel. The selected processing parameters for both the bond layer deposition and the flame spraying are listed in Table I. The coating operation of samples for their protection against wear was carried out with an oxyacetylene torch, type TECHNOKIT T2000 (Fig.1). This type of coating is simple and economical and preserves the integrity and the integrality of the tungsten carbides.

Table. I
FLAME SPRAYING PARAMETERS

Parameters	Estimated values
Torch velocity (mm/s)	1
Spray distance (mm)	120
Acetylene pressure (bar)	0.2
Oxygen pressure (bar)	4

Fig. 1: TECHNOKIT T2000 torch.

C. *Metallographic Characterization*

The samples are first mechanically polished with a series of SiC silicon carbide abrasive papers and then on a felt paper impregnated with a dilute suspension of colloidal alumina.

A chemical etching in aqueous solution of Murakami reagent (10g $K_3Fe(CN)_6$ + 10g KOH/NaOH + 100 ml water) was performed at room temperature for a period of 180 seconds to reveal the coating microstructure. This chemical reaction reveals the nickel grains in dark gray, the nickel dendrites in light gray and the pores in black.

The micrographic analysis was carried out using a scanning electron microscopy (SEM).

D. *Mechanical characterization*

The micrographic examinations after spraying are supplemented with micro-hardness, and nano-indentation tests.

For the micro-hardness measurements, a charge of 0.1 Kgf was used to perform the filiation from the substrate to the top coating surface using a step of 50 µm. The dwell time was 15 s.

In our study, the nano-indentation tests were performed using a Vickers indenter according to Olivier and Pharr method. The maximum charge used for the measurements was 100 µN. The indentation velocity was kept at 2500 nm/min. At the maximum charge, the dwell time was 10 s. The charge and discharge velocity was 200 µN/min.

E. *Electrochemical characterization*

To characterize the corrosion behavior of the coatings in the NaCl and Na_2SO_4 solutions potentiodynamic measurements were conducted at different concentrations (1 g/l, 10 g/l, and 35 g/l) and that, at ambient temperature.

We carried out tests of polarization in a conventional three-electrode cell (Figure 9). Data acquisition from the potentiostat is done via the VoltaLab software.

In each manipulation, we waited for the measurement of open circuit potential for a period of 30 minutes before starting the test. For these tests, the potential range chosen is between [-1000, 0 mV]. The scanning speed is 0.2 mV/s which implies a duration of 30 min.

The electrochemical impedance measurements were performed at open circuit potential at a sine perturbation amplitude of 10 mV and that between 100 kHz and 1 Hz of frequency. For these measurements, the acquisition rate was fixed at 5 per decade and the open circuit stabilization time was set at 30 min.

III. RESULTS AND DISCUSSION

A. *Microstructural Analysis*

Fig.2 represents the microstructure of the coating matrix. It appears from this microstructure that the feedstock material was propelled to form a dendritic nickel matrix, in which, the tungsten carbides are embedded. The dendritic matrix was completely melted and the presence of dendrites (light grey color) is due to the slow cooling rate. During the cooling, the dendrites were preferentially initiated around tungsten carbides. They then grow before the solid precipitation took place. This solid precipitation is the cause of formation hard chromium carbides (grey color) which take place in the nickel grains (dark grey color). Due to the optimized processing parameters, no micro-cracks were observed. The pores that appear in black color have an irregular form and are distributed in-homogeneously within the matrix. Due to self-fluxing effect of boron and silicon, the oxides are not present in this matrix. The inter-splats boundaries were completely eliminated. Indeed, the spraying torch moves at low speed which provide an excessive heat to remelt the coating.

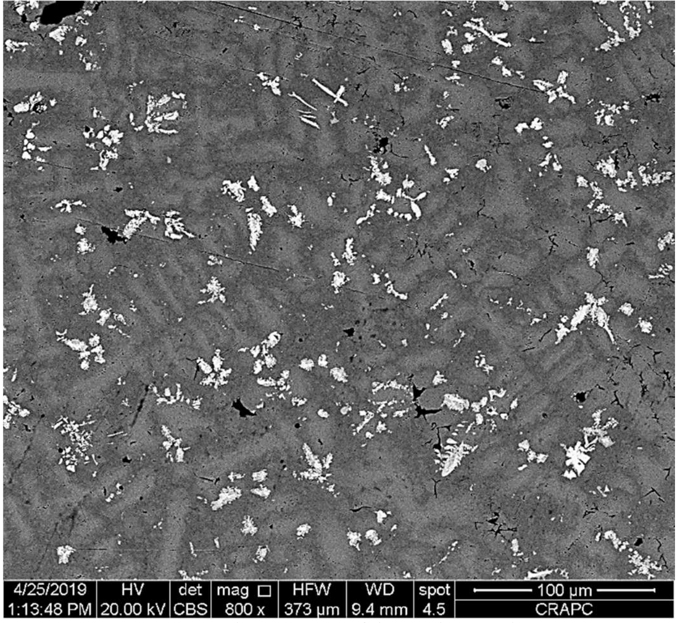

Fig. 2: Microstructure of the coating matrix.

B. *Mechanical characterization*

Fig. 3 illustrate the results of the microhardness measurement undergone on the cross section of coatings B. The results demonstrate the inhomogeneity of the coatings due to the presence of carbides. Even though the mean hardness of the matrix doesn't exceed 470 HV, the matrix is characterized by the presence of zones of carbides with relatively high hardness (500HV to 700 HV). During these tests, the indenter was not able to touch the WC carbides. However, the areas which surround the WC particles are characterized by high hardness (900 HV).

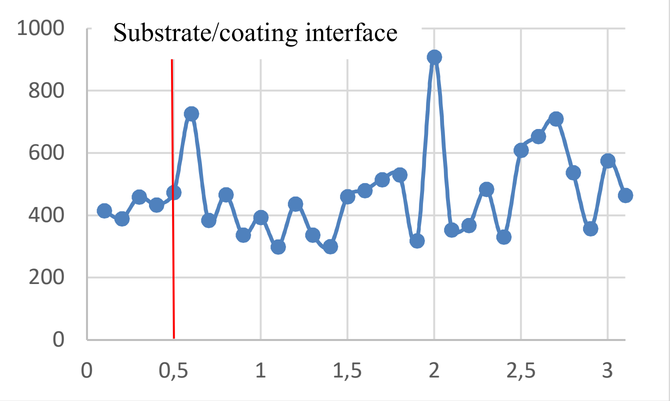

Fig. 3: Micro-hardness evolution profile of the cross section of the coating.

Fig 4. represents the load displacement curve obtained after nanoindentation of the coating matrix.

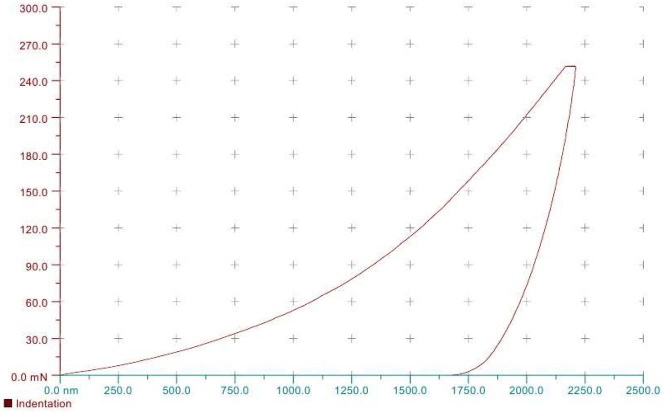

Fig. 4: Load displacement curve obtained after nanoindentation of the coating matrix.

The elastic modulus of the matrix is equal to 112.87 GPa. The hardness was about 272.29 HV.

C. *Electrochemical characterization*

Fig.5 and Fig.6 represent the potentiodynamic polarization curves obtained after the electrochemical characterization.

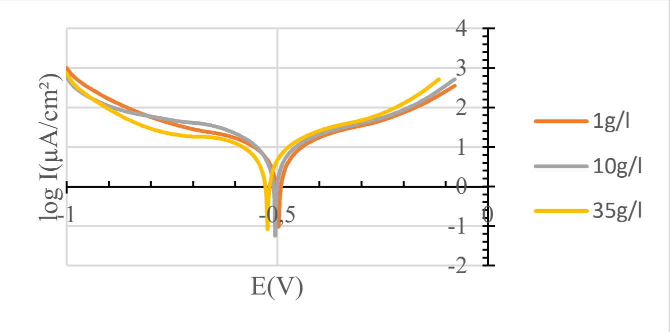

Fig. 5: Potentiodynamic polarization curves gotten in NaCl solutions.

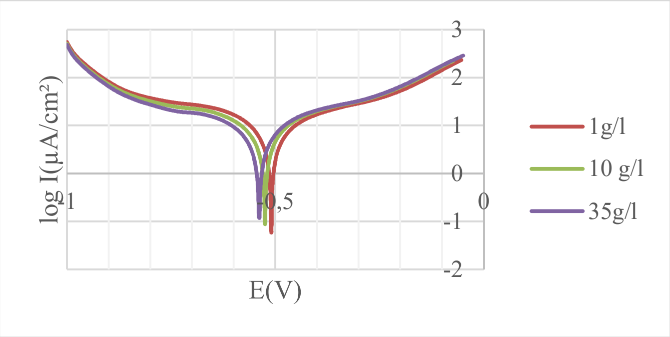

Fig. 6: Potentiodynamic polarization curves gotten in Na_2SO_4 solutions.

The extracted electrochemical data from the previous curves are summarized in Table II and Table III. It's clear that the corrosion current increased with the increase of the ionic concentrations. The corrosion potential shift from –505 mV in NaCl solution with 1g/l of concentration toward the more negative values to reach -524.2 mV with 35 g/l NaCl of concentration. The corrosion rate varies between 5.983 µm/year and 28.78 µm/year in this range of concentration.

In Na_2SO_4, the corrosion potential decreased from -509.5 mV at 1g/l of concentration to 524.5 mV at 10 g/l to reach a value of -539.5 mV. The corrosion current increased gradually and is between 1.3750 µA/cm² and 2.2501 µA/cm². In the given range of concentration, the corrosion rate increased gradually from 16.98 µm/year to 22.63 µm/year.

Table. II

THE EXTRACTED ELECTROCHEMİCAL DATA FOR THE COATİNG İN NACL

C_{NaCl} (g/l)	1	10	35
E_{corr} (mV)	-505.0	-506.1	-524.2
I_{corr} (µA/cm²)	0.7471	2.1748	2.5970
V_{corr} (µm/year)	5.983	25.53	28.72

Table. III

THE EXTRACTED ELECTROCHEMİCAL DATA FOR THE COATİNG İN NA_2SO_4

C_{NaCl} (g/l)	1	10	35
E_{corr} (mV)	-509.5	-524.5	-539.5
I_{corr} (µA/cm²)	1.3750	2.1378	2.2501
V_{corr} (µm/year)	16.98	20.30	22.63

Fig.7 shows the Nyquist plot gotten after an Electrochemical Impedance Spectroscopy in NaCl solutions. The semi-circles are capacitive, suggesting that there was adsorption of ions during the tests.

It results from the same figure that the increase in ion concentration decreases the charge transfer at the interface between the coating and the electrolyte.

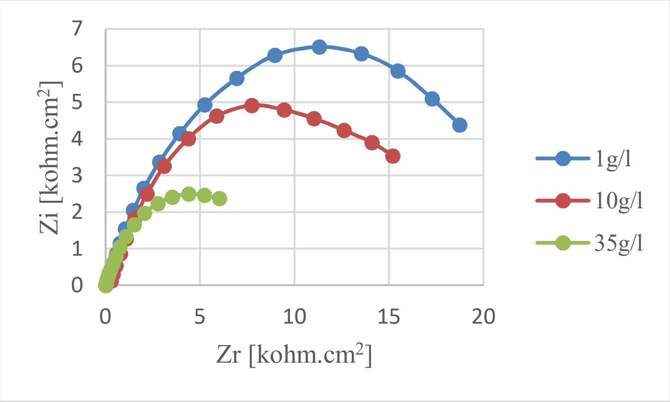

Fig. 7: EIS spectrum obtained in NaCl solutions.

From Fig.8, it results that the increase of ion concentration induced an increase in the radius of the impedance semi-circles toward a constant value due to passivation of coating. The coating forms then a compact passive film that protects it against the sulfur ions.

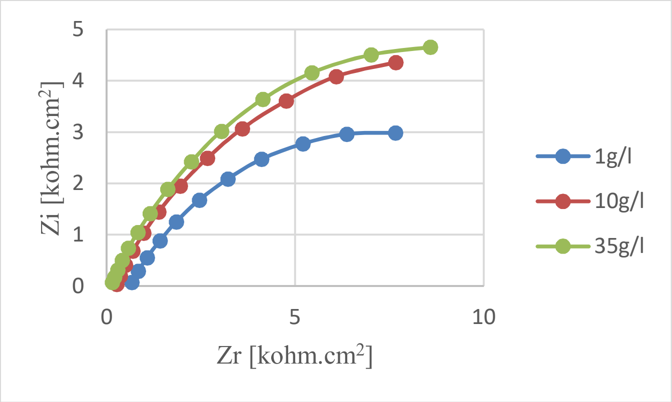

Fig. 8: EIS spectrum obtained in Na_2SO_4 solutions.

As compared to Rabah et al [19] findings, it results that the corrosive behavior of this coating is better.

IV. CONCLUSION

It can be concluded that the coating is composed of dendritic γ nickel matrix which is characterized by the presence of chromium carbides and γ nickel grains in the inter-dendritic regions.

The mechanical indentation behavior is governed by the plasticity of the indented phases. The microhardness of the matrix is about 470 HV. However, it can reach 900HV due to the decarburization of WC particles. The elastic modulus of the matrix is about 112.87 GPa.

The coating shows good resistance in NaCl and Na_2SO_4 aqueous solutions due to the presence of WC particles as reinforcement. For that reason, it can be used to cover the drilling bits in the exploited Algerian oil and gas fields. Nevertheless, actual tests must be carried out, using these coated drilling tools, in different prospecting sites, taking into account the rock encountered formations and the operational drilling conditions.

REFERENCES:

[1] A. Wong et al. New material technologies reduce PDC drill bit body and cutter erosion in heavy oil drilling environments. in SPE Latin America and Caribbean Heavy and Extra Heavy Oil Conference. 2016. OnePetro. https://doi.org/10.2118/181196-MS

[2] X. Ren, H. Miao and Z. Peng, A review of cemented carbides for rock drilling: an old but still tough challenge in geo-engineering. International Journal of Refractory Metals and Hard Materials, 2013. 39: p. 61-77. https://doi.org/10.1016/j.ijrmhm.2013.01.003

[3] C.-J Li and G.-J. Yang, Relationships between feedstock structure, particle parameter, coating deposition, microstructure and properties for thermally sprayed conventional and nanostructured WC–Co. International Journal of Refractory Metals and Hard Materials, 2013. 39: p. 2-17. https://doi.org/10.1016/j.ijrmhm.2012.03.014

[4] Z Izdinska, A. Nasher and K. Izdinsky, The structure and properties of composite laser clad coatings with Ni based matrix with WC particles. Materials engineering, 2010. 17(2): p. 1.

[5] J. ŠKAMAT et al., Improving hardness of Ni-Cr-Si-B-Fe-C thermal sprayed coatings through grain refinement by vibratory treatment during refusion. Mat Sci/Medziagotyra, 2015. 1(2). http://dx.doi.org/10.5755/j01.mm.21.2.6833

[6] P.R. Reinaldo and A.S.C.M. D'Oliveira, NiCrSiB Coatings Deposited by Plasma Transferred Arc on Different Steel Substrates. Journal of Materials Engineering and Performance, 2013. 22(2): p. 590-597. https://doi.org/10.1007/s11665-012-0271-7

[7] L. Gil et al., *Microstructural characterisation of NiWCrBSiC alloy coating produced by HVOF thermal spraying.* Surface Engineering, 2006. **22**(4): p. 304-313. https://doi.org/10.1179/174329406X122900

[8] I. Hemmati et al., *Microstructure and Phase Formation in a Rapidly Solidified Laser-Deposited Ni-Cr-B-Si-C Hardfacing Alloy.*

Metallurgical and Materials Transactions A, 2014. 45(2): p. 878-892. https://doi.org/10.1007/s11661-013-2004-4

[9] M.A. Rodríguez, L. Gil and M.H. Staia, *Post-Heat Microstructural Treatment Changes in Nickel Based Hvof Coating.* Surface Engineering, 2002. 18(5): p. 358-362. https://doi.org/10.1179/026708402225006213

[10] A.O. Tokarev, *Treatment of Wear-Resistant Metallic Coatings with Highly Concentrated Energy Sources.* Metal Science and Heat Treatment, 2001. 43(1): p. 61-64. https://doi.org/10.1023/A:1010478408048

[11] N. Serres et al., *Microstructures of Metallic NiCrBSi Coatings Manufactured via Hybrid Plasma Spray and In Situ Laser Remelting Process.* Journal of Thermal Spray Technology, 2011. 20(1): p. 336-343. https://doi.org/10.1007/s11666-010-9565-1

[12] Y.M. Zhang et al., *Influence of WC addition on microstructures of laser-melted Ni-based alloy coating.* Journal of Materials Engineering and Performance, 2002. 11(6): p. 667-674. https://doi.org/10.1361/105994902770343674

[13] Y.M. Zhang et al., *Effect of WC addition on microstructures of laser melted Ni-based alloy powder.* Surface and Coatings Technology, 2003. 169-170: p. 384-387. https://doi.org/10.1016/S0257-8972(03)00058-6

[14] T. Liyanage, G. Fisher and A.P. Gerlich, *Influence of alloy chemistry on microstructure and properties in NiCrBSi overlay coatings deposited by plasma transferred arc welding (PTAW).* Surface and Coatings Technology, 2010. 205 (3): p. 759-765. https://doi.org/10.1016/j.surfcoat.2010.07.095

[15] C. Sudha et al., *Microchemical and microstructural studies in a PTA weld overlay of Ni–Cr–Si–B alloy on AISI 304L stainless steel.* Surface and Coatings Technology, 2008. 202 (10): p. 2103-2112. https://doi.org/10.1016/j.surfcoat.2007.08.063

[16] T.S. Sidhu, S. Prakash and R.D. Agrawal, *Performance of high-velocity oxyfuel-sprayed coatings on an fe-based superalloy in Na2SO4-60%V2O5 environment at 900 °C Part I: Characterization of the coatings.* Journal of Materials Engineering and Performance, 2006. 15(1): p. 122-129. https://doi.org/10.1361/105994906X83402

[17] F. Otsubo, H. Era and K. Kishitake, *Interface reaction between nickel-base self-fluxing alloy coating and steel substrate.* Journal of Thermal Spray Technology, 2000. 9 (2): p. 259-263. https://doi.org/10.1361/105996300770350014

[18] R. Azzoug, F. Hellal and Y. Mebdoua, *Microstructural Analysis of Nickel-Based Composite Coatings and Their Effect on Micro-hardness and Nano-indentation Behavior*, in *Computational Methods and Experimental Testing In Mechanical Engineering*. 2019, Springer. p. 51-62. https://doi.org/10.1007/978-3-030-11827-3_6

[19] R. Azzoug et al., *Analysis of microstructure, mechanical indentation and corrosive behavior of a thermally sprayed NiFeCrBSi-WC composite coating.* Journal of Alloys and Compounds, 2022. 900: p. 163505. https://doi.org/10.1016/j.jallcom.2021.163505

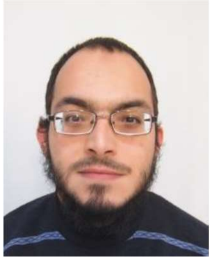

Rabah AZZOUG received his materials engineering diploma and master degree from the Ecole Nationale Polytechnique of Algiers. He received his Ph.D. from the same school in 2022. His research interest includes the characterization of newly designed composites, stainless steels, nanomaterials and nanocomposites. He is also interested in the lithium batteries. He is the first author of several scientific articles.

Yamina MEBDOUA is working as a director of research, head of the thermal spraying technology platform at the Center for Development of Advanced Technologies (CDTA) and a member of the Scientific Council (CS) of this establishment. She completed her Magister of astrophysics from Saad DAHLAB University - Blida. She received her Ph.D in physics in 2008 from Limoges University - France, followed by a university habilitation (HDR) from Saad DAHLAB University - Blida. She possesses several years of experience in research activity in the field of plasmas and thermal spraying at the CDTA. She trained a research team on thermal spraying and set up a technological platform for thermal spraying processes. She also headed a research division on ionized media and lasers (DMIL) at the CDTA during three years. She has led several research projects: on the design of a microwave plasma reactor for surface treatment application, on the applications of thermal spraying in surface treatment and on the development of thermal barrier coatings on industrial parts, a project with socio-economic impact. She has numerous publications on these processes but also on transversal subjects through PhD supervision.

Fatah HELLAL received his Engineer-doctor diploma in Material Science and Engineering in 1987, from the National Polytechnic Institute of Lorraine, Nancy, France. He received his PhD in Metallurgy in 2001, from the Ecole Nationale Polytechnique, Algiers, Algeria. He is currently professor at the Department of Metallurgy, and Research Director in the Laboratory of Material Science and Engineering at the Ecole Nationale Polytechnique. His fields of interest are material structure and properties, electrochemistry, stainless steels behaviour, coupled phenomena, Image analysis.

Mesophilic anaerobic co-digestion of cheese whey with cow manure in batch reactor

Nassima Tirichine, Meryem Saber, Mohamed Khitous, Hakim Lounici, and Rabah Bouarab

Abstract− Anaerobic digestion is a biological process that takes place under very strict operating conditions, including a pH close to neutrality. This experimental work aims to study the effect of pH control on CH_4 production in mesophilic anaerobic co-digestion of cheese whey with cow manure. Two experiments were conducted in batch reactor, the first without pH adjustment and the second with pH adjustment. The results of the first co-digestion revealed an inhibition of the methanization process by acidification of the medium and accumulation of volatile fatty acids; whereas during the second co-digestion with pH adjustment using sodium bicarbonate (1M), the process was improved with methane levels (> 50%) in the biogas. The accumulated biogas volume was two times higher for the same operating time in the digester.

***Keywords*− Cheese whey, anaerobic co-digestion, pH control, cow manure, biogas.**

NOMENCLATURE

CW	Cheese Whey.
CM	Cow Manure.
TS	Total Solids.
VS	Volatile Solids.
Eh	Redox Potential.
COD	Chemical Oxygen Demand.
At	Total Alkalinity.
VFA	Volatile Fatty Acids.
DI	Digester I.
DII	Digester II.

I. INTRODUCTION

Cheese whey is the main waste or effluent generated by the dairy industry, and it has a very high organic matter content ranging from 57 to 140 g COD/L [1-3]. Therefore, the disposal of this by-product is a challenge for small and medium enterprises (SMEs) in the dairy industry that do not have any type of processing plant [2]. Indeed, the dairy industries annually produce hundreds of millions of kilograms of milk and derivatives, with world production estimated at 190 billion kg per year [4]. If we consider FAO statistics, cheese production (all kinds of cheese) reached 27,634 t in 2018, generating around 41,162 t of whey [5]. Anaerobic digestion is a particularly interesting solution for treating or pre-treating this effluent, because it offers an excellent solution both in terms of energy savings and depollution; whey processed through anaerobic digestion produces biogas which is considered valuable energy that can be converted into heat and electricity [1, 6, 7]. Some studies have been carried out with whey as a substrate or co to study anaerobic digestion, in particular those carried out by [1-2, 8-12]. However, some difficulties have been reported regarding the anaerobic digestion of cheese whey. The majority of these difficulties are due to the low alkalinity and rapid acidification of cheese whey which can deplete buffering capacity, leading to lower pH, buildup of volatile fatty acids (VFAs) and subsequent reactor failure [1, 7, 13, 14]. In this research work, we studied a very important parameter in anaerobic digestion which is the pH. For this, two digesters were started, one without pH correction and the second with pH correction using sodium bicarbonates. The whey was co-digested with cow manure as an inoculum or source of anaerobic bacteria. Various parameters have been monitored and analyzed and characterization methods are carried out in order to monitor the behavior of the digester over time.

MATERIELS AND METHODS

A. Substrates

The effluent studied is the soft cheese whey generated by cheese dairy of Boudouaou (Algeria). It is made from a pressed cheese (Edam) and is still very rich in nutrients. Samples were taken from the coagulation tank and stored in 1 L plastic jerrican at 4°C until analyzed and processed in laboratory. Before each experiment, the substrate is removed from the freezer and defrosted at room temperature during 24 h. The cow manure used in this study comes from a private farm located in Bouzareah (Algeria).

The samples were made of fresh cow manure, and was directly weighed and put in the digesters. It is considered as an inoculum because it contains the microorganisms that will be used to degrade the nutrients contained in the whey. The main characteristics of cheese whey and cow manure are reported in Table I.

According to Table I, the whey contains a very high pollutant load, represented by a COD of 134 g O_2/L and has a fairly high level of fermentable organic solids, represented by the VS which is 98.3% [% MS]; which makes it a good substrate for producing biogas.

Manuscript received October 25, 2022; December 18, 2022.

N. Tirichine, M. Saber and M. Khitous are with the Centre De Développement Des Energies Renouvelables, Bioenergies et Environnement division, Algiers, Algeria (e-mails: n.tirichine@cder.dz, m.saber@cder.dz, m.khitous@cder.dz)

H. Lounici is with the Centre Universitaire de Bouira, Algeria (e-mail: hakim_lounici@yahoo.ca)

R. Bouarab is with Ecole Nationale Polytechnique, Département de Génie Chimique, Laboratoire de Valorisation des Energies Fossiles. (e-mail: rabah.bouarab@g.enp.edu.dz)

Digital Object Identifier (DOI): 10.53907/enpesj.v2i2.171

Table. I
Physicochemical characteristics of cheese whey and manure

Parameters	Cheese Whey	Cattle Manure
pH	6.4	8.1
Eh (mV)	23.1	-69.1
TS (%)	7	16
VS (% of TS)	98.3	86.7
COD (g L^{-1})	134	17.4
At (mg L^{-1})	-	1040
VFA (mg L^{-1})	37	11

B. *Analytical methods*

The system performance was tested by measuring biogas and methane productions, COD removing, total solids (TS), volatile solids (VS), total alkalinity At, pH, potential redox (Eh) and volatile fatty acids (VFA) concentrations. The influent and effluent pHs were measured from samples with a glass electrode pH meter (WTW InoLab pH Level 1). The total alkalinity (At) and the volatile fatty acids (VFA) were determined by titration at a pH of 4 and 3.5, respectively, according to the method described by Anderson [15]. All of the other analyses TS, VS, and COD were performed according to the Standard Methods [16, 17]. Biogas production of the system was determined daily by water displacement gas meter designed as a scaled measuring cylinders. Methane content biogas was measured using a gas analyzer Multitec 540.

C. *Experimental setup*

Experimental studies were performed in anaerobic reactor with a total volume of 5 L (Figure 1). The reactor was heated with water bath equipped with a temperature controller (LAUDA E200) to maintain a constant temperature of 38 °C. After that cheese whey and cow manure were filled to the reactor at 50/50 (V/V) with water, the reactor inlet was closed to prevent air leakage. After 24 hours, we start the samples in the two digesters and the monitoring of the parameters.
The biogas produced is measured with a gas meter and stored in a special bag for analysis by a biogas analyzer.

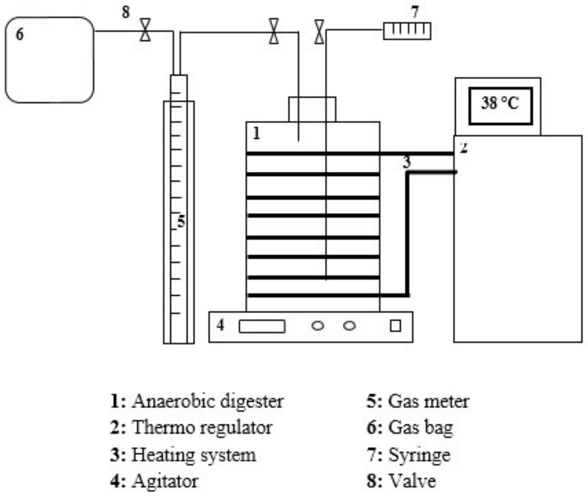

Fig. 1. Experimental set-up: Anaerobic digester (5L), gas meter (250mL) and storing bag (2L)

D. *Digester Startup*

The physico-chemical characteristics of the two digesters before starting are given in Table II. The two experiments were, carried out in order to study the effects of pH on the reactor performances.
According to Table II, we notice that the mixture of cheese whey at 7% TS, and cow manure at 16% (Table I) with water, gives us TS of 7% for both digesters DI and DII.

Table. II
Main characteristics of digester I and digester II

Parameters	Digester I	Digester II
pH	6.5	6.5
Eh (mV)	-8.7	-8.1
TS (%)	7	7
VS (% of TS)	87.1	87.1
COD (g L^{-1})	35. 319	35. 182
At (mg L^{-1})	1600	1400
VFA (mg L^{-1})	1.02	2.4

II. RESULTS AND DISCUSSION

A. *pH control and measurement*

pH of raw cheese whey and cow manure was 6.4 and 8.1 respectively (Table I). Mixing the two substrates with water gives us a pH of 6.5 in DI and DII (Table II). No adjustment was made for the pH in the first digester whereas the pH in the second digester was adjusted to the setpoint of 6.0 by the addition of 1M sodium bicarbonate solution.

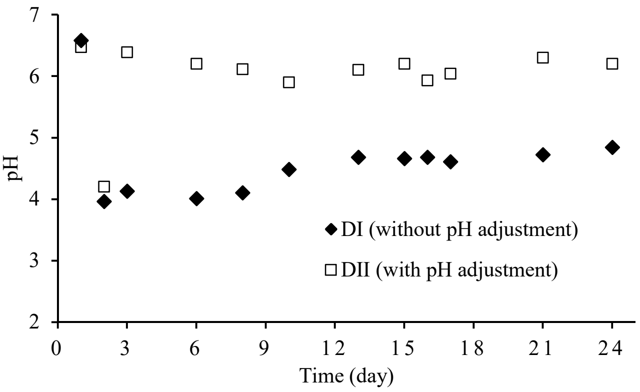

Fig. 2. pH behavior during anaerobic co-digestion of cow manure and cheese whey with and without pH adjustment

Fig. 2 shows the evolution of pH for both anaerobic co-digestion processes (without and with adjustment of pH). For first experiment, the pH decreased with time reaching 3.96 after 48 hours and then remained around values between 4.01 and 4.84. For the experiment with adjustment of pH, the pH decreased reaching 4.2 before adding sodium bicarbonate. However, when the 1M of sodium bicarbonate was added to digester, the pH increased with time reaching an average value of 6.39 after 3 days.

B. Redox evolution

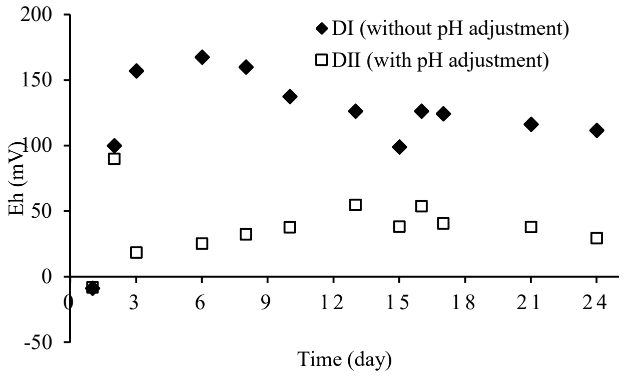

Fig. 3. Eh behavior during anaerobic co-digestion of cow manure and cheese whey with and without pH adjustment

Figure 3 shows the evolution of the redox potential for the two experiments. At start-up, the reduction potentials (Eh) were -8.7 mV and -8.1 mV for DI and DII, respectively. After 48 hours of anaerobic co-digestion, the potentials reached 100 and 90 mV for DI and DII, respectively. After 72 hours, the redox potential increases to 157 mV in the unadjusted digester (DI), and decreases to 18.5 mV in the adjusted digester (DII). This last value indicates correct bacterial activity in the digester (DII). This result is similar to that given by the literature where reduction potentials of 0 to 50 mV are generally measured for digesters in full activity [18].

C. VFA control

Volatile fatty acids are short chain fatty acids derived from microbial fermentation during anaerobic digestion. They are in continuous production and consumption during anaerobic digestion, and their monitoring can help us delineate the different stages of anaerobic digestion. Indeed, a too high concentration of VFA is toxic for bacteria and harms the proper operation of the digester hence the importance of their control.

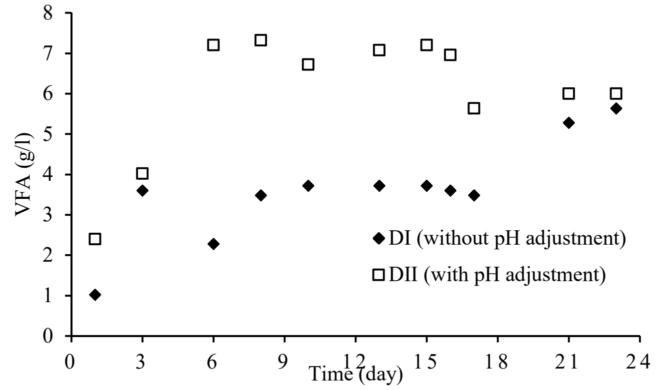

Fig. 4. VFA behavior during anaerobic co-digestion of cow manure and cheese whey with and without pH adjustment

Fig. 4 illustrates volatile fatty acids concentration evolution (expressed in g/L) as a function of the co-digestion time. The evolution curve of the VFA in the digester I, without pH adjustment can be divided into two phases; Phase 1, observed during first 3 days of digestion, with high production of VFA from 1 g/L to 3.6 g/L. This phase corresponds to the hydrolysis and acidogenesis phase; Phase 2, during this phase, the AGV values remained low, around 3 g/L from the 8th to the 17th day, with a maximum of 5.64 g/L on the 23rd day. This is due to the stopping of whey hydrolysis and acetogenesis as well, which led to an inhibition of the methanation process. As a result, a slowing and stopping of CH_4 production was recorded (Fig. 6). While the evolution of VFA in the digester II, with pH adjustment can be divided into three phases; Phase 1, observed during the first 6 days since the beginning of digestion, with a high production of VFA (from 2.4 g / L on the first day to 7.2 g/L on the 6th day). This phase corresponds to the hydrolysis and acidogenesis reactions. Phase 2, starts from the 6th to the 15th day when stabilization of VFA concentrations around 7.2 mg/L is observed. It is the acetogenesis phase; Phase 3, from the 15th day, the VFA concentrations decrease from 7.2 to 5.64 mg/L. This phase corresponds to the beginning of methane production (Fig. 6). This is the methanogenesis phase.

D. Alkalinity

The total alkalinity of an anaerobic digester is a measure of its ability to neutralize excess of organic acids and maintain a constant pH [14].

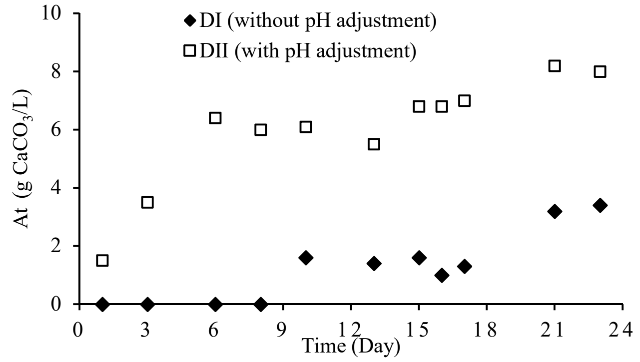

Fig. 5. At behavior during anaerobic co-digestion of cow manure and cheese whey with and without pH adjustment

For an operational digester, a total alkalinity of 2.5 to 5 g/L $CaCO_3$ is recommended [19] According to Grady and Lim (1980) [20], the use of sodium bicarbonate to control pH can have toxic effects that will inhibit microorganisms if the concentration exceeds 8000 ppm sodium (the equivalent of 8 g/L). In digester II (with pH adjustment with 1M sodium bicarbonate), although total alkalinity values of 8 and 8.2 g $CaCO_3$ /L were observed, there was no apparent inhibition by the sodium ion as indicated by the methane production fig. 6 with a methane content of 45%. These results are similar to those obtained by Ghaly (1999) [14]. Because total alkalinity is the sum of all alkali elements, it varies significantly with the endpoint of the pH used [14]. The pH values in digester I (without pH control) being less than or close to 4.5, the total alkalinity was therefore zero during the first 8 days. Then the alkalinity increases gradually until reaching 3.4 g/L after 23 days of anaerobic co-digestion. This is explained by the buffering power of cow manure which tends to neutralize the acidified medium.

E. Biogas and methane production

The fig. 6 shows the cumulative volume of biogas and methane levels produced by both anaerobic co-digestion of whey with cow manure (with and without pH adjustment). The total biogas production obtained by the digester II is much higher than that obtained by the digester I; it reached 11.5 L for the digester II and 5.7 L for the digester I. This difference is due to the different behaviors of the two digesters: the evolution of the pH, the alkalinity and the VFA concentration.

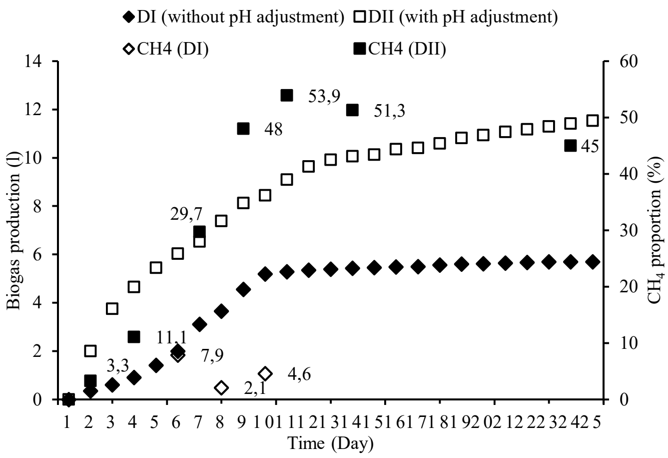

Fig. 6. Process performance during anaerobic co-digestion of cow manure and cheese whey with and without pH adjustment

Methane production

In the digester II, where we made regular pH adjustments, the methane content gradually increased over time to reach a maximum of 53.9% on the 11th day of anaerobic digestion, and 51.3% on the 15th day. While in the first digester, the methane content reached a maximum of 7.9% on the 7th day, and then dropped to 2.1% after the 8th day, stopping abruptly after 10 days of anaerobic digestion, due to the process inhibition.

In conclusion, the digester II worked properly including the four phases of the anaerobic digestion process. This is mainly due to the control and adjustment of the pH.

III. CONCLUSION

The effect of pH adjustment by the use of sodium bicarbonate on the performance of a mesophilic anaerobic digester was studied. It has been found necessary to control the pH of the digester during anaerobic co-digestion of acid whey with cow manure. Without pH control, the very low pH (3.3) inhibited the methanogenic process and the biogas produced contained very little methane. The pH inhibition of the methanogens was irreversible and the digester I did not recover (no methane production). While in the second digester, where we made adjustments, the pH was restored, and it was able to increase the methane production in the biogas, until 50% of CH$_4$. As a result, the biogas production reached 11 L in 25 days with a maximum methane content of 54% after the 11th day of co-digestion.

REFERENCES

[1] C. Rico, N. Munoz, JL. Rico, "Anaerobic co-digestion of cheese whey and the screened liquide fraction of dairy manure in a single continuously stirred tank reactor process: Limits in co-substrate ratios and organic loading rate", *Bioresour. Technol.*, vol.189, pp.327–333, 2015, DOI: 10.1016/j.biortech.2015.04.032

[2] H. Escalante, L. Castro, M.P. Amaya, L. Jaimes, J. Jaimes-Estévez, "Anaerobic digestion of cheese whey: Energetic and nutritional potential for the dairy sector in developing countries", Waste Management, 2017, DOI: 10.1016/j.wasman.2017.09.026

[3] N. Tirichine, M. Khitous, M. Saber, H. Lounici, R. Bouarab, "Improved anaerobic digestion performances of whey in a batch reactor", *Algerian J. Env. Sc. Technology*, vol.6, N°.4, pp. 1612-1619, 2020.

[4] F. Asunis, G. De Gioannis, P. Dessì, M. Isipato, P. N.L. Lens, A. Muntoni, A. Polettini, R. Pomi, A. Rossi, D. Spiga, "The dairy biorefinery: Integrating treatment processes for cheese whey valorization", *Journal of Environmental Management*, vol.276, pp. 1-15, 2020, DOI: 10.1016/j.jenvman.2020.111240

[5] Food and Agriculture Organization of the United Nations FAOSTAT |© OAA Division de la Statistique, 2018.

[6] P.A. Ferreira, S.C. Santos, I. Kimiko, M.B. Amâncio, E. Luiz Silva, "Hydrogen production from cheese whey with ethanol-type fermentation: effect of hydraulic retention time on the microbial community composition", *Bioresour. Technol.*, vol.161, pp. 10–19, 2014.

[7] TH. Erguder, U. Tezel, E. Guven, GN. Demirer, "Anaerobic biotransformation and methane generation potential of cheese whey in batch and UASB reactors", *Waste Manag.*, vol.21, N°7, p.643-650, 2001, DOI: 10.1016/S0956- 053X (00)00114-8

[8] E. Comino, M. Rosso, V. Riggio. "Development of a pilot scale anaerobic digester for biogas production from cow manure and whey mix". *Bioresour. Technol.*, vol.100, pp.5072–5078, 2009, DOI: 10.1016/j.biortech.2009.05.059

[9] B. Kavacik, B. Topaloglu, "Biogas production from co-digestion of a mixture of cheese whey and dairy manure", *Biomass and bioenergy*, vol.34, pp.1321-1329, 2010, DOI: 10.1016/j.biombioe.2010.04.006

[10] E. Comino, V. Riggio, M. Rosso, "Biogas production by anaerobic co-digestion of cattle slurry and cheese whey", *Bioresour. Technol.*, vol.114, pp.46–53, 2012, DOI: 10.1016/j.biortech.2012.02.090

[11] L. Bertin, S. Grilli, A. Spagni, F. Fava, "Innovative two-stage anaerobic process for effective codigestion of cheese whey and cattle manure", *Bioresour. Technol.*, vol.128, pp.779–783, 2013, DOI: 10.1016/j.biortech.2012.10.118

[12] M.V. Mainardis, V. Cabbai, G. Zannier, D. Visintini, D. Goi, "Characterization and BMP Tests of Liquid Substrates for High-rate Anaerobic Digestion", *Chemical and Biochemical Engineering Quarterly*, vol.31, N°.4, 2017, DOI: 10.15255/CABEQ.2017.1083

[13] S.V. Kalyuzhnyi, E. Perez Martinez, J. Rodriguez Martinez, "Anaerobic treatment of high-strength cheese-whey wastewaters in laboratory and pilot UASB-reactors", *Bioresour. Technol.*, vol. 60, p.59, 1997, DOI: 10.1016/S0960-8524(96)00176-9

[14] AE. Ghaly, DR. Ramkumar, "Controlling the pH of acid cheese whey in a two stage anaerobic digester with sodium hydroxide", *Energy source*, vol.21, N°.6, pp.475-502, 1999, DOI: 10.1080/00908319950014623

[15] GK. Anderson, G. Yang. "Determination of bicarbonate and total volatile acid concentration in anaerobic digesters using a simple titration". *Water Environment Research.* vol.64, N°.1, pp. 53-59 Water Environment Federation, 1992, DOI: 10.2175/WER.64.1.8

[16] APHA, "Standard Methods for the Examination of Water and Wastewater", 20th ed., *American Public Health Association. American Water Works Association and Water Environmental Federation*, Washington DC, 1998.

[17] APHA, "Standard Methods for the Examination of Water and Waste Water", 22n ed., *American Public Health Association. American Water Works Association*, Water Environment Federation, 2012.

[18] R. Moletta, "Gestion des problèmes environnementaux dans les IAA", Tech et Doc, Paris, 2002.

[19] EJ. Fox, CJ. Clanton, PR. Goodrich, BD. Backus, HA. Morris, "Liming an anaerobic cheese whey digester", *Transactions of the American Society of Agricultural and Biological Engineers*, vol.35, N°.1, pp.269-274, 1992, DOI: 10.13031/2013.28599

[20] CPL. Grady, HC. Lim, "Biological Wastewater Treatment", New York, NY: Marcel Dekker Inc, 1980.

Nassima Tirichine was born in Algiers, Algeria, in 1981. She received the Engineer Diploma degree from Ecole Nationale Supérieure d'Agronomie (ENSA), Algiers, in 2004, the Master degree from Ecole Nationale Polytechnique, Algiers, in 2011. She is currently a Researcher in Centre De Développement Des Energies Renouvelables (CDER) and Phd student at Ecole Nationale Polytechnique. Her current research interests include the production of biomethane, and anaerobic processes for energy conversion of waste and recovery of by-products.

Meryem Saber is Director of Research, and leader in Research Division of Bioenergy and Environment, at Renewable Energies Development Center, in Algiers. She received her doctorate in chemical engineering, in 2009, from National Polytechnic Institute of Lorraine - I.N.P.L., France, and her engineer and master degrees in chemical engineering sciences, in 2004 and 2005, respectively, from ENP and ECP. Most of Dr. Saber's papers and reports deals with issues related to anaerobic digestion of organic material.

Hakim Lounici currently works at the Department of Process and Environmental Engineering at BOUIRA University and researcher at Ecole Nationale Polytechnique, Algiers. Hakim does research in Environmental Chemistry, Analytical Chemistry and Green Chemistry. Their current project is 'Preparation, characterization and utilization of nanocomposite based bioresources.' He has authored or co-authored more than three hundred papers mainly in this research area.

Rabah BOUARAB is Professor at the Chemical Engineering Department, Ecole Nationale Polytechnique, Algiers. He has an experience of 26 years in the domain of hydrogen production. He has authored or co-authored more than forty papers mainly in this research area.

Survey and Classification of Hybrid GMPPT Techniques for Photovoltaic System under Partial Shading Conditions

Faiza Belhachat and Cherif Larbes

Abstract−A maximum power point tracking process is a very important task to harvest the maximum power available from a photovoltaic generator. For this reason, resorting to the development of new and more effective methods is an absolute necessity. Numerous advanced methods have been successfully employed to extract the real maximum point, such as neural networks and metaheuristic techniques. These techniques deal effectively in such conditions. However, the use of the algorithm alone has some limitations. In order to solve these drawbacks, the combination of two or more different techniques provides more advantages over single MPPT algorithms and improves the performance of the overall system. This paper mainly focus in reviewing the most important and recent hybrid global MPPT techniques proposed in the literature and proposes a classification of these methods with a comparison of their performances. All surveyed hybrid GMPPT methods are divided into four categories according to algorithms types involved in the MPPT method. This review study intends to make it easier for the user to make the convenient selection of which method to adopt especially in the presence of a variety of methods which are continuously developing in the literature.

***Keywords*− Photovoltaic, Hybrid, conventional algorithms, soft computing algorithms, GMPPT, Partial shading.**

NOMENCLATURE

PV	Photovoltaic.
PSC	Partial shading conditions.
HGMPPT	Hybrid Global Maximum Power Point Tracking.

I. INTRODUCTION

Partial shading (PS) causes significant reduction in power production in photovoltaic (PV) systems. The reduced effectiveness of partially shaded photovoltaic arrays is still a big barrier in front of the fast development of photovoltaic energy systems. Thus, reducing the mismatch of the output power and the partial shading effects is a primary task.

Extracting the maximum power from partially shaded photovoltaic array has been extensively studied in the literature. The negative effects of partial shadings can be resolved through different techniques. The most frequently used techniques to reduce the impact of partial shading are: bypass diode insertion to prevent PV cells from hotspot, PV system architecture, configurations and reconfiguration PV array schemes and maximum power point tracking (MPPT).

The maximum power point tracking strategy is considered a necessary means to gain the maximum energy in photovoltaic (PV) systems.

In fact, conventional methods have been widely used to extract the MPP, such as the P&O and INC algorithms. These algorithms work well under normal climatic conditions and find the MPP without difficulty since there is only one maximum. Nevertheless, the presence or the occurrence of the phenomenon of shading causes several maximum peaks in the characteristics of the PV module, which complicates the tracking task, therefore the need for the development of more efficient techniques able to differentiate the real maximum among the local maximums.

Partial shading in PV array makes conventional MPPT inefficient.

Different techniques GMPPT have already been developed in literature aiming to track in effective way the global maximum power point (MPP) under PS conditions.

In recent years, the application of bio-inspired and soft computing algorithms has been widely used thanks to their high efficiency in dealing with the problem of extracting the maximum power whatever the climatic operating conditions [1-2],[4], [6]. However, the use of the algorithm alone has some limitations which leads us to look for other more efficient algorithms.

In order to improve the performance of the algorithm and therefore the efficiency and yield of the whole system, the mixture of two or more algorithms makes it possible to increase them considerably since the disadvantage of an algorithm is compensated by the advantage of the other.

A variety of hybrid techniques have been proposed in the literature, each has its particularity, its own advantage and disadvantage and for which application was designed.

For this reason, this paper deal with the review of hybrid global MPPT techniques (HGMPPT) proposed in the literature and at the same time proposes a classification based essentially on the type of algorithms applied in the employed technique.

Manuscript received August 29, 2022; revised December 19, 2022.

F. Belhachat, and C. Larbes are with Ecole Nationale Polytechnique (e-mails: faiza.belhachat@g.enp.edu.dz, cherif.larbes@g.enp.edu.dz).

Digital Object Identifier (DOI): 10.53907/enpesj.v2i2.116

The reviewed HGMPPT is classified into four main categories: hybrid methods combining conventional algorithms, hybrid methods combining soft computing algorithms, hybrid methods combining conventional and soft computing techniques and other HGMPPT techniques.

Subsequently, all the reviewed methods will be discussed and their performances will be also evaluated in terms of different criteria's. The analysis of the different hybrid methods has made it possible to draw several observations concerning the use of the applied techniques.

This review helps the researchers to acquire comprehensive and precise information about the application of the different hybrid algorithms and furthermore help them to choose an efficient way to harvest maximum power from the PV systems during partial shading conditions (PSC) by applying the appropriate and suitable HGMPPT algorithms.

This paper is arranged as follows: Section 2 explains partial shading effect on photovoltaic module characteristic, while section 3 introduces partial shading mitigation methods for PV systems. Section 4 describes and classifies the selected hybrid techniques, the analysis and discussion are described in section 5 and the conclusion is provided in the section 6.

II. PARTIAL SHADING EFFECT ON PV MODULE CHARACTERISTIC

A PV module is usually connected in series to form a string. When the PV module is subjected to the shading effect, the exposed part of the solar cell to shading will no longer generate power and the module become as a load.

The shaded module current will force the output current of the whole string. In extreme cases, the shaded modules will generate excess heat due to reverse current flow. The excessive heat generated in certain part of PV modules leads to creation of the hot spots. In order to overcome this problem, bypass diodes are connected in parallel with group of PV cells. The bypass diode will bypass the cell current subjected to shading and protect the module failure due to hot spots [3-4].

Fig.1 shows P-V characteristics of two PV modules connected in series under STC and PSC.

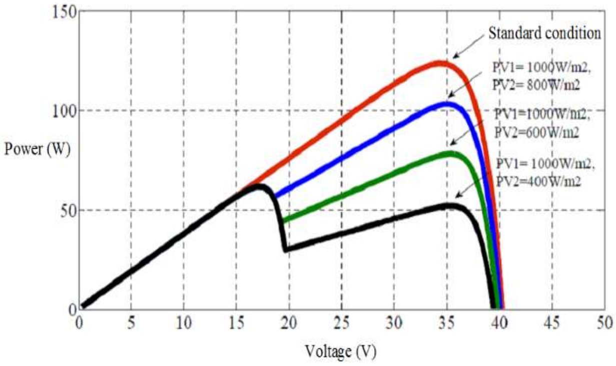

Fig.1: P-V characteristics curves obtained under STC and PSC.

III. PARTIAL SHADING MITIGATION METHODS FOR PV SYSTMES

Partial shading causes considerable power losses which affects the performance of the overall system, which has led researchers to develop numerous solutions which make it possible to remedy this problem and consequently reduces losses due to the shading. Several solutions are available to reduce this negative effect and therefore maximize the power supplied. Among the available solutions, we mention the bypass diode employment, the PV systems architecture, the PV array configuration and reconfiguration and MPPT techniques. A brief classification of shading mitigation techniques is presented in this section.

III.1. By-pass diode employment

Bypass diodes are electronic components that prevent problems associated with shading. They are associated with groups of PV cells within a single panel and allow current to flow by isolating the shaded cell in order to avoid drops in production (Fig.2). The insertion of the bypass diode with groups of cells causes the appearance of several peaks on the PV characteristics.

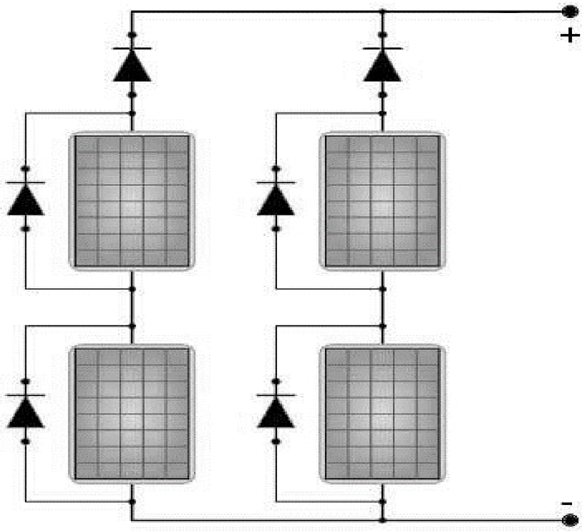

Fig.2: 2x2 PV array with bypass diodes across each PV module and blocking diodes.

III.2. PV System architecture topologies

The PV system architecture topologies describe how the power electronics converters are linked to the configuration of the photovoltaic panel. The most commonly used architectures are central inverters, string inverter, multi-string inverter and micro inverter system.

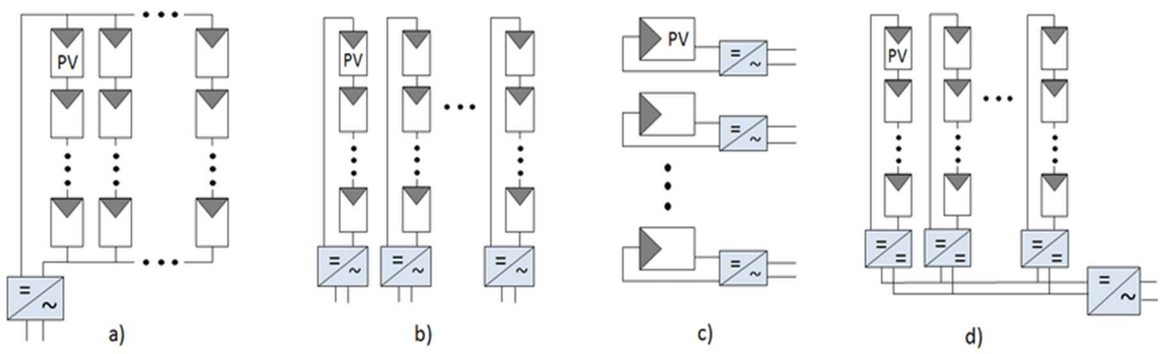

Fig.3: PV system topologies: (a) Central inverters; (b) String inverters; (c) Module inverters; (d) Multi-string inverters

III.3. PV array interconnection topologies

PV array configuration describes the way of the interconnection of the PV modules inside the PV array. There are the conventional configurations which are the Series (S), Parallel (P) and Series-Parallel (SP) configurations and the alternative configurations which are the Total-Cross-Tied (TCT), BL Bridge-Linked (BL) and Honey-Comb (HC) configurations. Several works have been studied and analyzed the performance of different PV configurations under PS conditions. The TCT configuration has been shown to provide the best performances compared to other PV configurations [3].

III.4. PV array reconfigurations

PV array reconfiguration process is considered as one of the most efficient solution to minimize the negative effect of PS to improve the extracted power. It aims to equalize the generated currents in different electrical rows.

Reconfiguration techniques are divided into two classes: static and dynamic reconfigurations. Several static and dynamic reconfiguration techniques and control algorithms to alleviate the negative effect of PS have been developed in the literature [5].

Fig 5 and 6 show examples of some static and dynamic reconfigurations techniques proposed in the literature.

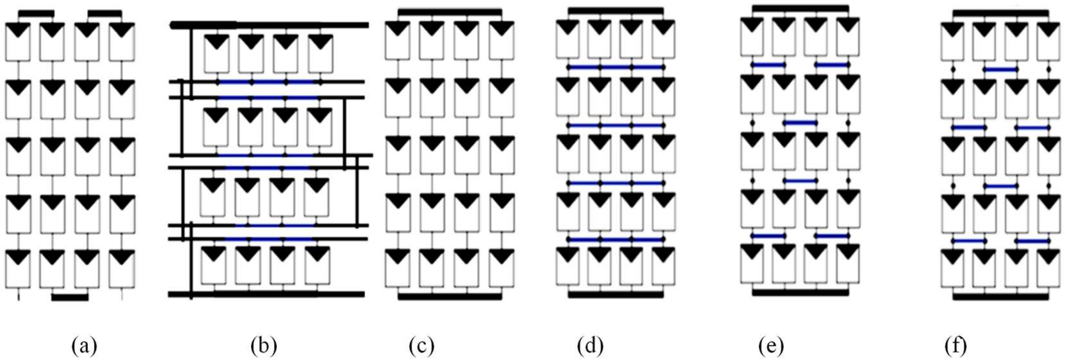
(a) (b) (c) (d) (e) (f)

Fig.4: PV array configurations scheme: (a) Series (S), (b) Parallel (P), (c) Series-Parallel (SP), (d)Total-Cross-Tied (TCT), (e) Honey-Comb (HC), (f) BL Bridge-Linked (BL).

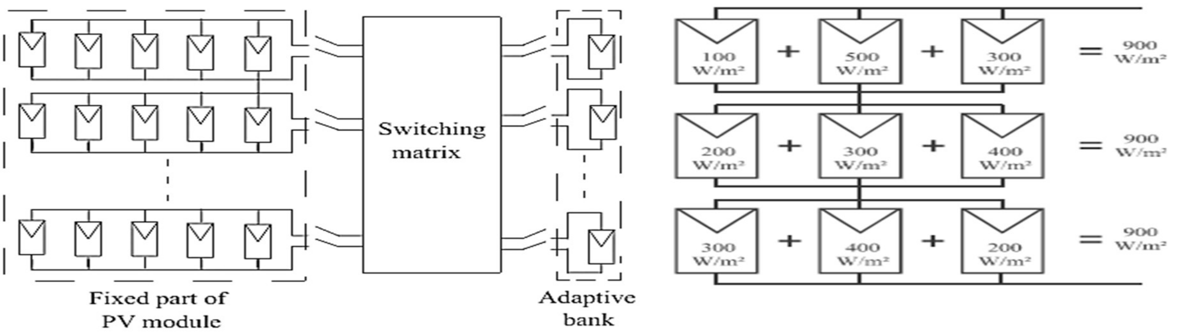

(a) (b)

Fig. 5: Dynamic reconfigurations techniques examples: (a) Adaptive bank method, (b) Irradiance equalization principle for 3x3 TCT PV array.

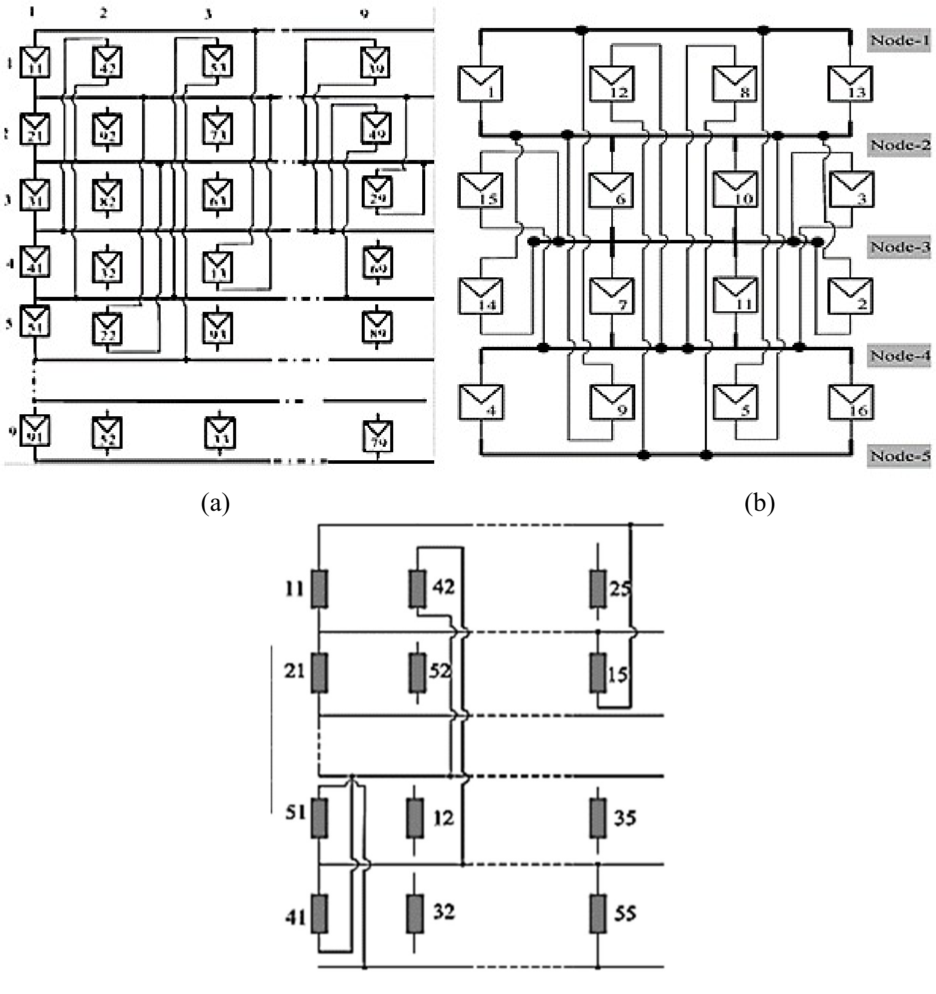

(a) (b)

(c)

Fig.6: Examples of some static configurations proposed in the literature. (a) Su Do Ku arrangement, (b) Futoshiki arrangement, (c) Magic square arrangement.

*III.5. Maximum power point tracking (*MPPT) *techniques*

MPPT is a technique commonly used with PV systems to maximize power extraction under all climatic conditions. Fig.7 depicts a model of photovoltaic system integrated with MPPT [6]. .

In the literature, numerous paper proposed control algorithms performing a maximum power point search under partial shading conditions (PSC).

In this paper, we are only interested in hybrid global MPPT techniques (HGMPPT).

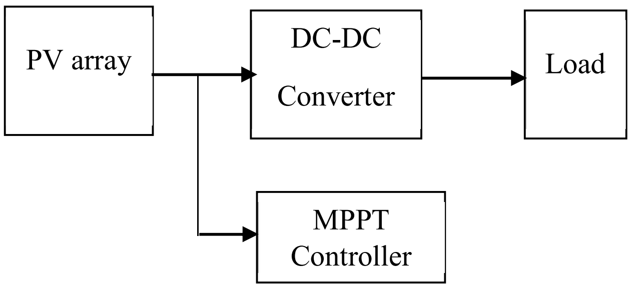

Fig.7: A model of photovoltaic system integrated with MPPT.

The most important strengths and weakness of each strategy can be summarized as follows: The use of the bypass diodes across one or series of PV modules avoids hot spots effect. However, its employment under PS conditions creates multiple local maximum power points. The appearance of these multiple peaks on the characteristics of PV array makes the tracking more difficult under these conditions and requires the integration of a more efficient power control system which is able to distinguish between local and global maxima to harvest the maximum possible energy and therefore, increase the efficiency of the entire system.

Additionally, the shading effect can be further mitigated by using alternative PV arrays' configurations such as TCT, BL and HC. The TCT configuration presents the best performances under most cases of PSC. However, TCT configuration does not provide the maximum possible power under PS and the extracted output power can be further improved. PV array reconfiguration strategy has been adopted as an alternative solution to optimize the power output under PS conditions. Many reconfiguration static techniques suffer from ineffective shade dispersion which reduces their reliability while. While, the dynamic technique requires a monitoring reconfiguration algorithm to identify the optimum configuration and the switching matrix to make connections between PV modules.

A variety of photovoltaic power system topologies and their control schemes exist and the way in which are arranged varies in term of complexity, efficiency and cost.

IV. HYBRID GLOBAL MPPT (HGMPPT) METHODS CLASSIFICATION

In this study, the reviewed HGMPPT techniques are divided into four main categories according to the type of the used algorithms in tracking as shown in Fig.8. The four groups are hybrid methods combining classical algorithms, hybrid methods combining soft computing algorithms, hybrid of classical and soft computing methods and other HGMPPT techniques.

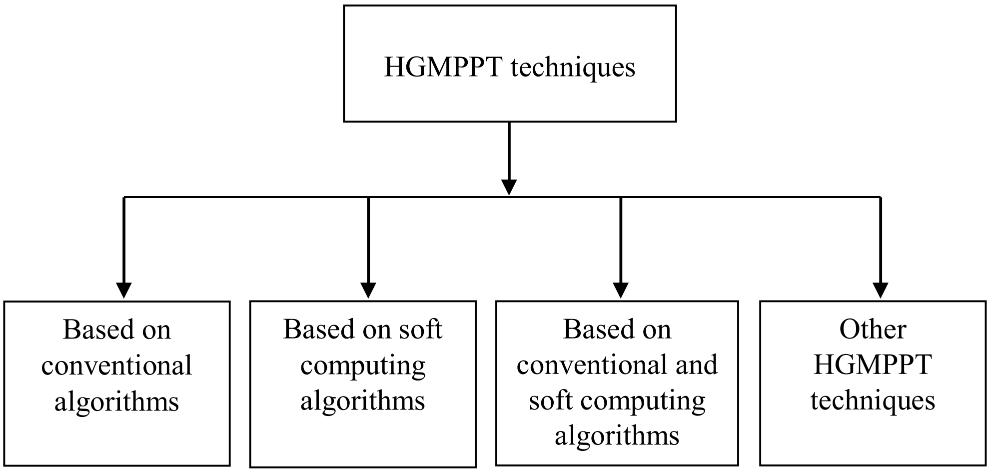

Fig.8: Proposed classification of the HGMPPT techniques.

IV.1. HGMPPT combining conventional algorithms (conventional-conventional algorithms based methods)

This category comprises the list of HGMPPT methods that integrates two or more classical algorithms. The conventional algorithm can be: perturb & observe (P&O), incremental conductance (INC), fractional open circuit voltage (FOCV), fractional short circuit current (FSCC), or power increment technique (PIT).

IV.1.1. Fractional open circuit voltage with perturb and observe (FOCV-P&O)

The FOCV approach is simple and effective, nevertheless it accuracy is low. Whereas P&O algorithm, is more accurate, but induces oscillations around MPP. Therefore, a fractional open circuit voltage is integrated with P&O algorithm to improve the performance in [7].

The weakness of an individual MPPT algorithm is overcome by the advantage of another with which it is combined. In this technique, the FOCV method situates general position a global maximum while the P&O method exactly locate it.

The proposed hybrid method *FOCV-P&O* is experimentally validated by implementing two PV panels connected in series using buck converter and compared the single P&O and FOCV.

IV.1.2. Power increment technique with perturb & observe (PIT-P&O)

For the same purpose, the same authors in [7] proposed hybrid method which combines the power increment and P&O techniques. Similarly, the proposed hybrid method PIT-P&O is experimentally validated by implementing two PV panels connected in series using buck converter and compared the single P&O and PIT technique [7].

*IV.1.3. Fractional open circuit voltage with i*ncremental conductance *(FOCV- INC)*

This hybrid technique combine the FOCV and INC algorithms. This algorithm works in two steps. First, FOCV technique finds global maximum region. Whereas, the variable step sized incremental inductance reaches global maximum power point. According the authors, this efficient technique has quick response time and easy to be implemented [8].

IV.1.4. Improved 0.8 V_{OC} model with smart power scanning procedure (I0.8 V_{OC} model –SPSP).

In this study, [9] used an improved 0.8 V_{oc} model and P&O algorithm for module level MPPT applications. The improved 0.8 V_{oc} model employs a power scanning procedure, which is based on the sign of PV module power change.

Figs.9 and 10 depict the flowchart and block diagram of the I0.8 V_{OC} model –SPSP technique.

The proposed HGMPPT was experimentally validated. The results obtained show higher tracking efficiency of the proposed technique compared to other techniques. This hybrid algorithm is used for module-integrated converters (MICs), PV power optimizers and module level distributed MPPT applications.

IV.1.5. Open circuit voltage and short circuit current based method (OCV-SCC)

In [10], a combination of the OCV and SCC techniques has been realized. The modified SCC is employed under normal conditions whereas the modified OCV method is used during PSC. The flowchart of proposed OCV-SCC technique is depicted in Fig.11.

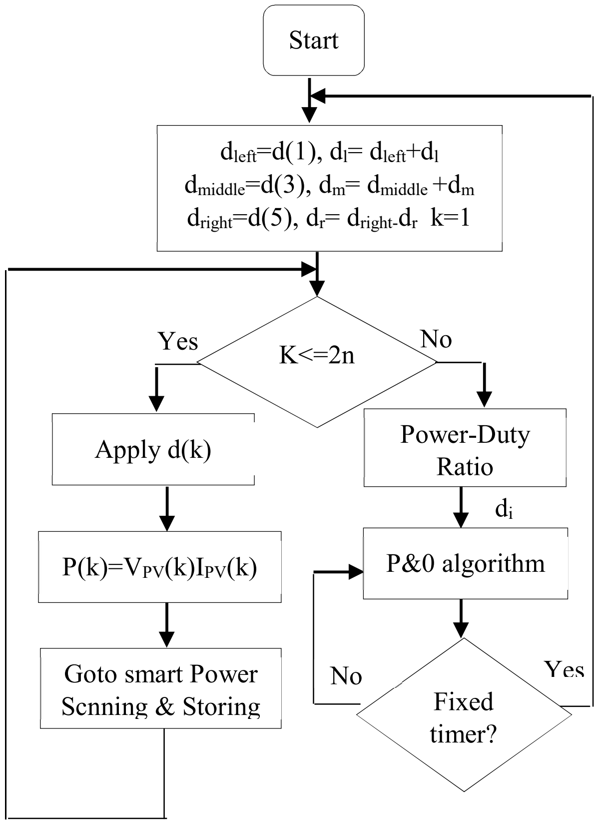

(a)

Smart Power Scanning & Storing

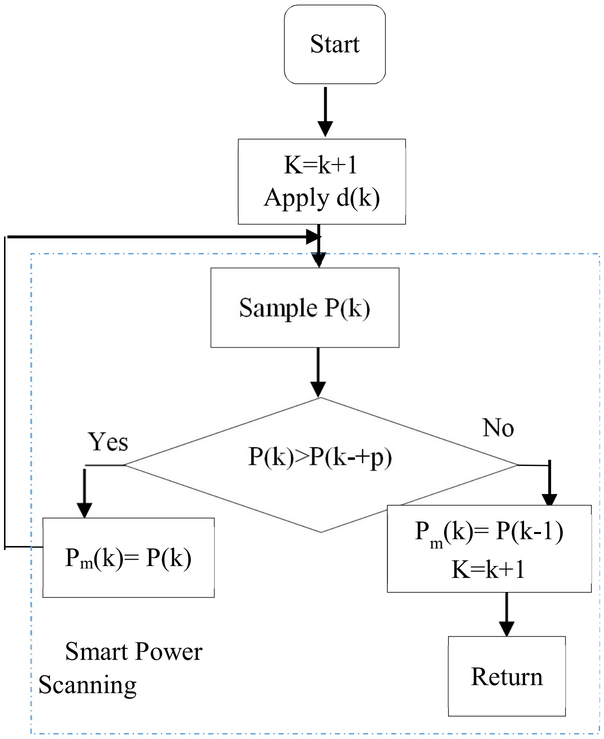

(b)

Fig.9: (a) The flowchart of the I0.8 VOC model –SPSP.(b) Smart Power Scanning & Storing procedure [9].

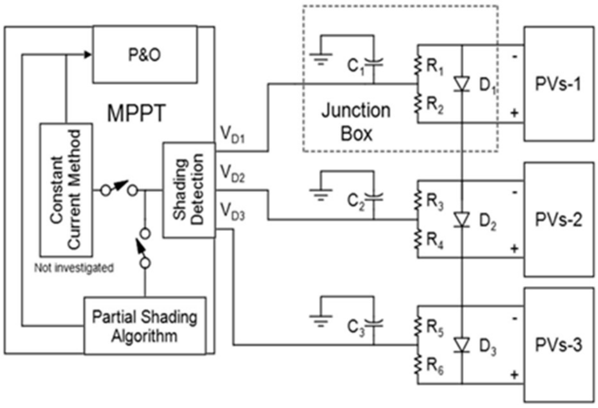

Fig.10: Block diagram of the I0.8 VOC model –SPSP [9].

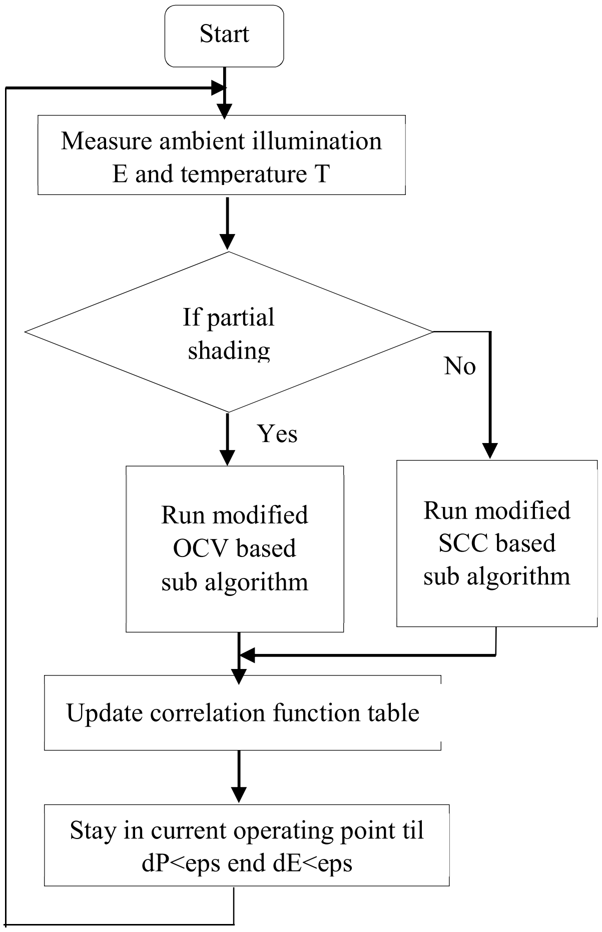

Fig.11: The flowchart of the OCV-SCC method [10].

IV.2. HGMPPT combining soft computing algorithms (soft computing - soft computing algorithms based methods)

This group contains all the methods which combine two or more algorithms belong to the soft computing algorithms such as PSO, DE, WOA, JAYA, SA, GWO, FFA, FWO and Beta algorithms, etc. …

IV.2.1. Differential evolutionary and particle swarm optimization algorithms (DEA-PSO)

The DEA and PSO algorithms are combined to track the GMPP under PS conditions in [11].

Simulation and experimental validation are investigated to verify the performance of the proposed technique under different PSC. According the authors, this method offers several advantages including reliability, system independence, and accuracy in GMPP tracking under PSC.

IV.2.2. Whale optimization and differential evolution algorithms (WOA-DEA)

The *WOA* algorithm was integrated with DEA technique to track global MPP. The WOA-DEA technique track the GMPP in short time and less number of searching agents [12]. The WOA allows to searches the global best in an efficient way while the DEA improves the performance of the WOA.

IV.2.3. Jaya and differential evolution algorithms (JAYA-DEA)

The hybrid method JAYA-DEA was introduced in [13] by hybridizing the Jaya with differential evolution to cut down the excessive number of iteration and searching delay.

The combined performance of Jaya and DE algorithms enhances the searching ability and reduces the number of iteration with the minimum computational burden [13].

The algorithm generates duty cycle from three values, the best and worst in these three values is chosen in accordance with the performance. After that, Jaya updates all values by using (1) and transmit all updated data the DE algorithm after evaluating best and worst.

$$\mathrm{D}_{i,j}^{k+1} = \mathrm{D}_{i,j}^{k} + \mathrm{rand}_1 \mathrm{x}(\mathrm{D}_{i,best}^{k} - |\mathrm{D}_{i,j}^{k}|) - \mathrm{rand}_2 \mathrm{x}(\mathrm{D}_{i,worst}^{K} - |\mathrm{D}_{i,j}^{k}|) \qquad (1)$$

Where, $D_{i,j}^{k}$ is the value of the *i*th variable for the *j*th candidate during the t*th* iteration, $D_{i,best}^{k}$ is the value of variable '*i*' for the best candidate during the *k*th iteration, $D_{i,worst}^{K}$ is the value of variable.

DE algorithm, by means of searching process (mutation, crossover and selection process) generates the best place for all candidates of the Jaya algorithm.

Afterwards, all duty cycles are mutated by using wavelet mutation, which notice the variations and consequently modify the obtained duty cycles. The wavelet mutation process is described as,

$$\mathrm{D}_i^{k+1} = \begin{cases} \mathrm{D}_i^k + \xi \mathrm{x}(\mathrm{D}_{max} - \mathrm{D}_i^k), & \text{if } \xi > 0 \\ \mathrm{D}_i^k + \xi \mathrm{x}(\mathrm{D}_i^k - \mathrm{D}_{min}), & \text{if } \xi \leq 0 \end{cases} \qquad (2)$$

Where, D_{min} and D_{max} are the minimum and maximum value of the duty cycle. ξ is wavelet mutation operator.

According the authors, the proposed method is accurate in tracking GMPP and faster in comparison to others published methods. In addition, it has a good dynamic and steady state responses under different conditions.

IV.2.4. Simulated annealing and particle swarm optimization algorithms (SAA-PSO)

In another study, a SAA algorithm and PSO algorithm are combined to reach much faster and more accurate tracking to the global MPP [14]. The SAA-PSO algorithm quarries the core part of the PSO algorithm with the stepwise change pattern, which is integrated into the SAA method. The algorithm can reduce the tracking time and increase the tracking accuracy. The proposed SAA-PSO exhibits better performances under PSC compared to the SA and PSO algorithms.

IV.2.5. Modified genetic and firefly algorithms (MGA-FFA)

The GA has complicated calculations and poor accuracy under PSC. [15] combined a modified GA with FFA and added a differential evolution (DEA) algorithm to further improve the calculation process. GA calculations are simplified by the integration of the DEA mutation process and FFA attractive process. The flowchart of the proposed MGA-FFA algorithm is illustrated in Fig.12.

Both the simulation and experimental evaluation show that the MGA-FFA algorithm presents a fast response time and high accuracy under PS.

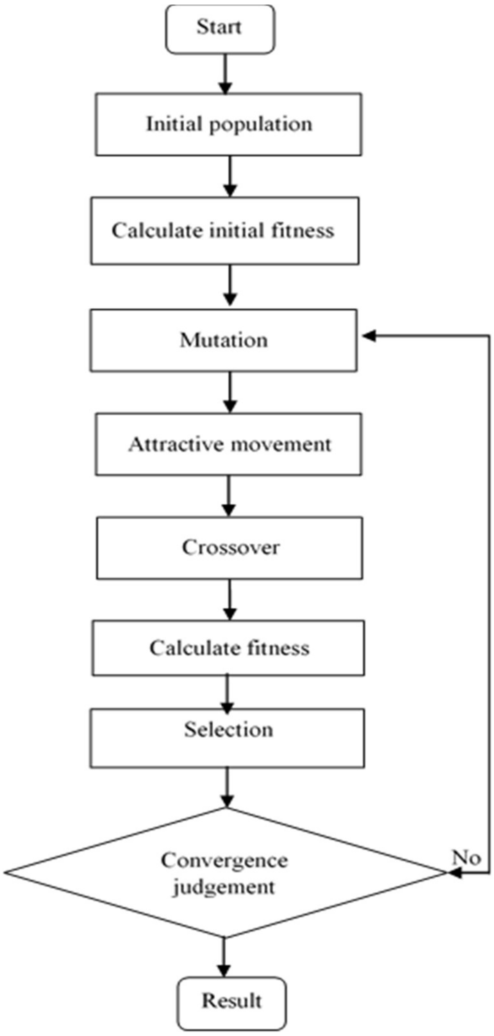

Fig.12: The flowchart of proposed *MGA-FFA* algorithm [15].

IV.2.6. Grey Wolf Optimization and Golden-Section Optimization algorithms (GWO-GSO)

The GWO has been used to track GMPP. Wherever, it requires numerous iterations resulting in significant power losses.

A hybrid search algorithm (GWO-GSO) integrating GWO and GSO to extract GMPP for photovoltaic systems was applied in [16]. Initially, MGWO is activated for the global search. In conventional GWO, wolf leaders possess the same impact on decision-making. In this technique, the decision weights of wolf leaders are automatically tuned with hunting progression to accelerate hunting. After that, the algorithm is switched to GSO for the local search, which play a crucial role to avoid useless search and reduce the tracking time. Additionally, a novel restart judgment based on the quasi-slope of the power-voltage curve is introduced to improve the reliability of MPPT systems. Simulation and experiment results reveal that the proposed GWO-GSO technique track the GMPP quickly and accurately with higher accuracy under different PSC.

According the authors, the proposed GWO-GSO exhibits better performance compared to the P&O, PSO, GWO and GWO-P&O algorithms under different conditions in terms of tracking time and output power,

IV.2.7. Grey wolf optimization and Beta algorithms (GWO-β)

[17] proposed a HGMPPT which combines the GWO algorithm with β method to enhance the convergence speed and reduce the power oscillations around MPP. The proposed algorithm employs the GWO technique to reach the GMPP, whereas, at the same time, the β method calculates the MPPT reference based on the PV voltage and current at GMPP. Then, only the Beta method which is activated to track the MPP reference, ensuring the GMPP in that specific operating point. The effectiveness of the proposed GWO-β algorithm was evaluated by means of simulation results, in which the proposed technique was compared to the P&O, β and GWO methods.

According to the authors, the simulation results show that the proposed MPPT algorithm converge quickly to the GMPP. Moreover, in, low power oscillations occur at MPPT in steady state as well as higher tracking efficiency compared to the other MPPT methods.

IV.2.8. Overall distribution and Particle Swarm Optimization algorithms (OD- PSO)

The authors in [18] proposed a OD algorithm to rapidly found the area near the global maximum power points, which is further mixed with the PSO algorithm to improve the MPPT accuracy

In this algorithm, the OD algorithm is first used to rapidly obtain the particles, which are within a small region that contains the GMPP. The obtained particles will be used as the initial particles for PSO algorithm, and finally the PSO algorithm captures the GMPP. The effectiveness and accuracy of the OD-PSO algorithm are demonstrated through simulations and experimentations.

IV.2.9. Particle swarm optimization and gravitational search algorithm (PSO-GSA)

Hybrid of PSO and GSA techniques have been proposed to track GMPP in [19].

The PSO-GSA algorithm combines the capability of social evolution of PSO and the local search ability of GSA. Results obtained from proved efficiency of PSO-GSA technique compared to other techniques.

IV.2.10. Particle swarm optimization (PSO) and ANFIS (PSO-ANFIS)

[20] proposed hybrid technique combining an adaptive neuro-fuzzy inference system (ANFIS) and PSO technique. The PSO-ANFIS method efficiently tracks the global maximum with a fast time. Simulation results prove that the PSO-ANFIS is more efficient and has higher speed tracking compared to the PSO and FFA algorithms.

IV.2.11. Grey wolf optimization algorithm and fuzzy logic controller (GWO-FLC)

[21] combined the GWO witch fuzzy logic controller (FLC) to solve the problem of oscillations around the global MPP. The hybrid of GWO and FLC exploits the advantages of both techniques where GWO is fast and reliable in tracking GMPP under PSC and FLC presents low oscillations around the GMPP. In addition, two initialization techniques are proposed to re-initialize the GWO to achieve the dynamic or variant GMPP. The initialization techniques are based on predefined time or PSC changes. Simulation results demonstrates that the proposed technique has superior performance in case of time variant PSCs.

IV.2.12. A general regression neural network trained with sailfish optimizer (GRNN-SFO)

[22] proposed a highly effective HGMPPT technique which consists of a general regression neural network trained with meta-heuristic sailfish optimization algorithm (GRNN-SFO). To verify the performance of the proposed technique, a comparison was made with the GRNN-PSO and GRNN-P&O methods. The comparison shows that GRNN-SFO tracks the global maxima with great efficiency and faster tracking time under fast varying irradiance and partial shading condition compared to the two methods.

IV.3. HGMPPT combining conventional and soft computing algorithms (conventional - soft computing algorithms based methods).

In this group, the classical algorithms such P&O, INC, FOC are combined with soft computing methods such ANN, FLC, PSO, SA, and ACO…

IV.3.1. Artificial neural network and P&O algorithms (ANN-P&O)

Several works have adopted this technique, combining the artificial neural network and the P&O [23-25].

In [23] and [24], the ANN predicts the region of the global MPP and then a P&O method searches real global MPP within the local region. The general process of the proposed ANN-P&O technique is depicetd in Fig.13. According to the author, this method has simple structure and provide a fast convergence speed.

In another study, this method combines P&O with the ANN technique. The ANN predicts the global MPP region by estimating its voltage boundaries. The P&O algorithm identifies the MPP in the estimated region [25].

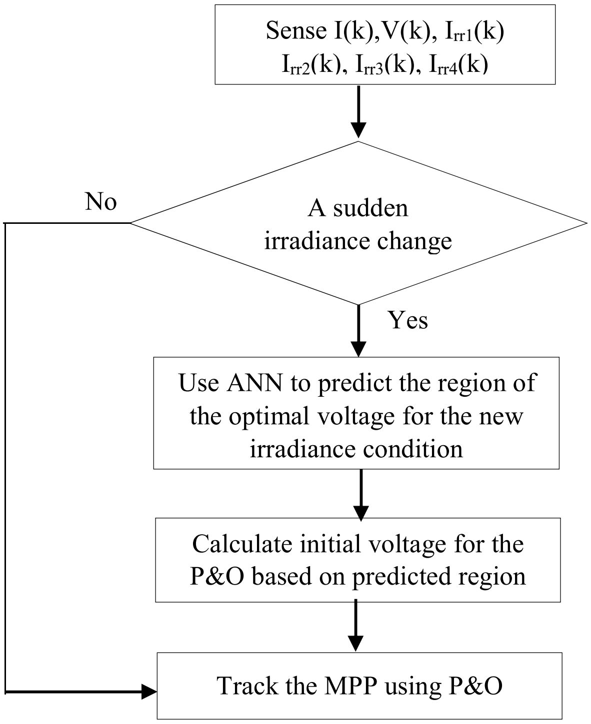

Fig.13: The general process of hybrid ANN-P&O MPPT [23].

IV.3.2. Artificial neural network and a hill climbing method (ANN-HCA)

In the study carried out in [26], an artificial neural network and a hill climbing method is combined to achieve global MPP. Initially, the hybrid method uses the ANN to provide a first GMPP estimation. Then, a HCA find the estimated optimal one. In this approach, the computational burden is reduced due to a good ANN structure and its training process.

IV.3.3. Fuzzy logic control and Perturb and observe and (FLC-P&O)

This hybrid algorithm combines P&O and fuzzy logic control (FLC) algorithms. The proposed algorithm starts MPPT with P&O and switches to FLC algorithm when the transient operating point is close to the global MPP [27]. According to the authors, this algorithm reach quickly the global MPP with less oscillation.

Simulation results show that the proposed method exhibits more harvested energy compared to single P&O and FLC algorithms. The flow chart of the proposed hybrid *FLC-P&O* MPPT method is shown in Fig.14.

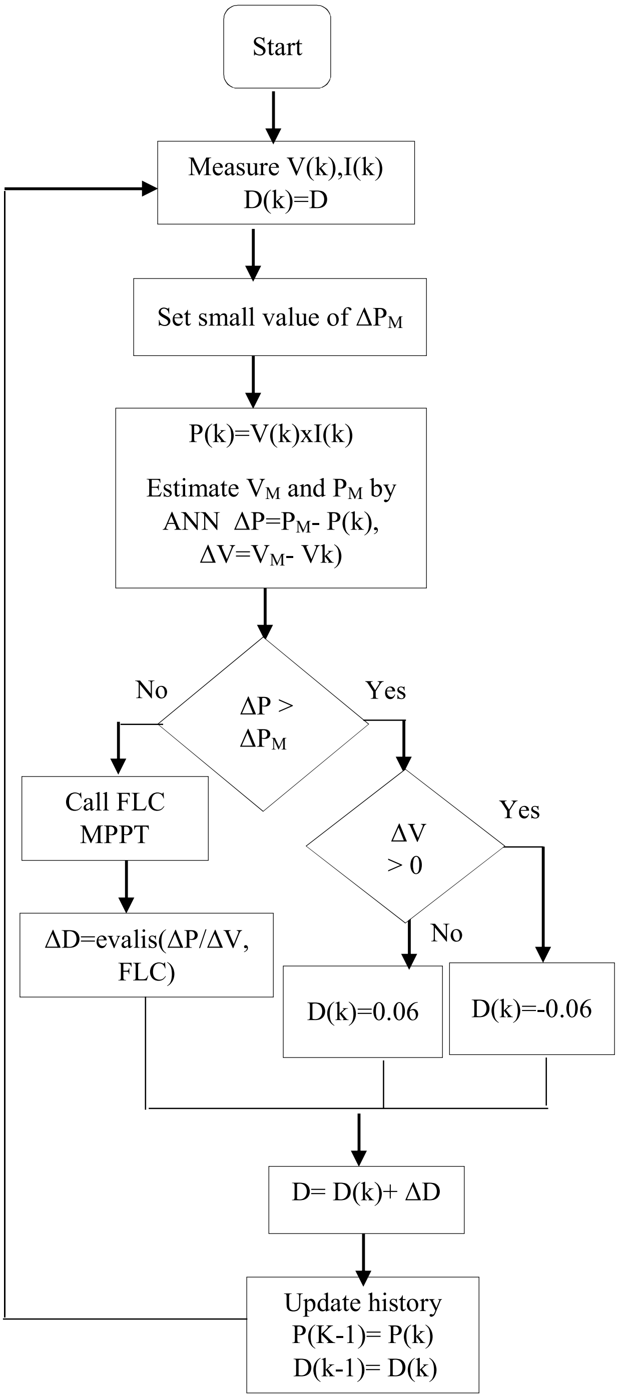

Fig.14: The flowchart of the proposed hybrid FLC-P&O MPPT method [27].

IV.3.4. Particle swarm optimization and incremental conductance (PSO-INC)

The PSO has been widely applied in MPPT tracking in PSC however; this algorithm suffers sometimes from a slow convergence speed and large search space. Several works listed in the literature combined the PSO algorithm with other algorithms such as P&O, INC and HC algorithms. A hybrid technique combining PSO and INC is proposed in [28]. In this method, first, the INC algorithm find the closest local maximum; then, the PSO method searches the global maximum point.

The time required for convergence is reduced due to the reduced searching area of the PSO algorithm. Simulation results demonstrate that the proposed hybrid PSO-INC method track the GMPP easily with a faster response time and better dynamic response compared the PSO algorithm. The authors in [29] proposed a dormant particle swarm optimization (DPSO) algorithm. The DPSO algorithm integrated with INC algorithm is simple for implementation and attain GMPP quickly and accurately under partial shading conditions.

IV.3.5. P&O and PSO (PSO-P&O)

Recently, the hybrid technique which integrates the conventional and metaheuristic approaches, is gaining interest [30-34]. A P&O method find the first local maximum point whereas the PSO MPPT methods success to track the global maximum point. However, the PSO algorithm has a long time convergence when the range search space is large. [30] proposed a hybrid method, which combines P&O and PSO methods. First, the P&O gives the nearest local maximum. Then, the PSO searches the global MPP. The main advantage this method is the reduction of PSO search space, which improves the time required for convergence. Simulation and experimental results show that the proposed hybrid PSO-P&O method tracks the GMP successfully with a faster convergence time and better dynamic response compared the PSO method.

Also, in [34] the P&O and the PSO algorithm was combined. Additionally, in order to enhance the tracking GMPP performance under complex shading conditions, an improved hybrid technique which combines a modified P&O and enhanced PSO was proposed in [32].

[35] presented a hybrid enhanced leader particle swarm optimization (ELPSO) assisted by a conventional perturb and observe (P&O) algorithm. The experimental results proved the superiority of the ELPSO-P&O method in tracking the maximum power under all shaded conditions.

IV.3.6. Hill climbing and particle swarm optimization algorithms (PSO-HCA)

The HCA is combined with the PSO. In this method, the MPPT algorithm uses the HCA method to update the position of the best particle and the PSO algorithm is employed to place the rest of particles [36].The effectiveness of the proposed method has been confirmed in simulation studies under partial shading conditions. The computational complexity of the proposed algorithm is low and allowing to its implementation using low cost microcontrollers.

IV.3.7. Particle Swarm Optimization and proportional-Integral (PSO-PI)

This algorithm combines the advantages PSO and proportional integral (PI) control technique [37]. The hybrid method uses firstly the PSO algorithm to find the global peak. Then, the PI controller is activated to increase the tracking precision and to track slow variations in the global peak location. An adaptive sampling time strategy is adopted to accelerate the convergence to the GP. Simulation is carried out using Matlab/Simulink to prove the performance of the PSO-PI algorithm under different partial shading conditions. The results obtained shows fast tracking speed and high accuracy. According to the authors, this algorithm is simple.

IV.3.8. Simulated Annealing and P&O algorithms (SAA-P&O)

SAA has been applied efficiently to track a global maximum with limited implementation complexity. As it was mentioned previously, P&O is simple and easy to be implemented but fails to locate global maxima, and the SA method is unable to carry out continuous searching [38]. The algorithm uses first the SAA algorithm to locate the neighbourhood of the global maxima. Then, the P&O method is applied to perform well tracking to the GMPP.

By merging the two techniques, some of their limitations are overcome such as the failure of the SA algorithm to continuously track and the limited ability of the P&O algorithm to identify global maxima. The effectiveness of the proposed hybrid SAA-P&O technique was demonstrated by simulation results.

IV.3.9. Grey wolf optimization and Perturb & Observe (GWO-P&O)

In this method, the GWO and P&O algorithms are mixed to achieve faster convergence to the GMPP [39]. GWO operates in the initial stages of MPP tracking and the P&O is employed at the final stage to attain faster convergence to the GMPP.

The effectiveness of the proposed hybrid GWO-P&O algorithm has been evaluated through both simulation studies and by experimental studies. The comparative study between the GWO-P&O technique, GWO and PSO-P&O demonstrates that the proposed GWO-P&O exhibits superior performance such as higher tracking speed and faster convergence.

IV.3.10. Whale optimization and Perturb and Observe algorithms (WOA-P&O)

The WOA technique shows more power oscillations when the algorithm tracks the MPP around the GP. To attain the maximum power with less power oscillation and a fast convergence speed, the WOA is combined with the P&O [40]. Thus, this hybrid algorithm overcomes the computational burden encountered in a WOA. In the WOA-P&O technique, the WOA predict the initial global peak and P&O to achieve a quicker convergence to a GP in the final stage. Simulation and hardware results showed that the proposed hybrid WOA-PO technique is efficient in GMPP tracking under various PSC and changes in irradiance level for both the dynamic and steady state conditions.

IV.3.11. An improved P&O and artificial bee colony algorithms (ABC-IMP&O)

In [41], a modified P&O is integrated with ABC algorithm. In the proposed method, GMPP is firstly identified by ABC algorithm and then the P&O algorithm is used for local MPP. The proposed method combines the advantages of both ABC and P&O algorithm.

Therefore, the local search ability of P&O and global search ability of ABC are reliably combined to provide effectively optimum duty cycle to the boost converter. The proposed ABC-P&O algorithm is implemented using Matlab/Simulink model and it is compared to P&O, INC and ABC algorithms. The simulation results demonstrate that the proposed ABC-PO algorithm is more efficient under PSC. Fig.15 depicts the flowchart of the proposed algorithm.

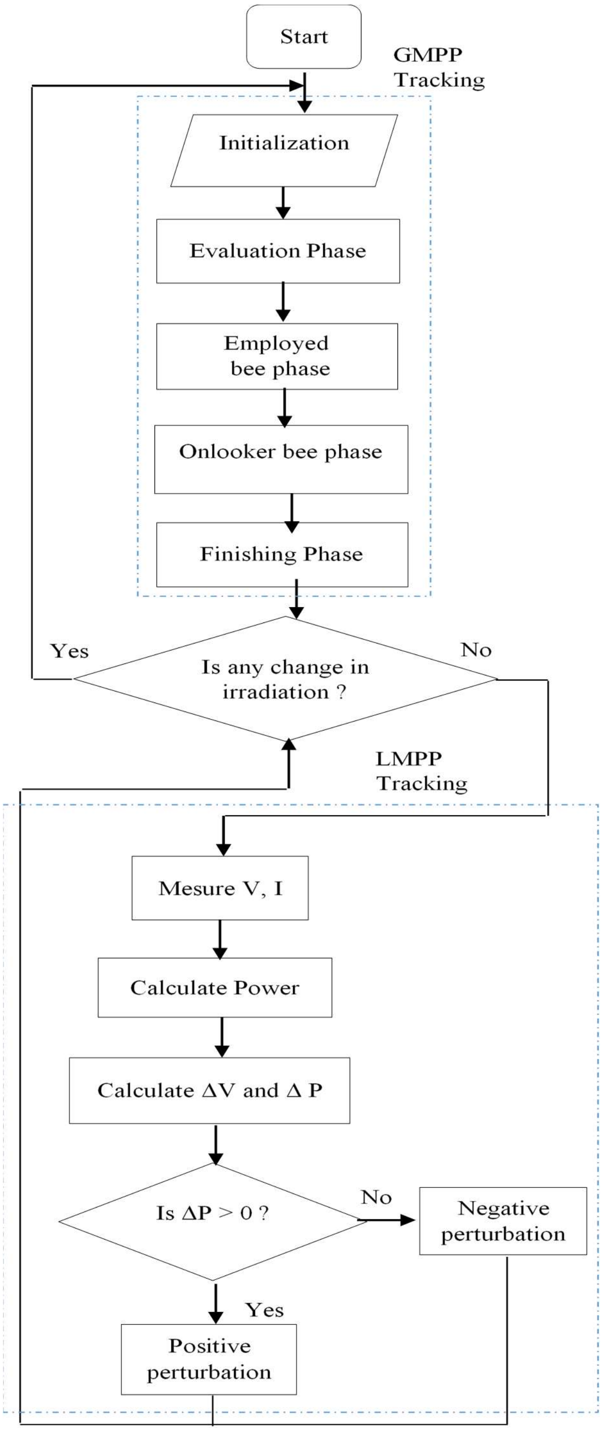

Fig.15: the flowchart of ABC-P&O algorithm [41].

IV.3.12. Ant colony with perturb and observe algorithms (ACO-P&O)

A hybrid MPPT algorithm which combines the ACO and P&O method was introduced in [42]. In this technique, the ACO method tracks a maximum power from PV array under all variations while the P&O achieve faster MPP tracking in final stage. In fact, when the ant colony approaches the MPP, the P&O MPPT begins at the location of the best ACO process.

The proposed ACO-P&O algorithm is validated by both simulation and hardware implementation. This hybrid technique has superior performance and fast tracking speed to track GMPP than other methods such as GWO, ACO and P&O methods.

IV.3.13. Firefly algorithm and incremental conductance (FFA-INC)

The INC and FFA are combined to provide a faster global searching capability and tracking speed [43]. INC algorithm was used for its low-cost implementation and stability under rapidly changing conditions, whereas, FA is very efficient in searching the GMPP.

Initially, the proposed algorithm used INC to find the first local MPP quickly. Next, the initial position and population size of fireflies is determined by the population initialization mechanism. After the initialization, FA searches the global optimal region. Finally, the GMPP is found by the improved INC within global optimal region.

The FFA-INC algorithm is compared to the P&O, FFA and INC MPPT methods under four different conditions. Simulation and experiment results show that the proposed algorithm tracks the GMPP under various conditions with higher speed and accuracy.

IV.3.14. Fireworks algorithm and Perturb and Observe (FWA-P&O)

This strategy exploits the advantages of the P&O and FWA algorithms [44]. Under uniform irradiance conditions, the P&O algorithm is used due to its dynamic tracking capability, where it tracks the unique MPP. During the occurrence of partial shading, the FWA determine the global MPP, due to the good exploration and exploitation characteristics and fast convergence that possess. The FWA-P&O technique is implemented using a low-cost microcontroller and performances are verified through experimentation.

The performance of the proposed technique is compared to the conventional PSO algorithm and has been demonstrated the superiority of the FWA-P&O method terms of dynamic tracking capability and power oscillation during tracking.

Fig.16 shows the flowchart for the proposed GMPPT FWA-P&O algorithm.

IV.3.15. Modified bat and Perturb & Observe algorithms (MBAT-P&O)

In [45], a hybrid search algorithm that consist of modified bat algorithm and P&O algorithm was proposed. The standard bat algorithm has been modified in this hybrid method by adding tabu list avoiding a duplication of unsuccessful solutions, first, a modified bat algorithm determine the global peak area, and then P&O track the MPP in the global peak area.

The simulations results demonstrated that the proposed MBAT-P&O method has superior performances compared to the standard bat and P&O algorithms.

IV.3.16. Gravitational search and P&O algorithms (GSA-P&O)

[46] proposed hybrid GMPPT algorithm combines the GSA with P&O algorithm. Initially, the GSA the scannes a power-voltage (P-V) curve to obtain the best solution which is then transferred to P&O algorithm.

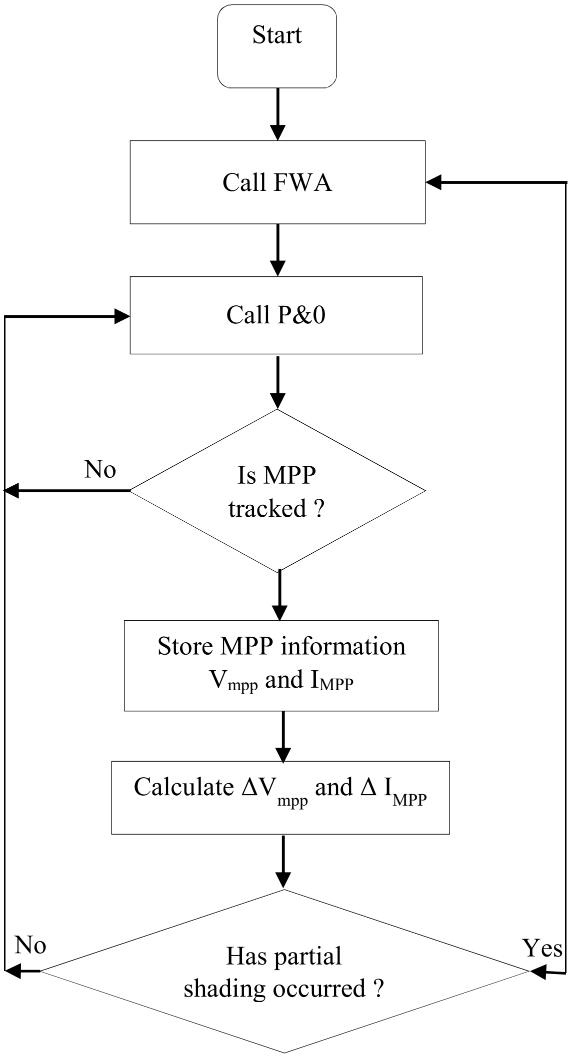

Fig.16: the flowchart of the proposed FWA-P&O [44].

Simulation and experimental results demonstrated that the GSA-P&O performance has been enhanced and it exhibits high efficiency in comparison with GSA and P&O.

IV.3.17. Hill climbing with single current sensor and artificial bee colony algorithms (HC-SS-ABC)

In order to reduce the number of sensors and obtain a good convergence speed, [47] has proposed a hybrid algorithm integrating the single sensor hill climbing (HC-SS) and ABC algorithms. In this technique, the detection of the occurrence of partial shading conditions as well as identification of type of shading pattern are performed by scanning the output current vs. duty cycle characteristics of the power electronic interface.

In addition, the SSHC is employed during normal irradiance conditions, while during partial shading conditions either HC-SS or ABC algorithms according to the PV-curve type.

The performance of this technique is validated by simulation and experimental results. The proposed HC-SS-ABC is compared to the HC algorithm based P-V curve scanning technique and ABC algorithm.

The obtained results show that the proposed hybrid GMPPT technique has a fast convergence speed and high efficiency compared to the two technique mentioned. This hybrid algorithm is used for battery charging applications.

IV.3.18. Adaptive salp swarm and differential evolution-perturb & observe technique (ASSADE-P&O)

[48] proposed a HGMPPT technique named adaptive SSADE–P&O which integrates SSA, DE and P&O algorithms. In the proposed method, the algorithm control parameters are adaptively adjusted to avoid needless power oscillations even after achieving the global peak region (GP) by SSA owing to dependency of the algorithm control parameter on the maximum iteration count. The combination of the SSA with the modified ED results in more accurate GMPP tracking with few search agents. Further in the identified GP region, the tracking is moved to the variable-step P&O, resulting in more accurate GMPP tracking and reduced power oscillations in the steady-state. In order to get the rapid MPP tracking during load changes direct duty ratio calculation is adapted without reinitializing the GP region identification stage.

The proposed algorithm is accurate and fast and has low power oscillations during tracking around MPP.

The proposed hybrid technique is verified with Matlab/Simulink model and by using hardware prototype developed. The superiority of the proposed method is compared the comparison of ASSADE-P&O method with SSA, ASSA, ASSADE MPPT methods which exist confirmed the superiority of the proposed technique in terms of tracking time and accuracy under complex partial shading conditions as well as load changes.

IV.4. Other HGMPPT methods

Various other hybrid techniques can be found in the literature but it is not possible to cover all techniques here. We mention the following:

IV.4.1. Direct adaptive neural control and voltage traverse (DANNC-VT)

An adaptive neural network control is combined with the feedback load voltage traverse (VT). Initially, the feedback load VT method achieve the reference voltage, and next the DANNC learning algorithm stabilize the maximum value [49].

The simulation results demonstrate that the proposed hybrid method track efficiently the GMPP under PSC. The proposed hybrid DANNC-VT technique is simple and more accurate and stable than other traditional algorithms.

IV.4.2. PSO algorithm and intermediate power point tracking algorithm (PSO-IPPT)

This hybrid technique integrates the PSO method and intermediate power point tracking algorithm (IPPT). The PSO technique is employed to track the global MPP under partial shading conditions whereas the IPPT algorithm is used to reach any other set point [50].

IV.4.3. Modified perturb and observe and checking algorithm (MP&O-CHECKA)

An enhanced P&O is mixed with a checking algorithm in [51]. In this method, the checking algorithm is introduced into a modified P&O algorithm. The checking algorithm detect the global maximum power by comparing all existed peak points, the modified P&O algorithm identify the voltage at MPP, required to calculate the duty cycle of the boost converter.

The Simulation results proved that the proposed technique track effectively the GMP. This method has many advantage such as the accuracy and simplicity of the algorithm and hence the possibility of implementation using low cost microcontroller.

IV.4.4. Gaussian process regression and Jaya algorithm (GPR-JAYA)

A hybrid of GPR and Jaya algorithm was proposed for photovoltaic system operating under PSC in [52].

To improve the tracking performance with Jaya algorithm, a GPR model is added into the iterative updates of candidate solutions (operating voltages).

The GPR model has the role of a predictor of PV power generations. Candidate solutions that do not improve PV power generations considered by the GPR model will be rejected during iterative updates, which reduce worse updates.

The effectiveness and efficiency of the proposed method is validated by simulation. Results obtained from simulation show that the GPR-Jaya outperforms standard Jaya algorithm and particle swarm optimization (PSO) algorithms in terms of dynamical efficiency and convergence speed.

IV.4.5. Hybrid P&O based multi-peak MPPT algorithms (P&O-MPT)

[53] presented a hybrid GMPPT algorithm under PSC combining five methods which includes the global scanning method, the filtering method, the binary searching method, the three-point method, and the anti-restarting method. The global scanning method finds all the local intervals, the filtering method reduces the search area, the binary searching method reduces the search time, the three-point method track the GMPP dynamically, and the anti-restarting method prevents restarting the algorithm.

The proposed P&O-MPT algorithm is illustrated in Fig.17.
The integration of benefit of all this methods allows to improve the efficiency and tracking speed, reduce the oscillation, and avoid restarting.

The results show that the proposed algorithm has a high performance such as system oscillation, tracking efficiency and speed. In addition, this algorithm is accurate and has fast respond fast in case of dynamic changes of irradiance (or temperature).

According the authors, the proposed algorithm is easily to be implemented using a low-cost microcontroller.

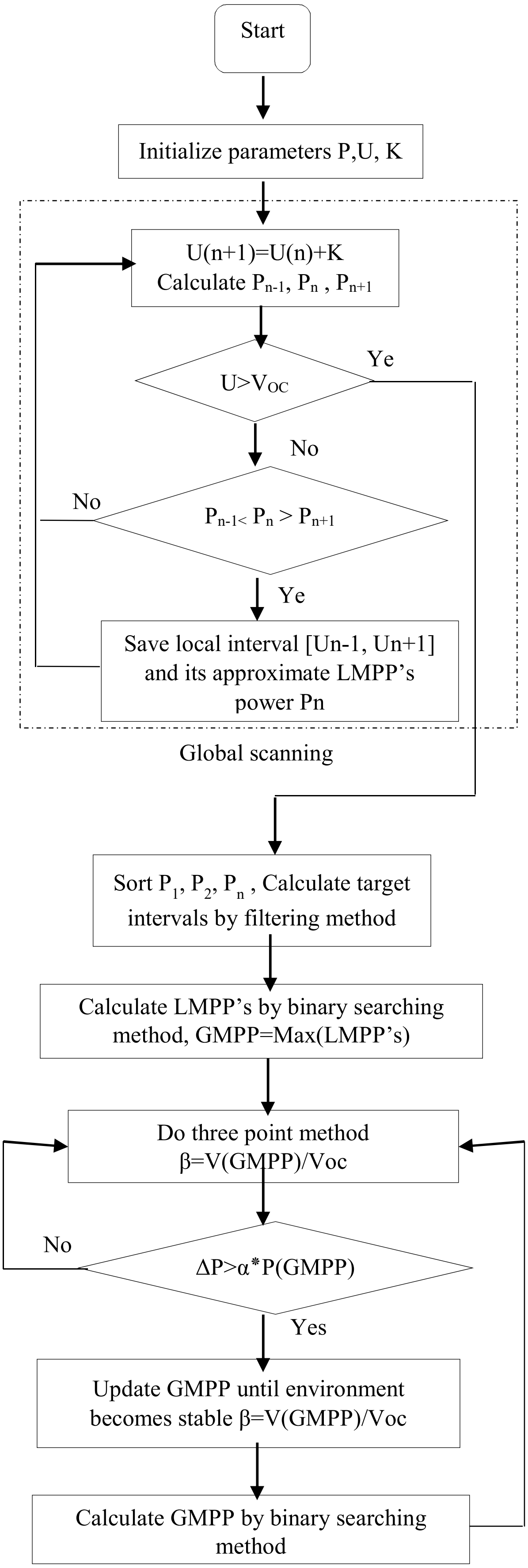

Fig.17: The flowchart of the proposed Hybrid P&O-MPT algorithms [53].

IV.4.6. Artificial neural network algorithm and segmentation algorithms (ANN-SEG)

[54] implemented an easy and cost effective HGMPPT technique to ensure a fast tracking of the global MPP. The proposed technique comprises a two stages searching method. The first stage combines an algorithm based on standard segmentation and an artificial neural network to identify the best operating point of the PV array subjected to continuously

variable environmental conditions. The second stage uses a hill-climbing method to finely track the precise GMPP location. The proposed method exploits a simple neural structure which consists only of six neurons in the hidden layer integrated with segmentation technique avoiding a complex ANN structure.

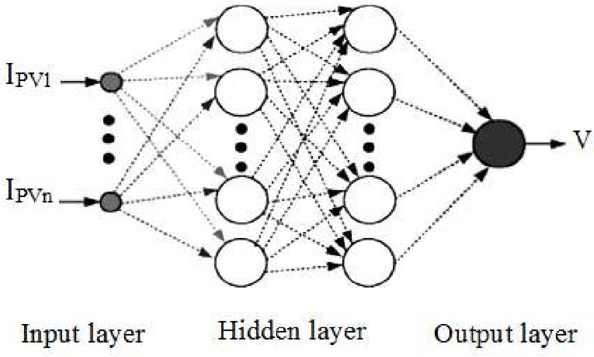

Fig.18: Neural network structure [54].

V.COMPARISON AND DISCUSSION

Availability of great number of techniques, impose to have a rigorous comparison to select the best one for a particular application. In this section, the following table depicts a performance comparison of different HGMPPT methods according the following parameters: convergence speed, complexity level, experimental implementation, efficiency, etc.

The analysis and evaluation of different HGMPPT techniques under PSC according to previous reviewed studies show that the hybrid techniques are the most useful methods in comparison with other MPP tracking methods.

- All hybrid control methods are efficient in tracking GMPP under PS and all weather conditions.
- The hybrid algorithms contributes to the improvement of PV array accuracy and efficiency under partial and changing environmental conditions.
- Hybrid methods based on classical algorithms are simple compared to hybrid methods based on conventional-soft computing and soft-computing soft computing based methods.
- Hybrid methods based on classical algorithms are less effective under partial shading compared to hybrid methods based on conventional-soft computing and soft-computing soft computing based methods.
- Hybrid methods based on conventional-soft computing and soft-computing- soft computing based methods are more effective in GMPP tracking.
- The use of two or more MPPT algorithms helps to overcome the drawbacks of individual MPPT algorithms when used alone.

Table I

PERFORMANCES OF DIFFERENT HGMPPT TECHNIQUES UNDER PSC.

Refs	HGMPPT	Complexity level	Tracking speed(s)	Efficiency (%)	converter	Appl-ication	Experimental Validation
[7]	FOCV-P&O	Simple	12.91	73.75	Buck	SA	Yes
[7]	FOCV-PIT	Simple	11.27	68.22	Buck	SA	Yes
[8]	FOCV-INC	Simple	<0.2	NA	Boost	SA	No
[9]	I0.8 V_{OC} mode-SPSP	Medium	5	97.39	SEPIC	GC DMPP	Yes
[10]	OCV-SCC	Simple	NA	NA	Buck	NA	Yes
[11]	DEA-PSO	Simple	<0.5	~98	SEPIC	SA	Yes
[12]	WOA-DEA	High	1.23	99.10	Boost	SA	Yes
[13]	JAYA-DEA	High	0.44	NA	Boost	SA	Yes
[14]	SAA-PSO	High	0.13	NA	Boost	SA	No
[15]	MGA-FFA	Medium	0.036	99.26	Buck	SA	Yes
[16]	GWO-GSO	High	0.64	99.99	Boost	SA	Yes
[17]	GWO-β	High	0.46	99.98	Boost	SA	No
[18]	OD-PSO	Medium	1.86	97.74	Buck	SA	Yes
[19]	PSO-GSA	Medium	8.75	99.99	Boost	SA	No
[20]	PSO-ANFIS	Medium	0.15	99.43	Boost	SA	No
[21]	GWO-FLC	High	NA	99.99	Boost	GC	No
[22]	GRNN-SFO	Medium	0,066	99.9%	Boost	SA	No
[24]	ANN-P&O	Medium	NA	NA	Buck	SA	Yes
[26]	ANN-HC	Medium	NA	NA	NA	NA	NA
[27]	FLC-P&O	Simple	1	>99.9	NA	SA	No
[28]	PSO-INC	Medium	~1	>99	NA	SA	No
[33]	PSO-P&O	Medium	0.9	NA	Boost	SA	No
[32]	PSO-P&O	Medium	NA	NA	Buck-boost	SA	Yes
[36]	PSO-HC	Medium	NA	NA	NA	SA	No

[37]	PSO-PI	Low	0.42	99.94	Buck-boost	SA	No
[38]	SAA-P&O	Medium	NA	NA	NA	SA	No
[39]	GWO- P&O	Medium	0.015	100	Boost	SA	Yes
[40]	WOA-P&O	Medium	NA	>96.7	NA	SA	Yes
[41]	ABC-P&O	Medium	0.08	99.93	Boost	SA	No
[42]	ACO-P&O	High	NA	>99.90	Boost	SA	Yes
[43]	INC-FFA	Medium	0.38	99.99	Boost	SA	Yes
[44]	FWA-P&O	Medium	NA	NA	Boost	SA	Yes
[45]	MBAT- P&O	Medium	NA	99.85	Buck-boost	SA	No
[46]	GSA-P&O	Medium	3	99.90	Boost	SA	Yes
[47]	HC-ABC	High	1.03	99.17	Boost	GC	Yes
[48]	ASSADE-P&O	Medium	1.36	99.68	Boost	SA	Yes
[49]	DANNC-VT	Low	0.0389	99.98	Boost	SA	
[50]	PSO-IPPT	Medium	NA	NA	Boost	SA	Yes
[51]	P&O-HECKA	Low	NA	100	Boost	SA	
[52]	GPR-JAYA	Medium	<2	>99		SA	No
[53]	P&O-MPT	Medium	~0.1	>99	NA	SA	No
[54]	ANN-SEG	Simple	NA	NA	Full bridge Power converter	SA	Yes

SA: Standalone, NA: Not Available, GC: Grid Connected

VI. CONCLUSION

In the literature, there are a large number of studies dealing with GMPP tracking under PSC. Thus, it is extremely delicate to pick the proper method by the designer with existence the huge studies number. For this reason, this review selected the studies that concern the most important HGMPPT methods published in the literature, revealing the advantages and drawbacks of each reviewed technique.

In addition, this work classifies different hybrid methods from the literature in four main categories. After the relevant evaluations of all surveyed methods, a table summarizing the performance has been presented, which makes it possible to choose the adequate HGMPPT technique for any application.

REFERENCES

[1] F. Belhachat, C. Larbes, “A review of global maximum power point tracking techniques of photovoltaic system under partial shading conditions”, Renew. Sustain. Energy Rev., vol 92, pp.513–553, 2018. https://doi.org/10.1016/j.rser.2018.04.094.

[2] F. Belhachat, C, Larbes, “Comprehensive review on global maximum power point tracking techniques for PV systems subjected to partial shading conditions”, Sol. Energy.,vol. 183, pp.476–500, 2019. https://doi.org/10.1016/j.solener.2019.03.045.

[3] F. Belhachat, C. Larbes, “Modeling, analysis and comparison of solar photovoltaic array configurations under partial shading conditions”, Sol. Energy 120, 399–418, 2015. https://doi.org/10.1016/j.solener.2015.07.039.

[4] F. Belhachat, C. Larbes, “Global maximum power point tracking based on ANFIS approach for PV array configurations under partial shading conditions”, Renew. Sustain. Energy Rev., vol.77, pp.875–889, 2017. https://doi.org/10.1016/j.rser.2017.02.056.

[5] F. Belhachat, C. Larbes, “PV array reconfiguration techniques for maximum power optimization under partial shading conditions”: A review, Sol Energy., vol.230, pp. 558–582, 2021. https://doi.org/10.1016/j.solener.2021.09.089.

[6] MH. Zafar, N M.Khan, A.Feroz Mirza, M.Mansoo, “Bio-inspired optimization algorithms based maximum power point tracking technique for photovoltaic systems under partial shading and complex partial shading conditions”, Journal of Cleaner Production, Vol 309, 127279, 2021. https://doi.org/10.1016/j.jclepro.2021.127279.

[7] MR. Al-Soeidat, A. Cembrano, D.C Dylan Lu, “Comparing Effectiveness of Hybrid MPPT Algorithms under Partial Shading Conditions, IEEE International Conference on Power System Technology, 2016. DOI :0.1109/POWERCON.2016.7754024.

[8] M.Y. Javed, M.M. Gulzar, S.T.H.Rizvi, “A Hybrid Technique to Harvest Maximum Power from PV Systems under Partial Shading Conditions”, International Conference on Emerging Technologies (ICET), Islamabad, Pakistan, 2016. DOI: 10.1109/ICET.2016.7813203.

[9] M.E. Başoğlu, B.Çakır, “Hybrid global maximum power point tracking approach for photovoltaic power optimisers”, IET Renew Power Gener., vol.12, no.8, pp.875–882, 2018.

[10] M.Ostrowski, “An adaptive OCV and SCC-based maximum power point tracking method for photovoltaic panels in the partial shading conditions”. IEEE International Conference on Environment and Electrical Engineering and IEEE Industrial and Commercial Power Systems Europe (EEEIC/I&CPS Europe), Palermo, Italy, 2018.

[11] M. Seyedmahmoudian, R.Rahmani, “Simulation and Hardware Implementation of New Maximum Power Point Tracking Technique for Partially Shaded PV System Using Hybrid DEPSO Method”, IEEE Transactions on Sustainable Energy.,vol. 6,no.3,pp. 850 – 862, 2015.

[12] N. Kumar, I. Hussain, B. Singh, B.K. Panigrahi, “MPPT in Dynamic Condition of Partially Shaded PV System by using WODE Technique”, IEEE Transactions on Sustainable Energy., vol. 8, no.3, pp.1204 - 1214, 2017. DOI: 10.1109/TSTE.2017.2669525

[13] N. Kumar, I. Hussain, B. Singh, B.K. Panigrahi “Rapid MPPT for Uniformly and Partial Shaded PV System by using JayaDE Algorithm in Highly Fluctuating Atmospheric Conditions”, IEEE Transactions on Industrial Informatics., vol.13, no. 5, pp. 2406–2416, 2017. DOI: 10.1109/TII.2017.2700327.

[14] T. Guan, F. Zhuo, “An Improved SA-PSO Global Maximum Power Point Tracking Method of Photovoltaic System under Partial Shading Conditions”, IEEE International Conference on Environment and Electrical Engineering and IEEE Industrial and Commercial Power Systems Europe (EEEIC/I&CPS Europe), Milan, Italy, 2017. DOI: 10.1109/EEEIC.2017.7977804

[15] Y.P.Huang, X. Chen, C.E .Ye, “A hybrid maximum power point tracking approach for photovoltaic systems under partial shading conditions using a modified genetic algorithm and the firefly algorithm”, Int. J. Photoenergy., pp.1–13, 2018.

[16] J.Y. Shi, D.Y.Zhang, L.T.Ling, T.Yang, “Dual-algorithm maximum power point tracking control method for photovoltaic systems based on grey wolf optimization and golden-section optimization”, J. Power Electron., vol.18,no.3, pp.841–852, 2018.

[17] M.V.Rocha, L.P. Sampaio, S.A.O. da Silva, “Maximum power point extraction in PV array under partial shading conditions using GWO-assisted Beta method”. In: Proceedings of the International Conference on Renewable Energies and Power Quality (ICREPQ’18). Salamanca, Spain, 21–23 March, vol. 1, no.16, pp. 450–455, 2018.

[18] H. Li, D. Yang, W. Su, J. Lü, X. Yu, “An overall distribution particle swarm optimization MPPT algorithm for photovoltaic system under partial shading”, IEEE Trans. Ind. Electron., vol .66, no. 1, pp.265–275, 2018. https://doi.org/10.1109/TIE.2018.2829668.

[19] A. M. Mohamed, A. Ahmed Zaki Diab, H. Rezk, “Partial Shading Mitigation of PV Systems via Different Meta-Heuristic Techniques”, Renewable Energy. Vol.130, pp. 1159-1175, 2019.

[20] J. Farzaneh, R. Keypour, A. Karsaz, "A novel fast maximum power point tracking for a PV system using hybrid PSO-ANFIS algorithm under partial shading conditions"., International Journal of Industrial Electronics, Control and Optimization., vol. 2, no.1, pp. 47-58, 2019.

[21] A.M. Eltamaly, M.H. Farh Hassan., "Dynamic global maximum power point tracking of the PV systems under variant partial shading using hybrid GWO-FLC", Solar Energy,.vol.177, pp.306–316, 2019.

[22] N.M. Khan, U.A. Khan, M.H. Zafar, "Maximum Power Point Tracking of PV System under Uniform Irradiance and Partial Shading Conditions using Machine Learning Algorithm Trained by Sailfish Optimizer", 4th International Conference on Energy Conservation and Efficiency (ICECE). Lahore, Pakistan, 2021.

[23] L. Jiang, L. Maskel Douglas, "A simple hybrid MPPT technique for photovoltaic systems under rapidly changing partial shading conditions", 2014 IEEE 40th Photovoltaic Specialist Conference (PVSC), 2014. . Denver, CO, USA. DOI: 10.1109/PVSC.2014.6925034,

[24] L.L. Jiang, D.R. Nayanasiri, L. Maskell Douglas, D.M. Vilathgamuwa, "A hybrid maximum power point tracking for partially shaded photovoltaic systems in the tropics", Renewable Energy., Vol.76, pp.53-65, 2015.

[25] H.M. El-Helw, A. Magdy, M.I. Marei, "A Hybrid Maximum Power Point Tracking Technique for Partially Shaded Photovoltaic Arrays", IEEE Access., Vol. 5, pp.11900–11908, 2017. DOI: 10.1109/ACCESS.2017.2717540.

[26] S.A. Rizzo, N. Salerno, G. Scelba, A. Sciacca, "Enhanced Hybrid Global MPPT Algorithm for PV Systems Operating under Fast-Changing Partial Shading Conditions", International Journal of Renewable Energy Research., Vol. 8, no. 1, pp.221-229, 2018.

[27] A. Al –Gizi, A. Craciunescu, M.A. Fadel, M. Louzazni, "A new hybrid algorithm for photovoltaic maximum power point tracking under partial shading conditions, Rev. Roum. Sci. Techn.– Électrotechn. et Énerg., Vol. 63, no.1, pp. 52–57, Bucarest, 2018.

[28] M. Abdulkadir, Y.A.H. Mohammed, "Hybrid Maximum power Point Tracking Technique Based on PSO and Incremental Conductance", IEEE Conference on Energy Conversion (CENCON), Johor Bahru, Malaysia, 2014. DOI : 10.1109/CENCON.2014.6967514.

[29] J. Shi, W. Zhang, Y. Zhang, F. Xue, T. Yang., "MPPT for PV systems based on a dormant PSO algorithm", Electric Power Systems Research., Vol.123, pp. 100–107, 2015.

[30] K.L.Lian, J. H. JHang, I. S. Tian, "A Maximum Power Point Tracking Method Based on Perturb-and-Observe Combined With Particle Swarm Optimization", IEEE Journal of photovoltaics., vol.4, no.2,pp. 626-633, 2014. DOI: 10.1109/JPHOTOV.2013.2297513.

[31] N. Foster, B. McCray, S. McWhorter, "A Hybrid Particle Swarm Optimization Algorithm for Maximum Power Point Tracking of Solar Photovoltaic Systems", Proceedings of The National Conference On Undergraduate Research (NCUR) 2017 University of Memphis, Tennessee April 6-8, pp. 207-214, 2017.

[32] M. Kermadi, Z. Salam, J.Ahmed, E.M. Berkouk, "An Effective Hybrid Maximum Power Point Tracker of Photovoltaic Arrays for Complex Partial Shading Conditions". IEEE Transactions on Industrial Electronics., 2018. DOI: 10.1109/TIE.2018.2877202.

[33] S.Hanafiah, A. Ayad, A.Hehn, R.Kennel,. "A Hybrid MPPT for Quasi-Z-Source Inverters in PV Applications under Partial Shading Condition", 2017 11th IEEE International Conference on Compatibility, Power Electronics and Power Engineering (CPE-POWERENG), pp. 418-423, 2017. DOI: 10.1109/CPE.2017.7915208.

[34] E. Avila, N. Pozo, E. Pozo, G. Salazar, X. Dominguez, "Improved Particle Swarm Optimization Based MPPT for PV Systems under Partial Shading Conditions", IEEE Southern Power Electronics Conference (SPEC). Puerto Varas, Chile, 2017. DOI: 10.1109/SPEC.2017.8333634.

[35] J.P. Ram, D.S. Pillai, N. Rajasekar, S.M.Strachan, "Detection and Identification of Global Maximum Power Point Operation in Solar PV Applications Using a Hybrid ELPSO-P&O Tracking Technique". IEEE Journal of Emerging and Selected Topics in Power Electronics., vol. 8, no.2, pp.1361-1374, 2020.

[36] K. Basinski, B. Unfalski, L.M.Grzesiak, "Hybrid MPPT algorithm for PV systems under partially shaded conditions using a stochastic evolutionary search and a deterministic hill climbing", Power Electronics and Drives., vol. 2, no. 37, 2017. DOI: 10.5277/PED170212.

[37] M. Kermadi, E.M. Berkouk, "A Hybrid PSO-PI Based Maximum Power Point Tracking Algorithm using Adaptive Sampling Time Strategy", 4th International Conference on Electrical Engineering (ICEE), 2015. DOI: 10.1109/INTEE.2015.7416787.

[38] S. Lyden, M. E, Haque, "A Hybrid Simulated Annealing and Perturb and Observe Method for Maximum Power Point Tracking in PV Systems under Partial Shading Conditions", Australasian Universities Power Engineering Conference (AUPEC), 2015. DOI: 10.1109/AUPEC.2015.7324803.

[39] S.Mohanty,B. Subudhi, P. Kumar Ray, "A Grey Wolf Assisted Perturb & Observe MPPT Algorithm for a PV System". IEEE Transactions on Energy Conversion., vol.32, no.1, pp. 340 – 347, 2017. DOI: 10.1109/TEC.2016.2633722.

[40] M. Premkumar, R. Sumithira, "Humpback Whale Assisted Hybrid Maximum Power Point Tracking Algorithm for Partially Shaded Solar Photovoltaic Systems", Journal of Power Electronics., vol 18, no.(6), pp.1805-1818, 2018.

[41] D. Pilakkat, S. Kanthalakshmi, An improved P&O algorithm integrated with artificial bee colony for photovoltaic systems under partial shading conditions". Sol.Energy. vol .178, pp.37–47, 2019.

[42] R.Selvakumar, M. Sujatha, S.Palanikumar, "ROAC: Recursive optimization of Ant colony assisted perturb and observe for a photovoltaic resonant boost converter", International Journal of Engineering & Technology., vol. 7, no.13, pp.150-156, 2018.

[43] J.Y.Shi, L.T.Ling, F. Xue, Z.J.Qin, Y. Li, Z.X.Lai, T.Yang, "Combining incremental conductance and firefly algorithm for tracking the global MPP of PV arrays", Journal of Renewable and Sustainable Energy., 9, 2017. Doi: 10.1063/1.4977213.

[44] C. Manickam,, G.P. Raman,, G.R. Raman, S.I. Ganesan, N. Chilakapati, "Fireworks Enriched P&O Algorithm for GMPPT and Detection of Partial Shading in PV Systems". IEEE Transactions on Power Electronics., vol. 32, no.6, pp.4432–4443, 2017. DOI: 10.1109/TPEL.2016.2604279.

[45] M.K. Karagoz, H. Dermirel, "A Novel MPPT Method for PV Arrays Based on Modified Bat Algorithm with Partial Shading Capability", IJCSNS International Journal of Computer Science and Network Security.,vol.17, no.2, pp. 61-66, 2017.

[46] K. Sundareswaran, V. Vigneshkumar, S.P.Simon, P. Srinivasa Rao Nayak, "Gravitational search algorithm combined with P&O method for MPPT in PV systems", IEEE Annual India Conference (INDICON), India, 2016.

[47] G.J. Saikrishna, R. Kalpana, B.Singh, "A hybrid global maximum power point tracking technique with fast convergence speed for partial shaded PV systems", IEEE Trans. Ind. Appl., vol. 54, no.5, pp. 5367–5376, 2018. https://doi.org/10.1109/TIA.2018.2845415.

[48] D.K. Mathi, R.Chinthamalla, "A hybrid global maximum power point tracking of partially shaded PV system under load variation by using adaptive salp swarm and differential evolution – perturb & observe technique", Energy Sources, Part A: Recovery, Utilization, and Environmental Effects., vol.43, no.20, 2021.

[49] Z. Xiao-qiang, C. Ke, C, Z.Ying-quan, Z. Cui-fang, R. Guang-chao, "A direct adaptive neural control with voltage traverse for maximum power point tracking of photovoltaic system", In: Proceedings of the IEEE 29th Chinese control and decision conference (CCDC); 2017. pp. 4493–8.2017. DOI: 10.1109/CCDC.2017.7979290.

[50] Guichi, A. Talha, E.M. Berkouk, S.Mekhilef, S. Gassab, "A new method for intermediate power point tracking for PV generator under partially shaded conditions in hybrid system", Solar Energy., vol. 170, pp.974–987, 2018. https://doi.org/10.1016/j.solener.2018.06.027.

[51] R. Alik, A. Jusoh, "Modified Perturb and Observe (P&O) with checking algorithm under various solar irradiation", Solar Energy., vol.148, pp.128-139, 2017. https://doi.org/10.1016/j.solener.2017.03.064.

[52] C. Huang, L. Wang, L. Huan, X. Luo, J.H. Wang, " A Hybrid Global Maximum Power Point Tracking Method for Photovoltaic Arrays under Partial Shading Conditions, Optik.,vol. 180, pp.665-674, 2019. https://doi.org/10.1016/j.ijleo.2018.11.158.

[53] Y. Songsen, X. Zhang, L.Yin, "Hybrid global maximum power point tracking algorithm under partial shading condition", Journal of renewable and sustainable energy., vol.10, 063504, 2018. https://doi.org/10.1063/1.5041370.

[54] S.A. Rizzo, G.Scelba, "A hybrid global MPPT searching method for fast variable shading conditions", Journal of Cleaner Production., vol. 298, 2021. https://doi.org/10.1016/j.jclepro.2021.126775.

Faiza Belhachat received the diploma of electronic engineering degree from the university of Science and Technology Houari Boumedienne (USTHB), Algiers; the diploma of magister degree in electronic from the Ecole nationale polytechnique (ENP), Algiers Algeria; and also the Doctorate in science degree in electronic engineering from the ENP. Her current research interests include artificial intelligence, photovoltaic systems, embedded sysems. The author has several publications in the field of photovoltaic solar energy.

Cherif Larbes received the “Ingeniorat d’Etat” degree in electronics from Ecole Nationale Polytechnique, Algiers, Algeria, in 1985 and the Ph.D degree in engineering from the University of Lancaster, UK, in 1990. He is currently a Full Professor with the Department of Electronics, Ecole Nationale Polytechnique, Algiers, Algeria. He is the director of the “Dispositifs de Communication et de Conversion Photovoltaïque" Research Laboratory (LDCCP). His current research interests include intelligent control, power converters, electrical machine drives and photovoltaic systems. He authored over 100 journal and conference papers.

Objective Evaluation of the Pathological Voice Based on Deep Learning Neural Networks in an Algerian hospital environment

Mahraz Kabache and Mhania Guerti

Abstract− In this study, we propose a method based on Recurrent Neural Networks, to objectively evaluate the process of rehabilitation of the pathological voice, in an Algerian clinical environment. We choose Unilateral Laryngeal Paralysis as the pathology of the voice. In this paper, we used a Deep Learning system of pathological voice detection by Long Short Term Memory neural model (LSTM). As the dysphony studied in our work concerns essentially the laryngeal vibration, we choose the acoustic parameters based on the instability of the frequency and the amplitude of the laryngeal vibration: Jitter and Shimmer, Noise parameters and Cepstraux MFCC coefficients (Mel Frequency Cepstral Coefficients). A pathological voice detection rate of 88.65% shows important results brought by the rehabilitation technique adopted in Algerian clinical setting. The exclusive and abusive use of hearing to evaluate the effect of speech rehabilitation in the Algerian hospital environment remains insufficient. It is important to correlate perceptual data with objective methods based on detection and classification methods by introducing relevant acoustic parameters, for an effective and objective management of vocal pathology assessment.

***Keywords*− Voice Pathology, *Unilateral Laryngeal Paralysis,* Deep Learning, LSTM Recurring Neural Networks.**

NOMENCLATURE

LSTM	Long Short Term Memory.
MFCC	Mel Frequency Cepstral Coefficients
GMM	Gaussian Mixture Models.
KNN	K-Nearest Neighbors.
SVM	Support Vector Machines.
RNN	Recurring Neural Networks.
CPP	Cepstral Peak Prominence.
HPR	High-frequency Power Ratio.
HNR	Harmonic to Noise Ratio.
ANN	Artificial Neural Network.

I. INTRODUCTION

Assessing the quality of the voice is an important issue for laryngo-phoniatria in order to validate the relevance and effectiveness of the treatments proposed, whether they are rehabilitation or phono-surgery. In this sense, the ear-based judgment, also known as subjective or perceptive evaluation terminology, is the only method of analysis and evaluation of pathological voice used in Algerian clinical environment [1, 2, 3]. In this method, the rehabilitative speech therapist is the only one in charge of listening to the quality of the voice, which results in an unreliable perceptive evaluation, given that reliable perceptive analysis involving several expert auditors and several listening sessions is ultimately time consuming and human resources consuming, and does not allow regular use in clinical routine [3,4,5].

Another major drawback of subjective evaluation is inter- and intra-listener variability in voice perception by a jury of experts. This variability can be influenced by the context, emotional state or attention of the listener [6].

In this work, we will develop a system of automatic detection and evaluation of pathological voice using LSTM-type Recurring Neural Networks. We will use in this system a discriminant acoustic analysis based on pathological acoustic parameters. The objective is to show that the use of RN in the re-education evaluation process with the introduction of pathological indices reflecting the malfunction of vocal strings, in the extraction phase of acoustic vectors, can significantly improve and facilitate voice assessment during rehabilitation.

II. LARAYNGEAL PARALYSIS

Dysphonia is an alteration of the voice resulting in the isolated or combined achievement of the three acoustic parameters of the voice which are the pitch, intensity and timbre. The main causes of dysphonia are functional disorders, organic alterations or neurological affected. Laryngeal immobility is defined as a complete decrease or stop of the abduction and/or abduction movement of the larynx (Figure 1). Depending on their laryngeal topography (uni or bilateral, position rather abduction or adduction), they will expose to a vital risk due to respiratory or swallowing problems and to a functional risk related to the various functions of the larynx: phonation, swallowing and breathing.

Unilateral paralysis accounts for 90% of laryngeal paralysis. They are more common on the left, probably for anatomical reasons (longer path on this side) [2]. The voice of a laryngeal paralysis is blown and hoarsely with a significant air leak causing shortness of breath at the end of sentences and a continuous projected voice impossible.

Manuscript received July 11, 2022; revised December 16, 2022.

M. Kabache and M. Guerti are with Ecole Nationale Polytechnique, Algiers, ALGERIA. (e-mails: mahraz.kabache@g.enp.edu.dz, mhania.guerti@g.enp.edu.dz).

Digital Object Identifier (DOI): 10.53907/enpesj.v2i2.170

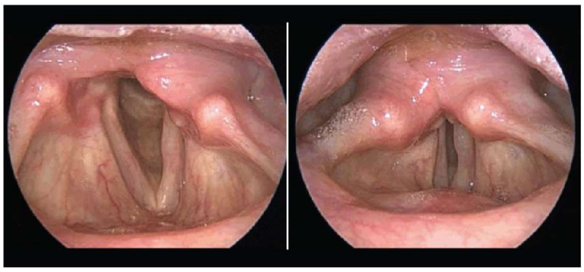

Fig. 1: Pictures representing two larynx, right healthy vocal cords, left unilateral paralysis of the left vocal cord.

III. PATHOLOGICAL VOICE CLASSIFICATION TECHNIQUES

An automatic evaluation system can discriminate between normal and pathological samples and classify voice pathologies. The process of differentiating between normal and pathological subjects is a two-class problem called pathology detection. On the other hand, identify different types of pathology is a multi-class problem called pathology classification.

Among the methods used in the detection and automatic classification of pathological voice, we cite Artificial Neural Network ANN, models based on Gaussian mixtures adapted from a generic GMM speech model, the K Nearest Neighbor classifier KNN, SVM support vector machines, etc. Table. I summarises research work on pathological speech and voice detection and classification systems, and their methodologies on the acoustic analysis used, the type of classifier and the corpus chosen.

Table. I

MODELS OF CLASSIFIERS

Reference	Selected Features	Classifier Model	Corpus used
[7]	MFCC	GMM	Vowels [a], [i] and [u]
[8]	MFCC	SVM	Speech segment of 1.5 sec
[9]	MFCC, Jitter, Shimmer et HNR	SVM	Vowels [a], [i] and [u], continuous speech
[10]	MFCC	Comparison SVM et GMM	Vowels [a], [i] [u], continuous speech and EGG signals
[11]	MFCC	hybrid model SVM /GMM	Vowels
[12]	HNR, critical band of the energy spectrum	KNN	Vowels
[13]	Voice signal preprocessing	DNN	Vowels [a], [i] [u] and EGG signals

IV. LONG SHORT TERM MEMORY RECURRING NETWORKS

Long Short Term Memory Network (LSTM) are the special type of Recurrent Neural Networks capable of learning long term dependencies (figure II).

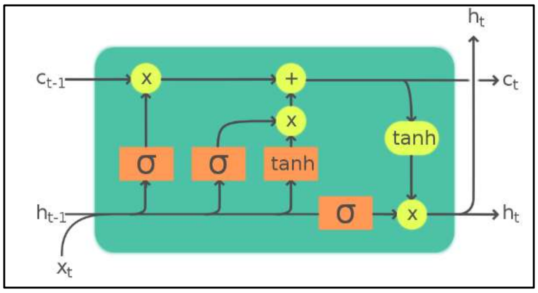

Fig. 2: *Diagram of an LSTM cell [14]*

LSTM cell contains three gates: *forget gate, Input gate* and *Output gate*. Forget gate layer decides what information has to be kept or thrown away from the cell state. It takes input as h_{t-1} and x_t and outputs a number between 0 and 1 using the sigmoid function σ, the output f_t as in the Equation (1). Value of 0 indicates completely remove and 1 to completely keep this.

$$f_t = \sigma\,(W_{hf}\,h_{t-1} + W_{xf}\,x_t) \tag{1}$$

Now we need to decide what information has to be stored in the cell state. It has two parts, firstly input gate layer using to decide what values has to be updated and then tanh layer generates a vector of new candidate values that has to be added. i_t is the function used by input gate layer and C is the vector of new candidate values by *tanh* layer as shown in the equation (2) and (3).

$$i_t = \sigma\,(W_{hi}\,h_{t-1} + W_{xi}\,x_t) \tag{2}$$

$$C = \tanh\,(W_{hh}\,h_{t-1} + W_{xh}\,x_t) \tag{3}$$

The updated cell status is indicated by the following equation:

$$C_t = f_t * C_{t-1} + i_t * C \tag{4}$$

Finally, we need to decide what will be the output using output gate. First we run the sigmoid layer using o_t as shown in the Equation (5) and then its output is multiplied by *tanh* to get the output which is shown in the equation (6):

$$o_t = \sigma\,(W_{ho}\,h_{t-1} + W_{xo}\,x_t) \tag{5}$$

$$h_t = o_t * \tanh(C_t) \tag{6}$$

W_{hi}, W_{hf}, W_{hh}, W_{ho} *are the* recurrent connections between the previous hidden layer and current hidden layer. W_{xi}, W_{xh}, W_{xf}, W_{xo} *are* the weights matrix that connects the inputs to the hidden layer. *σ and tanh* are the activation functions.

V. MATERIALS AND METHODS APPLIED

A. *Selected population*

The subjects selected for this works consists of nine Algerian female patients aged 42 to 56 with Unilateral Laryngeal Paralysis (ULP), six are left and three are right. Patients over the age of 56 were eliminated in this study to give reliability to our results. A recording is made after a 9-month speech rehabilitation. In this study, we only selected patients who followed a regular rehabilitation protocol. The same corpus was pronounced by 3 normal female speakers between the ages of 40 and 50 years, not presenting voice disorders (reference standard).

B. Equipment and protocol recording

The voice corpus was recorded with an external M-audio pro sound card, with a Signal/Noise ratio of 100 dB and 16 bits of resolution. We selected a sampling frequency of 44.1 kHz. A dynamic microphone of the Sennheiser e815S type is used for recording with sound software Sound Forge version 10. The voice recordings were made in an acoustically quiet room to eliminate parasitic sound sources. When recording the vocal corpus, a distance of 5 cm is respected between the microphone and the patient's mouth. The microphone is placed at 45° laterally to the mouth, its gain has been adjusted to have an optimal quality of the recording and to avoid the saturation of the sound.

C. Corpus used

The corpus of sound recordings includes the vowel [a] for the various pathological parameters. The chosen corpus consists of 450 normal and pathological voice samples, used for learning, validation and testing. The detection corpus consists of 194 samples between normal and pathological.

D. Multi variable extraction of acoustic parameters

After the input signal preprocessing step a multi-variable acoustic analysis is applied to each frame. In order to have an optimal discrimination of our detection system, we took the Jitter and the Shimmer to evaluate the stability of the frequency and amplitude of the laryngeal vibration F0 of the voice, HNR, HPR, H_1-H_2 and CPP for noise analysis and we used the Mel Frequency Cepstral Coefficients (MFCC) (table. II).

Table. II
ACOUSTIC PARAMETERS USED

Acoustics Parameters		Dimension of the acoustic vector
Cepstral Parameter	MFCC	12
Fundamental frequency stability parameters	Jitter	1
	Shimmer	1
Noise parameters	HNR	1
	HPR	1
	H_1 –H_2	1
	CPP	1

E. System Architecture and Learning

The system has 6 layers of neurons: an input layer, an output layer and 4 hidden layers. The number of neurons in the input layer is set to 18. These inputs correspond to the input acoustic vector coefficients for each frame (window). The first hidden layer is limited to 100 neurons, it corresponds to the LSTM cell layer. This is followed by a dropout layer to avoid over-learning or learning by heart (Overfitting). The hidden third layer has two completely connected neurons (Fully Connected), represents the number of classes to ensure non-linearity of network activities. The hidden fourth layer is a softmax activation function with two neurons. The output layer contains a single neuron for decision (Pathological P or Normal N) (Figure III).

The learning rate is set at 0.001, the Dopout (neuron abandonment) is 0.5, the Epoch number is 50 and the batch size is set at 25. As a reminder, in Deep Learning, the Batch size is the number of learning examples in a forward and backward pass through the network. An epoch represents a pass back and forth only once of all learning data.

A. Confusion Matrix and Performance Evaluation

Pathological voice classification performance is represented by a two-dimensional array called the Confusion Matrix. Real voices are arranged in rows and predicted voices in columns (Table. III) [16, 17].

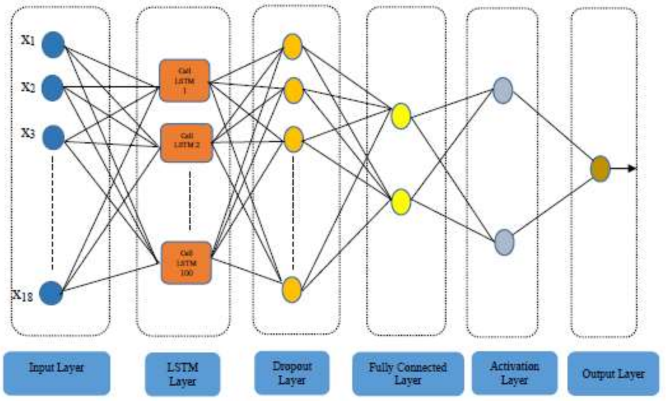

Fig. 3: Pathological Voice Detection System Architecture

B. Confusion Matrix and Performance Evaluation

Pathological voice classification performance is represented by a two-dimensional array called the Confusion Matrix. Real voices are arranged in rows and predicted voices in columns (Table. III) [16, 17].

Table. III
CONFUSION MATRIX

		Voice Detected		Total
		Normal Voice	Pathological Voice	
Real Voice	Normal Voice P	True Positive TP	False Negative FN	P= TP+FN
	Pathological Voice N	False Positive FP	True Negative TN	N= FP+TN

If a voice is positive (P) and is detected as positive, that is a positive voice correctly detected, it is counted as a True Positive (TP). If it is detected as negative, then it is considered a False Negative (FN). If a voice is negative and is detected as negative, it is considered as True Negative (TN), if it is detected as positive, so it is considered as False Positive (FP).

In order to measure the performance of a voice pathology detector or of the classification of the type of pathology, three main indices are taken into consideration: Accuracy, Sensitivity and Specificity [16, 17].

F.1. Accuracy

Is one of the measures commonly used for detection and classification performance. It is defined as a ratio between correctly detected voices and the total number of voices.

$$AC = \frac{TP+VN}{TP+FP+VN+FN} * 100 \qquad (8)$$

F.2. Sensitivity

Represents the True Positive Rate (TPR), it is the ability of a classifier to detect positive samples correctly classified in relation to the total number of positive samples. It is estimated by the following equation:

$$TPR = \frac{TP}{TP+FN} * 100 \qquad (9)$$

F.3. Specificity

It concerns negative or pathological samples, it represents the True Negative Rate (TNR), it is the ability of a classifier to detect negative samples correctly classified in relation to the total number of negative samples.

$$TNR = \frac{TN}{TN+} * 100 \qquad (10)$$

VI. OBTAINED RESULTS AND DISCUSSION

Figure 4 shows the training of the network, it shows the evolution of the Detection Rate (Accuracy) and the Cost (Loss) for the validation data according to the number of Epoch (or iteration number). We tested several values for this parameter, 50 Epoch is enough for a good convergence of the network and that no drop in performance appears beyond.

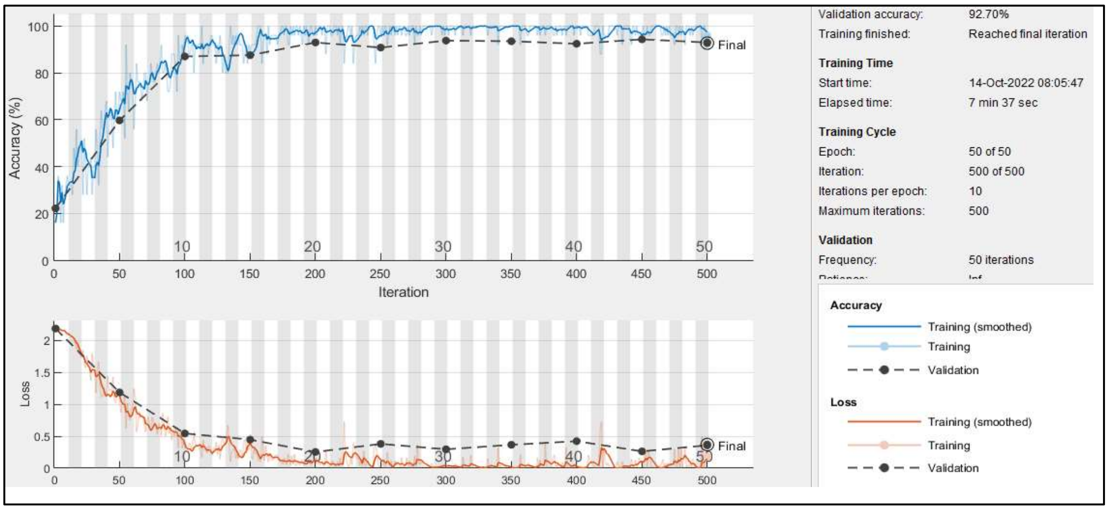

Validation accuracy: 92.70%
Training finished: Reached final iteration

Training Time
Start time: 14-Oct-2022 08:05:47
Elapsed time: 7 min 37 sec

Training Cycle
Epoch: 50 of 50
Iteration: 500 of 500
Iterations per epoch: 10
Maximum iterations: 500

Validation
Frequency: 50 iterations

Fig. 4: Evolution of the Accuracy Rate during learning depending on the number of Epoch

Tables IV and V illustrate the confusion matrices obtained by our detection system, for RUP before and after rehabilitation, indicating the overall detection rate represented by the accuracy as well as the sensitivity and specificity of the system.

We noticed a total detection (specificity) of pathological voice (100%) before rehabilitation with a high rate of system accuracy (95.87 %). After rehabilitation, we observed a confusion between normal and pathological voices resulting in a specificity rate of 83.33 % that decreased the accuracy of the system (88.65 %). This low rate of specificity is explained by a difference in the values of pathological parameters used in the values of pathological parameters used in acoustic analysis between normal and pathological voices after rehabilitation.

The sensitivity of our detection system is considered very high (92.72 %) given the inter-speaker and intra-speaker variability factor of the corpus that can cause performance difficulties for automatic speech recognition systems in general.
The significant difference between the specificity and sensitivity of the detection system is explained by the differences between the reference (normal) an pathological voices after rehabilitation of the different acoustic parameters.

Table. IV
CONFUSION MATRIX AND DETECTION RATE OBTAINED BEFORE REHABILITATION

		Voice Detected		Total	Accuracy AC (%)	Sensitivity TPR (%)	Specificity TNR (%)
		Normal Voice	Pathological Voice				
Real voice	Normal Voice P	**102**	8	110	**95.87**	**92.72**	**100**
	Pathological Voice N	00	**84**	84			

Table. V
CONFUSION MATRIX AND DETECTION RATE OBTAINED AFTER REHABILITATION

		Voice Detected		Total	Accuracy AC (%)	Sensitivity TPR (%)	Specificity TNR (%)
		Normal Voice	Pathological Voice				
Real voice	Normal Voice P	**102**	8	110	**88.65**	**92.72**	**83.33**
	Pathological Voice N	14	**70**	84			

VII. CONCLUSION

The LSTM ANN was implemented for pathological voice detection for the first time. Other machine learning tools such as vector support machines and artificial neural networks were already used in similar work [6] but for other pathologies. The application of LSTM recurrent neural networks, in an automatic classification (detection) system of pathological voice, allowed us to have appreciable results. The advantage of these Networks is that the input values transmitted to the network not only pass through several LSTM layers, but also propagate over time in an LSTM cell in order to avoid problems related to a long-term dependence. The problem of confusion between normal and pathological voices in the detection phase makes the use of neural networks alone, as an objective evaluation method in the speech therapy process ineffective, but it can help the speech pathologist in the detection and evaluation of pathological voice with other methods such as objective evaluation through acoustic and subjective analysis through listening.

REFERENCES

[1] M Kabache and M. Guerti, "Multi parametric method for the objective Acoustic Evaluation of the Voice Produced by laryngectomy patients", *Instrumentation, mésure et métrologie*, vol. *20, no. 3,* pp. 137-142, 2021, DOI: https://doi.org/10.18280/i2m.200303

[2] M Kabache and M. Guerti, "Acoustic Analysis of Voice Signal of Patients with Unilateral Laryngeal Paralysis a view to objective evaluation after rehabilitation", *Revue de Traitement de Signal*, vol.38, no. 5, pp.1339-1344, 2021, DOI:10.18280/ts.380508

[3] K. Ferrat and M. Guerti, "A study of sounds produced by Algerian esophageal speakers", *African Health Sciences*, vol. 12, no. 4, 2012, doi: 10.4314/ahs.v12i4.9.

[4] Yu. Ping M. Ouaknine, J. Revis, A. Giovanni, "Objective Voice Analysis for Dysphonic Patients: A Multiparametric Protocol Including Acoustic and Aerodynamic Measurements. *Journal of Voice*, vol. 15 no. 4 pp. 529–542. 2001, https://doi.org/10.1016/S0892-1997(01)00053-4.

[5] E. Saltürk, T. Özdemir, Z. Lütfi Kumral, , E. Karabacakoğlu, H. Kumral, G. Yildiz, , Y. Mersinlioğlu, , G. Atar, , G. Berkiten, Y. Yildirim, "Subjective and objective voice evaluation in Sjögren's syndrome", *Logopedics Phoniatrics Vocology*, vol. 42 no. 1, pp. 9-11. 2017, https://doi.org/10.3109/14015439.2015.1116606

[6] J. Kreiman, B. R Gerratti, , G. B. Kempster., A. Erman, G. S. Berke, "Perceptual Evaluation of Voice Quality: Review, Tutorial, and a Framework for Future Research*", Journal of Speech and Hearing Research*, vol. 36, pp. 21-40, 1996, https://doi.org/10.1044/jshr.3601.21

[7] L. Salhi, T. Mourad, A.Cherif, "Voice Disorders Identification Using Multilayer Neural Network". *The International Arab Journal of Information Technology*, vol. 7, no. 2, pp. 177-185, 2010, https://www.researchgate.net/publication/220413929

[8] C.M. Vikram and K. Umarani, "Pathological Voice Analysis To Detect Neurological Disorders Using MFCC & SVM", *International Journal of Advanced Electrical and Electronics Engineering*, vol. 2, no. 4, 2013, DOI:10.1109/EITech.2015.7163000

[9] F. Teixeira, J. Fernandes, V. Guedes, A. Junior, and J. P. Teixeira, "Classification of control/pathologic subjects with support vector machines," *Procedia Computer Science*, vol. 138, pp. 272–279, 2018.

[10] F. Amara, " An Improved GMM-SVM System based on Distance Metric for Voice Pathology Detection", *Applied Mathematics & Information Sciences*, vol.10, no. 3, pp. 1061-1070, 2016, DOI:10.1016/j.procs.2018.10.039

[11] Xiang Wang et al., "Discrimination between pathological and normal voices using GMM-SVM approach," *Journal of Voice*, vol. 25, no. 1, 2011, https://doi.org/10.1016/j.jvoice.2009.08.002

[12] S. Kumara , K. Anantha, U. Niranjan, "Study of Harmonics-to-Noise Ratio and Critical-Band Energy Spectrum of Speech as Acoustic Indicators of Laryngeal and Voice Pathology*", EURASIP Journal on Advances in Signal,* 2007, DOI:10.1155/2007/85286

[13] H. Pavol, B. Jesus, H. Alonso, J. Mekyska_, Z. Galaz_, R. Burget, Z. Smekal, "Voice Pathology Detection Using Deep Learning: a Preliminary Study" arxiv, 1907.05905, pp. 1-4, 2019, https://doi.org/10.48550/arXiv.1907.05905

[14] C. P. Tang, K. L. Chui, Y. K. Yu, Z. Zeng, K. H. Wong, "Music Genre classification using a hierarchical Long Short Term Memory (LSTM) model", *International Workshop on Pattern Recognition IWPR*, 2018, DOI:10.1117/12.2501763

[15] V. Gupta, *"*Voice Disorder Detection Using Long Short Term Memory (LSTM) Model*", Arxiv,* 1812.01779, *2018,* https://doi.org/10.48550/arXiv.1812.0177

[16] B. Sabir, F. Rouda, Y. Khazri, B. Touri, and M. Moussetad, "*Improved algorithm for pathological and normal voices identification", International Journal of Electrical and Computer Engineering (IJECE)*, vol. 7, no. 1, pp. 238-243, DOI:10.11591/ijece.v7i1.pp238-243

[17] A. Tharwat, "Classification assessment methods", *Applied Computing and Informatics*, vol. 17 no. 1, pp. 168-192, 2021, 10.1016/j.aci.2018.08.003

Mahraz Kabache received his Diploma of Engineer on electronics from university of Blida, Algeria in 1999 and the Diploma of Magister in automatic speech processing at the University of Bouzaréah, Algeria in 2006. He is currently a PhD candidate in electronics at the Ecole Nationale Polytechnique, Algiers. His research interests on speech and treatment of the pathological signal.

Mhania Guerti is currently a Full Professor and Research Director in the Department of Electronics at Ecole Nationale Polytechnique of Algiers (Algeria). She received her MSc in 1984, from the ILP Algiers in collaboration with the CNET - Lannion (France). She got her PHD from ICP -INPG (Grenoble - France), in 1993. She is specialised in Speech and Language Processing. Professor M. GUERTI has supervised many students in Master and PHD degree. Her current research interests include the areas of Speech Processing, Audiovisual Systems, Acoustics, Biomedical Engineering and Technology and Medical Image Processing.

Breakout Stocks Identification using Machine Learning Approaches

Md. Siam Ansary

Abstract—Stock market offers a platform for people to engage in trading. It contributes to the growth of nation. Decision making regarding investments needs to be done very carefully so that an investor does not suffer massive loss. Since the share market is susceptible to experience huge change at any given moment, with the probability of profit comes huge risks of losing a fortune. In our research, we have worked on prediction of breakout stocks. If identified properly, it can help one to invest efficiently. We have used multiple machine learning approaches as ML models can offer more effective predictions compared to other methods due to the ability to learn and adapt from dataset information. In our experiment, the models have yielded very good results.

***Keywords*—machine learning, breakout stock, stock market, stock.**

NOMENCLATURE

ML	Machine Learning.
AI	Artificial Intelligence.
RFE	Recursive Feature Elimination.
SVM	Support Vector Machine.
SVR	Support Vector Regression.
KNN	K Nearest Neighbor.
RF	Random Forest.
DT	Decision Tree.
MLP	Multilayer Perceptron.
AdaBoost	Adaptive Boosting.
API	Application Programming Interface.

I. INTRODUCTION

Since stock values are always fluctuating, working with stock market data can be exceedingly difficult. Complex circumstances are always present. Predicting the nature of stock prices is rarely simple. While buying and selling stocks, investors and businesses take constant risks, but this is what keeps the economy expanding. The Stock Exchange's dynamic nature aids in the prosperity and economic improvement of a nation. Investing in stocks in the interests of minimizing risk and loss and maximizing gain and profit is a difficult task. Any investment could quickly suffer a significant loss if it is not done correctly.

A breakout stock is one whose price, along by higher volume, varies from a clearly defined support or resistance level. In technical analysis of the stock market, support and resistance are established price levels of a security where it is believed that the price will tend to stop and reverse. Abdullah and Rahaman [1] discussed that based on breakouts, buying and selling decisions should be made. Yu and Li [7] pointed out that the breakout point is a crucial trading point that is more likely to be a high margin opportunity based on the actual experience of human investors.

With enough data, machine learning (ML) approaches may make predictions quite well. When a suitable model is trained on the right data, it may effectively determine if a stock is a breakout candidate or not. The main reason of using ML techniques such as statistical models is that Stock Market is highly volatile and ML can adapt to different scenarios through training better compared to any other method.

The issue regarding investment is that no one wants to suffer any loss. Hence, no decision should be made hastily and all relevant factors should be taken into account. Investments might be quite profitable if a breakout stock can be predicted efficiently. Therefore, we have determined that such a topic requires the use of machine learning techniques to be investigated. Despite reasonable experimentation with other parts of stock markets, we have found that there has been very little work with breakout stocks and there is much scope for progress. Therefore, we have done this work and with classification models, we have achieved satisfactory outcomes.

In the following sections, our research work has been described in details.

II. RELATED WORKS

Researchers have done various experiments with stock market data. In different works, distinct aspects have been focused on.

Ballings et al. [2] used information acquired from publicly traded European companies to forecast the direction of stock prices. The primary goal of their research was to determine which kind of algorithm performed better when comparing single learners and ensemble learners. Logistic Regression, Neural Networks, K Nearest Neighbor, Support Vector Machine, Random Forest, AdaBoost, and Kernel Factory were the methods employed in this study. Random Forest outperformed the other methods. For cross validation, they had employed five times two folds. In this experiment, many financial indicators, including those that measure liquidity, solvency, and profitability, were used as features.

Manuscript received November 4, 2022; December 20, 2022.

Md. Siam Ansary is with the Computer Science and Engineering Department, Ahsanullah University of Science and Technology, Dhaka, BANGLADESH (e-mail: siamansary.aust@gmail.com).

Digital Object Identifier (DOI): 10.53907/enpesj.v2i2.173

Data from the National Stock Exchange of India was used by Naik and Mohan [3] to classify stock price movement. As features, indicators such the Relative Strength Index, Simple Moving Average, Exponential Moving Average, Momentum Indicator, Stochastic Oscillator, Moving Average Convergence Divergence, William R, Accumulation Distribution Index, and Commodity Channel Index were employed.

Using different ML models, Islam et al. [4]. predicted the daily closing price of equities. They used data from the Dhaka Stock Exchange. Support Vector Regression and K Nearest Neighbor Regression are the models that were applied in the experiment. SVR performed better at work. In their best outcome, KNN Regression's R Squared Score was 96.39% and Linear SVR's R Squared Score was 97.04%.

Maheswari and Anbalagan [5] worked using data from the Bombay Stock Exchange to make short-term investing selections. The work has tried with the fuzzy graph technique. The analysis made use of the Simple Moving Average, Exponential Moving Average, Moving Average Convergence Divergence, and Relative Strength Index.

Xu et al. [6] performed research on feature selection for trend prediction of stock trading prices. The fluctuations in stock prices can be due to a variety of variables. Thus, it is crucial to pinpoint the most critical attributes when performing machine learning analysis. Two recursive feature elimination techniques, SVM-RFE and RF-RFE, based on Support Vector Machine and Random Forest, respectively, were utilized in the study. Data from the Shanghai Stock Exchange were utilized for the project. The study concluded that while RF and SVM can both forecast trends effectively, SVM may do so more effectively, and RFE may be unneeded for SVM while it is required for RF.

Breakout points were employed by Yu and Li [7] as crucial trading indicators to locate large margin trading opportunities. They talked about how a breakout happens when the trading volume picks up and a stock price breaks through a predetermined resistance level. After the stock price breaks through resistance, human traders typically take a long position. Volatility tends to rise if a stock trade breaks through a price barrier, and prices often move in the direction of a breakout. Breakouts are significant because they serve as the launching pad for significant price moves in the future and, frequently, major price trends. Typically, channel breakthroughs and price breakthroughs, such as triangles, flags, and heads and shoulders, are what cause the most spectacular price movements.

Wen et al. [8] worked in trading decision support system using Support Vector Machine and Oscillation Box where importance was put on breakout point. They discussed that if the strength of buying or selling beat that of the another, the price will effectively break out the upper bound or the lower bound and the time of the breakout is supposed to be the best time to buy or sell the stock. If the current price effective breaks out the upper bound, it means the price will start an uptrend. The same is true for lower bound breakout.

We have observed that there have been definitely lots of works with stock market and machine learning. But, only in a few of them, the concept of breakout stocks have been utilized and we have not found any work where prediction of breakout stocks have been done. With our research, we have addressed this issue.

III. METHODOLOGY

Stocks can be classified as potential breakout candidates or not using machine learning techniques. Stock data over time are required for this purpose. A stock might be considered a breakout candidate if consolidation happens for it for an extended length of time and its closing value is either higher or lower than the minimum or maximum closing value from the previous two weeks.

A. Dataset Preparation

1—Data Collection: Firstly, stock data has been collected using Yahoo! Finance's API [9]. This collected data has the Open, High, Low, Close, Volume and Adjusted Close values of each of the stocks. Initially, we have collected 5630 samples which are stock data from 01 January 2000 to 20 May 2022.

2— Calculation of New Features: From the Close values of the stocks, for each stocks we have calculated two more features. They are *Maximum Close Value from Last Two Weeks* and *Minimum Close Value from Last Two Weeks*. These two values are considered as Resistance and Support values.

3— Stock Labelling: The highest and lowest closing prices during the previous two weeks for a stock have been identified as characteristics. The occurrence of consolidation is then verified. Consolidation is stated to have taken place if the lowest closing value from the previous two weeks is more than 98% of the highest closing value from the previous two weeks. If consolidation takes place, a stock is considered a breakout candidate if its closing value is either higher or lower than the highest or lowest closing price during the previous two weeks. In this manner, each stock is then classified as either a breakout candidate or not.

4— Balancing the Dataset: It is observed that the number of breakout candidate stocks is less compared to the stocks that are not breakout candidates. Random under-sampling is done to make the dataset balanced. The balanced dataset has 432 samples.

B. Use of Machine Learning Models

1—Feature Scaling: Machine learning classification models can be used to classify stocks as breakout candidates or not after the dataset has been produced. Scaling has been completed on the prepared dataset before applying the classification models. The features can initially be in different ranges, but the scaling procedure puts all the features in the same range. Such a procedure guarantees the absence of any unwarranted bias. Standardization has been used for scaling purpose.

2— Train Test Split: We have divided the dataset into two portions. 80% of the data is used for training the machine learning models and the rest 20% is used for testing purposes. After training the ML models using the 80% of the dataset, we have applied the models on test data and the results are illustrated through the Figures.

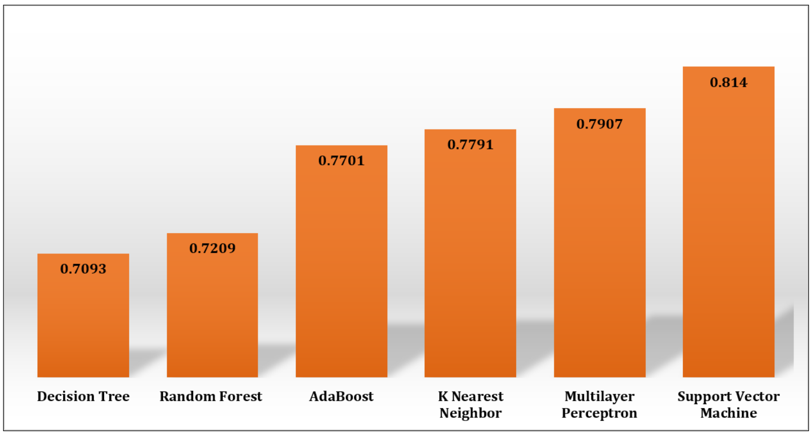

Fig. 1: Accuracy values of the ML Models for Predicting BreakoutStocks

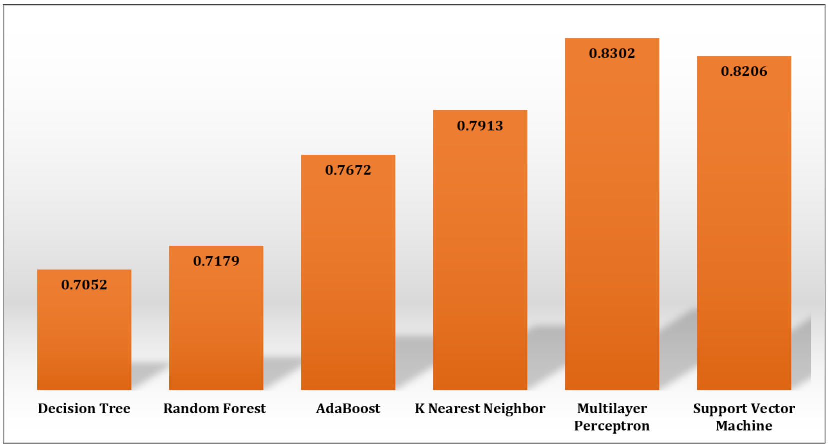

Fig. 2: Precision values of the ML Models for Predicting BreakoutStocks

3— Machine Learning Models: We have used six machine learning models in our work for the classification task. Before applying the models, we have observed the dataset for outliers or null values but prepared dataset had no issues of these kinds. The applied ML models are as the following.

- Decision Tree: A Decision Tree uses a tree-like structure to develop models. It incrementally develops an associated decision tree while segmenting a dataset into smaller and smaller sections. The outcome is a tree containing leaf nodes and decision nodes.

- Random Forest: Random Forest is an ensemble-learning model. The Decision Tree model's shortcomings are sought to be fixed by the Random Forest model. Given that many decision trees are aggregated, the Random Forest technique is far more reliable than the Decision Tree approach.

- Adaptive Boosting: AdaBoost is an ensemble boosting classifier that, by combining weak classifiers, improves their performance. A number of underperforming classifiers are combined through an iterative process to produce a strong classifier with high accuracy. To make effective predictions of unexpected observations, the basic principle is to train the data sample and set the classifier weights in each iteration.

- K Nearest Neighbor: The K Nearest Neighbor is an effective classification technique. KNN maintains all of the examples that are accessible and categorizes additional cases using a similarity metric. A majority vote from its neighbor classes determines the classification of an object (a new instance). The object is grouped into the K closest neighbors' most prevalent class, which is mostly determined by a distance function.

- Multilayer Perceptron: A three-layer feed-forward neural network is called a Multilayer Perceptron. The input layer, hidden layers, and output layer are these three. From input to output, data in an MLP flow in a forward manner. The neurons are trained using back propagation.

- Support Vector Machine: For classification, Support Vector Machine is frequently employed. The algorithm takes data as input and, if possible, creates a line that separates those classes. The technique's goal is to identify the best decision boundary or line for categorization. A hyper-plane is the name given to this optimal choice boundary.

IV. PERFORMANCE ANALYSIS

The performances of the six classification models are illustrated in the figures. The used evaluation metrics are Accuracy, Precision, Recall and F1 Score values of the models.

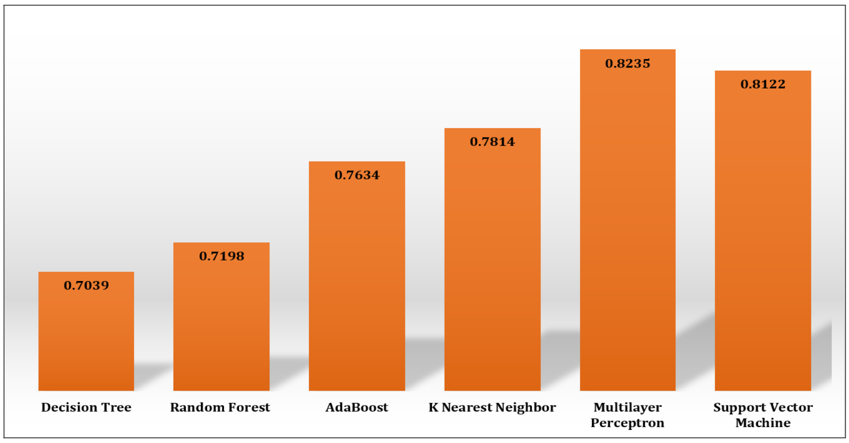

Fig. 3: Recall values of the ML Models for Predicting Breakout Stocks

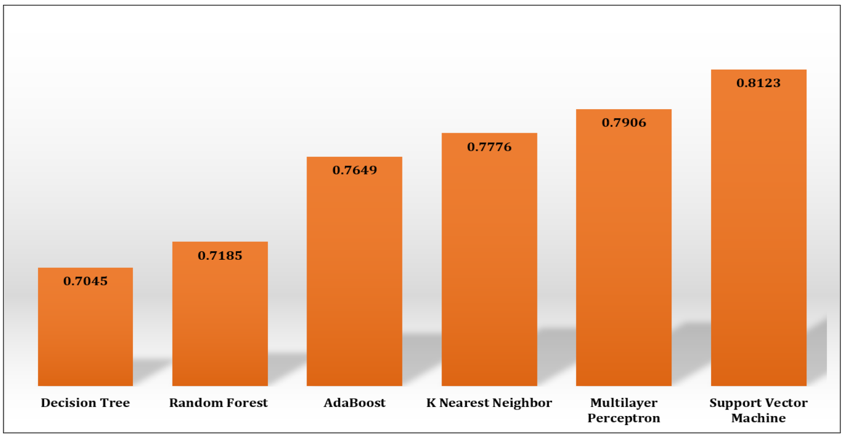

Fig. 4: F1 Scores of the ML Models for Predicting Breakout Stocks

Figure 1 shows the Accuracy values, Figure 2 displays the Precision scores, Figure 3 illustrates the Recall values and Figure 4 represents the F1 Scores of the trained models' performances on the Test portion of the dataset. Among these six models, Decision Tree has had the poorest outcomes while Multilayer Perceptron and Support Vector Machine are the leading ones.

V. CONCLUSION AND FUTURE WORKS

In our work, we have observed that machine learning models can very efficiently identify breakout stocks. Such prediction can help an investor to make wise decisions so that minimal loss and maximum gain can be achieved. Support Vector Machine and Multilayer Perceptron algorithms have shown the most promising results while all the models have achieved satisfactory outcomes. In future, we intend to expand our research and do experiments with more datasets targeting different stock exchanges from various countries and want to work with Deep Learning models.

REFERENCES

[1] Abdullah, Sheikh Shaugat, and Mohammad Saiedur Rahaman. "Stock market prediction model using tpws and association rules mining." In *2012 15th International Conference on Computer and Information Technology (ICCIT)*, pp. 390-395. IEEE, 2012.

[2] Ballings, Michel, Dirk Van den Poel, Nathalie Hespeels, and Ruben Gryp. "Evaluating multiple classifiers for stock price direction prediction." *Expert systems with Applications* 42, no. 20 (2015): 7046-7056. https://doi.org/10.1016/j.eswa.2015.05.013

[3] Naik, Nagaraj, and Biju R. Mohan. "Stock price movements classification using machine and deep learning techniques-the case study of indian stock market." In *International Conference on Engineering Applications of Neural Networks*, pp. 445-452. Springer, Cham, 2019.

[4] Islam, Sharmin, Md Sikder, Md Hossain, and Partha Chakraborty. "Predicting the daily closing price of selected shares on the Dhaka Stock Exchange using machine learning techniques." SN Business Economics 1, no. 4 (2021): 1-16. DOI:10.1007/S43546-021-00065-6

[5] Anbalagan Thirunavukarasu, and S. Uma Maheswari. "Classification and prediction of stock market index based on fuzzy metagraph." *Procedia Computer Science* 47 (2015): 214-221. https://doi.org/10.1016/j.procs.2015.03.200

[6] Xu, Yanru, Zhengui Li, and Linkai Luo. "A study on feature selection for trend prediction of stock trading price." In *2013 International Conference on Computational and Information Sciences*, pp. 579-582. IEEE, 2013.

[7] Yu, Xinpeng, and Dagang Li. "Important trading point prediction using a hybrid convolutional recurrent neural network." *Applied Sciences* 11, no. 9 (2021): 3984. https://doi.org/10.3390/app11093984

[8] Wen, Qinghua, Zehong Yang, Yixu Song, and Peifa Jia. "Intelligent stock trading system based on SVM algorithm and oscillation box prediction." In *2009 International Joint Conference on Neural Networks*, pp. 3341-3347. IEEE, 2009.

[9] "Yahoo! Finance's API", [Online] Available: https:https://pypi.org/project/yfinance/, Last Accessed on 18 September 2022.

Md. Siam Ansary has completed Bachelor of Science (BSc) in Computer Science and Engineering (CSE) from Ahsanullah University of Science and Technology (AUST), Dhaka, BANGLADESH. His undergraduate thesis work was on Extractive Summarization of Newspaper Articles. In the year of 2021, he joined the Department of CSE as a Lecturer. His research interests are on the various fields of Machine Learning and Artificial Intelligence.

An Overview on the Recent Advances of the Voltage Source Converter Control Modes in Terms of their Roles in Transmission Grid Ancillary Services

Rayane MOUROUVIN, Jing DAI, Seddik BACHA, Didier GEORGES and Abdelkrim BENCHAIB

Abstract−Voltage Source Converters (VSC) are expected to be one of the major actors in future AC transmission grids. Their role includes the interconnection of renewable energy, from distributed sources such as residential PV to large Offshore Wind Farms (OWF) using HVDC. With the ongoing decommissioning of traditional power plants with their synchronous generators, VSCs must now bring support functions to the grid. The aim of this paper is to review the different grid services that can be achieved through VSCs and discuss their compatibility with the state-of-the-art VSC controls especially the so-called grid-following and grid-forming controls. After presenting the upcoming issues of future grids and classifying the main VSC controls, this paper deals with the different additional control laws which make it possible to support the AC grid. Some recommendations regarding future grid services classifications and power and energy requirements are given. A comparative table is also proposed to assess the role of the different control modes.

***Keywords*− Ancillary service, grid-following, grid-forming, renewable energy, voltage source converter (VSC).**

NOMENCLATURE

VSC	Voltage Source Converters.
OWF	Offshore Wind Farms.
PSS	Power System Stabilizers.
RoCoF	Rate of Change of Frequency.
SG	Synchronous Generators.
SM	Synchronous Machines.
AVR	Automatic Voltage Regulator.
SCL	Short Circuit Level.
SCR	Short Circuit Ratio.
SCC	Short Circuit Contribution.
PWM	Pulse Width Modulation.
PLL	Phase Locked Loop.
MMC	Modular Multilevel Converters.
FRT	Fault Ride Through.
FFR	Fast Frequency Response.
DSE	Dynamic State Estimation.
POD	Power Oscillation Damping.
ESS	Energy Storage System.
VSM	Virtual Synchronous Machine.

Manuscript received September 29, 2022; revised December 2022.

R. MOUROUVIN and S. BACHA is with the SuperGrid Institute, 69100 Villeurbanne, France, and also with the University Grenoble Alpes CNRS, Grenoble INP, G2Elab, 38000 Grenoble, France (e-mails: rayane.mourouvin@supergrid-institute.com, seddik.bacha@g2elab.grenoble-inp.fr)
J. DAI is with the University Paris-Saclay, CentraleSupélec, CNRS, Laboratoire de Génie Electrique et Electronique de Paris, 91192 Gif sur-Yvette, France, also with the Sorbonne University CNRS, Laboratoire de Génie Electrique et Electronique de Paris, 75252 Paris, France (e-mail: jing.dai@centralesupelec.fr)
D. GEORGES is with the University Grenoble Alpes CNRS, Grenoble INP, GIPSA-lab, 38000 Grenoble, France (e-mail: didier.georges@gipsa-lab.grenoble-inp.fr)
A. BENCHAIB is with the SuperGrid Institute, 69100 Villeurbane, France (e-mail: abdelkrim.benchaib@supergrid-institute.com)

Digital Object Identifier (DOI): 10.53907/enpesj.v2i2.147

I. INTRODUCTION

Power systems now encounter massive changes in terms of generation, transmission and distribution of electricity. In the European Union, the share of renewable energy in electricity generation is expected to rise constantly for the next decades [1], in a worldwide attempt to tackle climate change [2]. In particular, at the transmission-grid level, especially in Europe, many HVDC systems have been built to exchange energy across long distances and interconnect Offshore Wind Farms (OWF) to the mainland [3]. At the distribution-grid level, Power Electronics (PE) converters are used to integrate renewable power sources and new types of loads, such as islanded systems and electric vehicles [4]. These changes will lead to an evolution of the operation of power systems, where PE-interfaced sources and loads will replace a large number of Synchronous Generators (SG) [5].

To ensure stability of such power systems in the future, the PE converters will have to play the roles of traditional SG. This topic has been discussed for years in the scientific community [6] and draws public attention [7]. In particular, the current methods we know to operate and secure the power systems will have to evolve. In order to understand the necessary conditions to operate these PE-dominated grids, we need to analyze the elementary functions that are brought by synchronous generators. Traditionally, the grid stability and reliability is ensured by implicit actions from generators themselves and by specific actions which require additional controls, such as primary frequency support or Power System Stabilizers (PSS) or dedicated equipment such as synchronous condensers or FACTS. In various regions of the world, some of these functions are allocated using ancillary services market [8], [9], [10]. In parallel, with the growing role of PE-based converters, more and more studies now focus on the potential contributions of VSCs to the operation of 100% PE-based grids, such as micro grids [11], offshore networks [12] and HVDC transmission grids [13], [14]. However, these papers only deal with the control options, instead of addressing the needs of the grid. In the last decades, a consistent classification of the power system stability issues has been used as a reference for transmission grid operability and stability [15]. But it is only recently that this classification has been adapted to take into account the increasing role of VSCs in the grid [16], but no classification of the existing control solutions for any of those issues is achieved.

More recently, the impacts of VSC control to provide specific support functions to the common system stability issues was discussed in [17], which only focuses on vector-controlled, also named current-source controlled, VSCs and only briefly mentions the role of grid-forming. On the other hand, some recent studies [18], [19] did compare the role of different grid-forming implementations in multi-machine systems but did not compare them to the most commonly used current-source mode. Indeed, even though there has been some research conducted on classifying those different grid forming controls [20], [21], there is still a missing piece between what can be achieved in terms of ancillary services, i.e. from the grid point-of-view, by the different VSC control modes. In [22], the authors study the evolution of power systems and how it will affect the existing ancillary services. Although it provides insightful review of the implementation of new ancillary services, it does not focus on the control aspects of the VSCs. In [23], the authors present a review of the support functions of VSC for micro grids, but this work is specific to low-voltage systems and do not discuss wide-area issues such as frequency support or power oscillation damping for instance. Some papers proposed a review of specific support functions of VSCs for transmission grids, such as inertia [24], short-circuit contribution for unbalanced faults [25] and power sharing options, both active and reactive, hence integrating grid-forming controls [26]. In addition, more recent reports were published about the role of grid-forming controlled VSCs in grid support functions [27], [4]. However, no comparison is clearly drawn with the most commonly-used current-source controls. In parallel, the role of the grid-forming controlled VSCs in enhancing the PE-based sources penetration limits using modal analysis have been the topic of several studies [28], [29], [30] but these papers are mainly based on simplified systems and it is hard to extract the precise role of each support function when applied to more complex systems. To the authors' best knowledge, there is no review in the literature which focuses on the different VSC control options for the needed support functions from the transmission grid perspective.

In this paper, we gather information about the existing grid services that are currently provided by synchronous machines and that will be needed from the VSCs to ensure a smooth transition to hybrid grids with remaining synchronous units and a high proportion of PE-based converters. The novelty of the paper is to propose a comprehensive comparison of the converter control modes, i.e. Current-source and voltage source modes, not only in terms of converter-level control performances, but also in terms of the potential ancillary services they can provide to the grid.

The paper is organized as follows. In Section 2, we describe the ongoing evolution of power system production and transmission structures and the role of SGs in power system stability. In Section 3, the VSC control modes are introduced and an updated classification is defined for the transmission grid. In Section 4, the role of the VSC in both current-source and voltage-source modes are explored in terms of the grid support functions. Finally, an overview of the differences is drawn in Table 3 and discussed in Section 5.

II. IMPACTS OF THE REPLACEMENT OF SYNCHRONOUS GENERATORS BY POWER ELECTRONICS-BASED STATIONS

The role of the SGs in power systems has been studied for decades [31], [32], and their services to the grid are summarized in this section, in particular, frequency support, reactive power support, contribution to system strength, short circuit contributions and power oscillation damping.

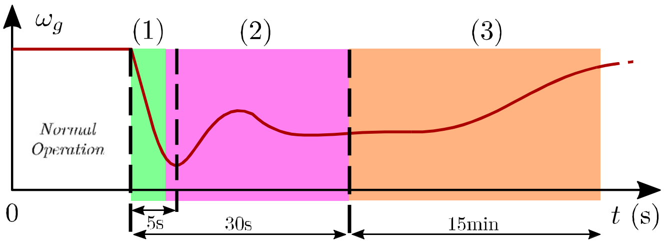

Fig. 1: Different mechanisms with distinctive time scales of the grid frequency when encountering an active power disturbance. (1) Is for inertial response, (2) is for primary frequency control and (3) is for secondary frequency control.

A. *Frequency support*

Traditionally, the grid frequency is mainly supported by the synchronous generators which provide a frequency response following a contingency in the form of an unbalance between the generation and the load. A typical frequency profile of such response is given in Figure 1, where the different mechanisms are highlighted in terms of the time constant:

- Inertial response: The physical law imposes that, in case of a frequency deviation, the SG instantaneously releases the kinetic energy in its rotor, which reduces the Rate of Change of Frequency (Ro Co F).

- Primary frequency control: The speed governor, usually in form of a droop, adjusts the mechanical power from the prime mover in the time scale of 30 seconds, in order to stabilize the frequency.

- Secondary frequency control: The secondary frequency regulator, with a time constant of 15 minutes, adjusts the mechanical power of the synchronous generators of the control area where the disturbance originates, in order to bring back the grid frequency to 50 Hz and restore the power exchange between the control areas.

B. *Reactive power support*

The reactive power support refers to the capacity of a given system to provide some reactive power which is used to maintain the grid voltage. For this, the SG are equipped with an Automatic Voltage Regulator (AVR), which observes the voltage magnitude and adjusts the reactive power accordingly. Indeed the reactive power compensation is used to maintain the grid voltage within acceptable limits. This support is often seen as an ancillary service from the TSO point of view [33]. It can be separated in two types [33], [34] according to the time scales:

- Dynamic support: it refers to the capability to control the bus voltage magnitude following a disturbance. The Belgian TSO Elia defines it as a voltage control that "is activated automatically by the user's production units" [34]. This is provided by the SGs' AVRs for instance;

- Static support: it refers to changes of reactive power references in a given grid in order to support the AC grid voltage at all nodes. This corresponds to a centralized action dictated by the regional TSO. It is triggered “either automatically or manually depending on the situation” [34].

To illustrate the role of reactive power in voltage control, a simple case system is given in Figure 2a. The reactive power received at the bus 1, denoted by QR can be calculated, with phasor assumptions [35], as:

$$Q_R = \frac{V_1}{X}(V_2 \cos\delta - V_1)$$

$$Q_R \approx \frac{V_1}{X}(V_2 - V_1)$$

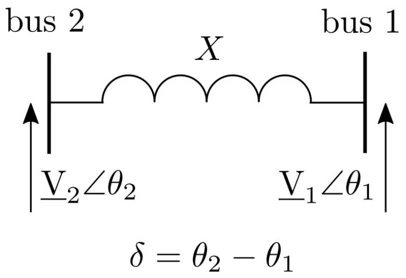

(a) Simplified view of a two-bus system interconnected with a purely inductive line.

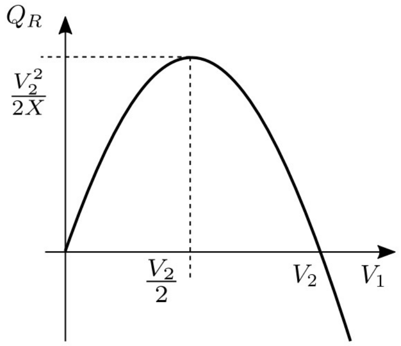

(b) Reactive power evolution around small disturbances (δ = 0).

Fig. 2: Approximation of the reactive power steady-state value depending on the voltage magnitude [35].

Figure 2b gives the evolution of Q_R using (2) and shows the importance of acting on the reactive power to control the AC voltage magnitude. In practice in traditional power systems, the operating points of SGs are determined in power flow studies in order to avoid line congestions and have acceptable voltage magnitude levels [36] but the TSOs also rely on automatic voltage control actions to maintain the bus voltages following unexpected disturbances.

C. System Strength

The system strength, or voltage stiffness, is a metric that quantifies the capability of a given AC bus to maintain the bus voltage around its nominal set point, in terms of both voltage magnitude and phase angle. In its 2016 System Operability Framework [37], the British TSO National Grid gives the following definition in the voltage management section:

“System strength is a regional characteristic which can be expressed as short circuit level (SCL), measured in kA. It provides an indication of the local dynamic performance of the system and behaviors in response to a disturbance.”

With this definition, it is clear that a bus connected to a voltage source, such as an SG, has a stiff voltage since the generator controls its voltage magnitude thanks to its AVR. To quantify the system strength of a grid dominated by SG, the power system community has used for decades the notion of Short-Circuit Level (SCL) or Short-Circuit Ratio (SCR) [38], defined as the amount of fault current that will be injected to the bus in case of a fault normalized with the bus base power. This means that for a given voltage, the higher the SCR is, the closer it is to SGs since the equivalent impedance to the faulty bus is smaller. Nowadays, the system strength is considered as a rising issue because a low value of SCR can create stability problems due to the PE-based source controllers [16].

Although the SCR is a single notion to study the system strength, it actually contains two different power system issues: the system strength at the given bus discussed in this subsection, and the contribution to the short-circuit current, discussed in the next subsection.

D. Short-circuit contributions

The voltage-source behavior of the machine and its large overcurrent capacity make it possible to inject a high short-circuit current in case of a fault, which is essential for the proper operation of the protective relays. The SGs inherently provide a Short-Circuit Contribution (SCC) when a fault occurs. Indeed, during the first instants following the fault, the machine remains connected and injects a fault current which can be as high as 500% of the nominal current [39]. This behavior is illustrated in Figure 3. As shown in this figure, from the point of view of the faulty bus, all the fault currents from the SG and the other AC grid fault currents converge to it. These fault currents are valuable because they are used to detect and locate the fault in the AC grid. Note that, similar to the inertial response, the short-circuit contribution is also a natural behavior of the SG, i.e. No additional control is needed to realize this. However, this feature is based on the voltage-source behavior of the SG which still relies on the AVR performances during the fault.

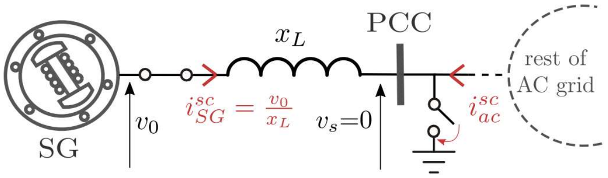

Fig. 3: Grid-connected synchronous generator response when encountering a fault at its point of coupling.

E. Power oscillation damping

Power oscillations refer to low-frequency oscillations, in the range of 0.1 to 1 Hz, which are due to structural limits of the system when certain large-scale disturbances (synchronous generator loss, line tripping, etc.) occur. They are mainly due to the poor damping of low-frequency modes which exist in power systems where the loads and production units are not regularly distributed or where the transmission lines are relatively long [40]. These oscillations must be taken care of because they provoke power oscillations which generate more losses and can cause the tripping of lines. To solve this problem, the Power System Stabilizer (PSS) [35] can be added to the AVR to improve the damping of power oscillations.

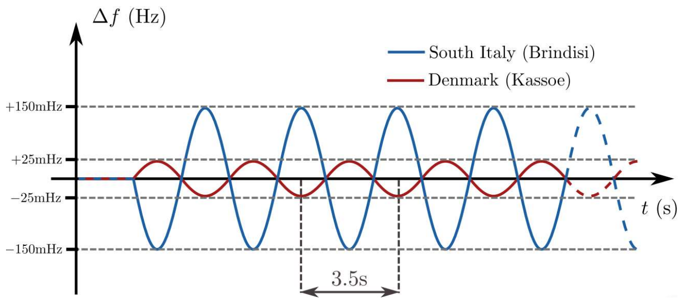

Fig. 4: Illustration of the inter-area oscillation event of the 3rd of Dec. 2017 in the European grid. Based on [41].

However, this problem is still an up-to-date topic because the locations of the SGs equipped with PSSs plays a major role on the damping factor of the whole system. An illustrative case of inter-area oscillations which occurred in Europe in 2017 [41] is given in Figure 4. In this example, 0.3Hz oscillations were noticed by European TSOs in December 2017 between the Northern and Southern parts of Europe. The root cause was not a single large-scale event but rather a sum of different low-risk factors in South Italy.

This event shows the importance of the PSSs allocation, since the disturbance severity can be drastically different depending on the grid node, as described in Figure 4.

F. Consequences of the SG dismantlement on system stability

As synchronous generators are being progressively replaced by PE converters, all the functions described earlier in this section will have to be fulfilled in transitional grids with high proportion of PE and the remaining SGs. This issue is gaining more and more attention from academia [42] and industry [43] across the world.

In 2017, a list main challenges on power system stability were highlighted by European TSOs [43], of which the following items are related to the replacement of SGs by PE-based generation units:

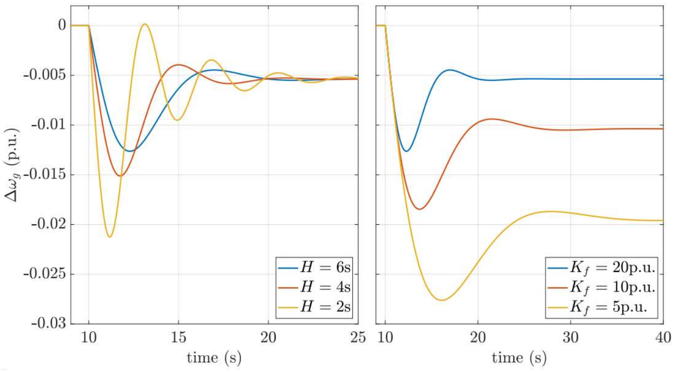

Fig. 5: Effects of decreasing inertia and primary frequency reserves in AC grid frequency ω_g. H is the inertia constant and K_f the primary frequency droop gain. The nominal case (blue line) is H=6s and $K_f = 20p.u.$

1. Decrease of inertia;
2. Reduction of transient stability margins;
3. Wrong participation of PE-based generators in frequency containment;
4. Loss of devices in the context of Fault-Ride-Through (FRT) capability;
5. Lack/excess of reactive power;
6. Voltage dip-induced frequency dip;
7. Introduction of new power oscillations and loss of existing power oscillation dampers (such as PSS of SGs).

Table. I
INERTIA CONTRIBUTIONS OF DIFFERENT COUNTRIES IN EUROPE FOLLOWING ENTSO-E 2030 SCENARIO [4]

Inertia (s)	Countries
H < 2s	Germany, Italy, Ireland, Spain, UK.
2s ≤ H < 3s	Austria, Switzerland.
3s ≤ H < 4s	Finland, France, Norway, Sweden.
H ≥ 4s	Hungary, Poland, Serbia.

Taking the first one for instance, the inertia of most of the European countries is expected to decrease due to the increasing of renewable generation in the electricity mix. The expected equivalent inertia constants of different European countries by 2030 is given in Table 1.

This table shows that countries which would rely on massive renewable sources such as Southern European countries with solar power or Northern Sea countries with wind power, would have a low inertia contribution. On the other hand, Central European countries which still rely on coal-powered plants would have a much higher inertia. Finally, countries that have started to introduce renewables in their electrical systems but still rely on low-carbon power plants, either hydro or nuclear, would be in-between.

In consequence, there is a need to counterbalance the impacts of dismantling current power plants in order to maintain the system operable. In Figure 5, we illustrate the consequences of decreasing inertia and the deployment of primary frequency reserves following an active power load step in the frequency deviation of a two-bus system with one SG and one load. The lack of inertia may cause the tripping of certain components due to an excessive value of RoCoF.

G. Opportunity of the use of power electronics in transmission grids

Even if many challenges arise due to this grid transition, PE-based sources may offer innovative solutions since these interfaces are much more controllable and faster than typical SGs. In addition, as illustrated in Table 2, the integration of renewable energy sources such as OWF, here denoted as wind power plants, the grid-side converter rarely works at its maximum rated power due to wind intermittency mostly. The average active power set point can be derived as follows. The maximum active and reactive power headroom from this average set point are then calculated while assuming the initial reactive power set point is $q^* = 0$:

Table. II
COMPARISON OF THE CHARACTERISTICS OF A SG AND A VSC IN TERMS OF AVAILABLE POWER HEADROOM AND ENERGY FOR SUPPORT FUNCTION PROVISIONS.

Features	Symbol	Wind Power Plant	Thermal Power Plant
Installed capacity, from [44]	S_b	2500 MVA	1000 MVA
Operating hours, from [44]	t_{op}	2000 h	5000 h
Yearly produced energy, from [44]	W_y	5000 GW.h	5000 GW.h
Overcurrent capability, from [45]	i_{max}	110%	500%
Average power set point	p^*_{avg}	0.23 p.u.	0.57 p.u.
Max. active power headroom	P_{hr}	0.77 p.u.	0.43 p.u.
Max. reactive power headroom	Q_{hr}	0.97 p.u.	0.82 p.u.

$$p_{avg}^{*} = \frac{t_{op}}{t_{year}} = \frac{t_{op}(h)}{8670}$$

$$P_{hr} = S_b \times (1 - p_{avg}^{*})$$

$$Q_{hr} = S_b \times \sqrt{1 - {p_{avg}^{*}}^{2}}$$

It appears that the active power at the operating point of the converter is quite low, here assumed to be at $p_{avg}^{*} = 0.23\,p.u.$. In consequence, there would be a lot of power headroom, both active and reactive, available in average, to counterbalance the progressive dismantlement of SGs and the upcoming challenges listed above. This will still require to implement additional control options, which are summarized in Sections 3 and 4.

III. CONVERTER-LEVEL CONTROL MODES

This section presents the existing converter control modes classified into two main categories: current- source mode and voltage-source mode. The state variables we use in the control schemes are based on the equivalent VSC with its LC filter described in Figure 6.

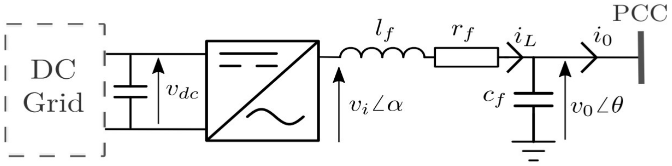

Fig. 6: Equivalent electrical circuit of a Voltage Source Converter (VSC) between its AC and DC interfaces.

A. *Current-source mode*

The current-source control, also known as grid-following or grid-feeding control, is the most commonly used method, where the converter imposes both the active and the reactive power, independent of the grid frequency and voltage. The controller receives the power set points and yields the reference for the current to be injected into the grid. Thus, the converter works as a current source, i.e. the current (and hence the active and reactive power) is controlled while the voltage magnitude and the frequency is free to change. Note that the power reference itself can be varying due to other factors, e.g. the intermittency of renewable energy sources, or an over-layer controller providing some grid service.

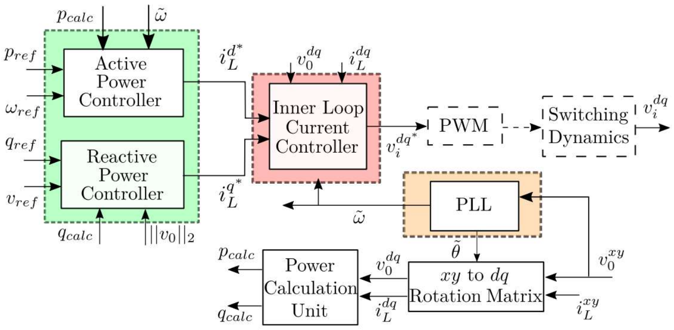

Fig. 7: VSC cascaded structure control scheme in current-source mode.

A classical implementation of the grid-following control is shown in Fig. 7. The voltage at the point of common coupling (PCC) is denoted as v0, while the voltage synthesized by the converter as v_i. A reactor lf is placed between the two voltages. With a properly synthesized v_i, the power exchanged between the converter and the AC grid across the reactor lf follows its reference.

In Figure 7, the current and the voltage in the natural abc frame are transformed in the synchronous dq frame, and a cascaded control is used. The control is composed of four blocks:

- Phase-Locked Loop (PLL): it observes the three phase voltage at the PCC located between the converter and the AC grid, and estimates its angle θ, as illustrated in Figure 8. This information will be used by the other blocks.

- Outer power loop: based on p_{ref} and q_{ref} , the reference values of active and reactive power, the outer power loop calculates the current references, denoted by i_L^{d*} and i_L^{q*}, which are then sent to the inner current loop. By aligning the grid voltage to the d axis, p and q can be decoupled and thus controlled independently. In particular, p depends only on i_L^d while q only on i_L^q. To calculate i_L^{d*} and i_L^{q*} based on p_{ref} and q_{ref} respectively, the control structure in Figure 7 uses a measurement of the PCC voltage to generate the current references, where p_{ref} and q_{ref} are simply divided by the grid voltage to obtain i_L^{d*} and i_L^{q*}. An alternative way to calculate the current references is to use closed-loop control, where PI controllers compare the power references with the measured and filtered power, and then adjusts the current references.

- Inner current loop: based on the current references i_L^{d*} and i_L^{q*} sent by the outer power loop, the inner current loop calculates v_i^{d*} and v_i^{q*}, the desired voltage to be synthesized by the converter, which are then sent to the PWM block. The PI controllers compare the current references with the measured currents, and then adjusts the voltage references. This inner loop is used to control the current flowing through the converter and limit potential over currents. More information about the tuning can be found in [46].

- Pulse-Width Modulation (PWM): based on the v_i^{d*} and v_i^{q*} given by the inner current loop, the PWM generates the gate control signals, which are sent to the switches of the 2-level VSC so that the fundamental component of the obtained voltage is the desire voltage. In case of the other types of VSC, such as Modular Multilevel Converters (MMC), adequate control should be implemented to synthesize the desired voltage [47].

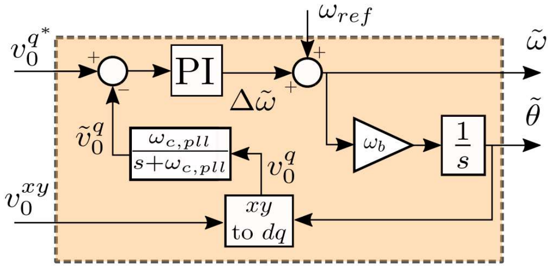

Fig. 8: Detailed control scheme of a classical PLL [48].

The grid-following control is not capable of feeding a passive network, because it always needs a grid voltage to follow, whose frequency and magnitude should be regulated by synchronous machines or converters working in other control modes. When left unregulated, the grid voltage and frequency may deteriorate and result in a voltage collapse, which is unacceptable from the demand-side point of view.

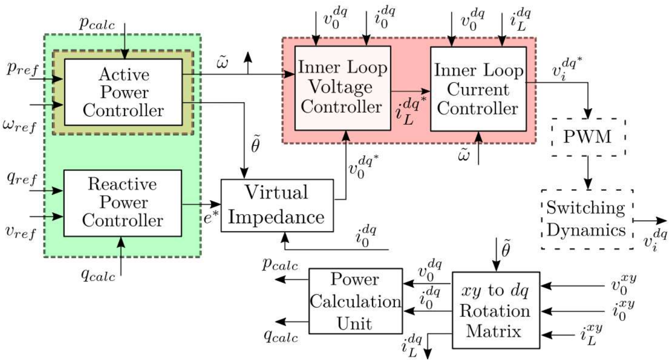

Fig. 9: VSC cascaded structure control scheme in voltage-source mode.

B. *Voltage-source mode*

This control mode, which is also referred to as grid-forming control, has emerged in islanded micro grids first [11]. In this mode, the VSC operates as a voltage source and, in consequence, generates a voltage of desired magnitude and frequency at the connecting bus.

The general scheme is given in Figure 9. The voltage at the PCC, denoted by v_0, is also the voltage of the capacitance c_f. This capacitance can be the physical capacitance of an LC filter [49] or the capacitance of an AC component such as an overhead line [50] if there is no filter. The control scheme is composed of the following blocks:

- Outer power loop: based on the voltage and current measurements at the PCC, the control loop calculates the active and reactive powers which are compared with the references. The control errors of active and reactive power are used to adjust, respectively, its frequency $\tilde{\omega}$ and voltage magnitude e^*. This function reflects the principles of grid-forming which will be detailed in Section 3.C.

- Virtual impedance: when several VSCs are working in voltage-source mode in parallel, this block can be used to eliminate the circulating currents between them. In fact, it changes the voltage reference e^* sent by the outer power loop to emulate an additional impedance between the controlled voltage v_0 and the PCC to generate the voltage reference v_0^{dq*} which is used for the inner control loops, as described in [49].

- Inner control loops: In addition to the inner current, control similar to the one in Section 3. A for the grid-following control, there is also an inner voltage control law that controls v_0^{dq} using PI controllers and generates current references i_L^{d*} and i_L^{q*} for the current controller. More information about the tuning can be found in [51].

- Pulse-Width Modulation (PWM): similar to the one in Section 3.1.

There are in the literature different variants of grid-forming control, which depends on the way the power variations and the voltage references are coupled in the outer power loop. In particular, in Figure 10c, the droop-based grid-forming control [52], [53], [51], [54] couples the active power deviation with that of the VSC estimated frequency $\tilde{\omega}$. The virtual inertia and load sharing of the grid-forming control can be tuned by acting on the low-pass filter cutoff frequency ω_{pq} and the droop gain $m_{p\omega}$ given in Figure 10c.

It is important to note that the vf control, also known as voltage and frequency control [21], which basically imposes a constant voltage magnitude e^*, usually 1 p.u., and a constant frequency $\tilde{\omega} = \omega_{ref}$, usually 50 Hz or 60 Hz, may also be referred to as grid-forming control in micro grid literature [11]. In fact, vf mode can be seen as a particular case of the scheme given in Figure 9 where the outer loops are bypassed and the references are fixed values of e^* and $\tilde{\omega}$.

C. *Classification in the context of transmission grids*

Thanks to the small size of a micro grid, a grid-forming converter is able to impose by itself the frequency to the whole system. However, in the context of a transmission grid, one single converter, which is of much smaller rating than the whole synchronous area, would become incapable of imposing the frequency on its own. Therefore, compared to its original definition in the micro grid where the converter behaves as a voltage source with imposed frequency and voltage magnitude, the grid-forming control in the transmission system is slightly different, and the following classification can be used instead:

- Grid-following: the converter works as a current source that injects power without consideration on the grid conditions.

- Grid-supporting: the converter works as a current source and modulates its power references with respect to the initial load flow conditions to provide voltage, frequency or angle support. In other words, the grid-supporting combines the current-source working mode with an external control modulating the power references. A commonly-used method for controlling the active and reactive powers using a PI control is given in Figures 10a, 10b.

- Grid-forming: the converter works as a voltage source and provides voltage and frequency support. However, the frequency imposed by the converter will not be the nominal frequency, but such that the resulting power and the frequency are coupled to emulate the behavior of SM. The differences between existing grid-forming controls lie in the different control designs of their active and reactive outer power loop and the coupling between them. In addition to the droop-based control given in Figs. 10c 10d, other options exist, such as emulation of Synchronous Machines (SM) [55], [56], [57], [58], [59], [60] and more advanced control-oriented strategies [61], [62]. Besides, some comparisons were drawn between different grid-forming options in micro grids [63] and in transmission grids [64], [65] and showed similar small- signal behaviors and compatible control laws between each other. However, the transient stability analysis showed different behaviors of the grid-forming options [66].

Note that the above classification, borrowed from [11], is somewhat an abuse of language, because the classification criterion is a mixture of the control method and control objective. On the one hand, in terms of the control method, the

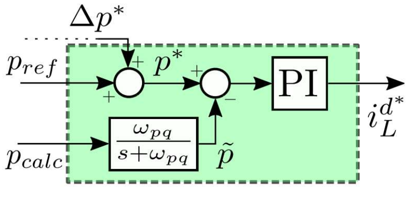

(a) Active power control loop with PI controller in current-source mode

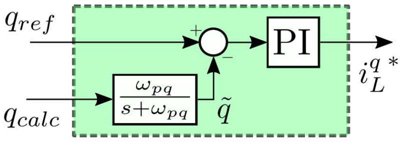

(b) Reactive power control loop with PI controller in current-source mode

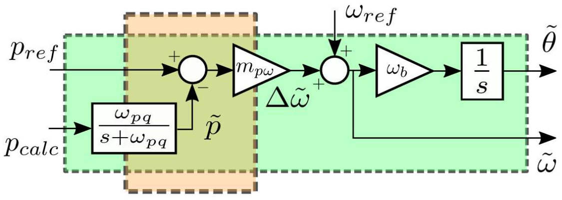

(c) Droop-based active power control loop in voltage-source mode

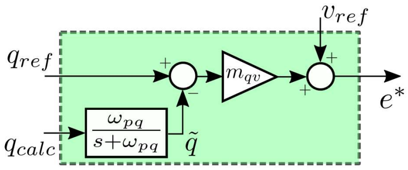

(d) Droop-based reactive power control loop in voltage-source mode

Fig. 10: Examples of the outer power control loops of the VSC in current and voltage source modes respectively.

grid-supporting control resembles the grid-following since both have the converter working as a current source; on the other hand, in terms of the control objective, the grid-support control seems closer to the grid-forming control, since both make the converter to contribute to the voltage and frequency regulation. In other words, to support the frequency, one can either use the grid-supporting control where a Δp^* term is added in the active power controller of the converter working as a current source, as described in Fig. 10a, or alternatively, use the grid-forming control as described in Figure 10c. In addition, the active power controller of the grid-forming scheme from Figure 9 plays a double role as described in Figure 10c. Indeed, it provides a PLL-free synchronizing unit [52] and makes the VSC contribute to frequency support as SGs do, i.e. by providing both synthetic inertia and primary frequency response [49].

In terms of performances, grid-following control is designed to ensure a good power tracking of the power references p_{ref} and q_{ref} using a dedicated controller as in Figures 10a, 10b. However, the behavior of the VSC relies on strong grid assumptions, i.e. with a high SCR and the VSC can even become unstable if connected to a weak grid (SCR<3). On the other hand, the grid-forming control has a power tracking capability thanks to its power controller shown in Figures 10c, 10d but since it behaves as a voltage source, its AC power response depends on the SCR. However, it is capable of working in weak grid conditions as well, on the contrary to grid-following controlled VSCs. These conclusions are shown in Fig. 11 where simulations were carried out using a simple benchmark containing a VSC model based on Figure 6 which is connected to an infinite bus through a transformer and a line modeled with a dynamic phasor model.

IV. GRID-LEVEL CONTROL MODES

With the current-source and voltage-source modes described at the converter level in Section 3, this section presents their services from a grid point of view.

A. *Frequency support*

Contrary to SGs whose frequency response is a combination of the physical behavior and explicit control, the VSC output power is entirely decoupled from the grid frequency behavior in grid-following mode. However, there are different active power profiles that can be provided by the VSC to support the grid frequency:

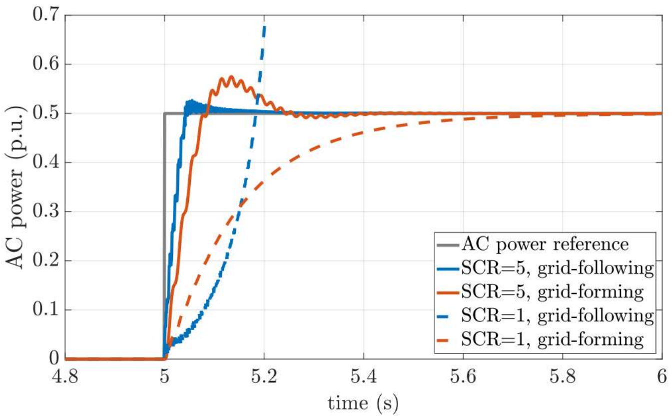

Fig. 11: Influence of the SCR on the performances of the VSC in terms of power tracking, following a 0.5 p.u. step of pref . The test-case is based on [67] with PLL gains taken from [68].

- Active power / frequency droop: developed in [69], [70], [71], [72], its aim is to provide an active power response that is proportional to the measured frequency deviation as described in Figure 12a. This control scheme is inspired by the primary frequency control of traditional SGs given in Fig. 1. In consequence, the VSC takes part in the load sharing with the SGs.

- Virtual inertia: as in [73], [74], with this control, almost instantaneously after the disturbance, the converter changes the active power reference proportionally to the RoCoF in order to emulate the kinetic energy delivered by the SG's rotor. It is known as the inertial response, and is illustrated in Figure 12b. It is important to note that the implementation of a derivative term $\frac{d\Delta\omega}{dt}$ would require an additional notch filter in practical conditions.

- Fast Frequency Response (FFR): this type of response has started to spread in islanded transmission grids [22] and provides an active power contribution deployed with a latency of less than 1s [75], [76], [77]. In consequence, it can be seen as a trade-off between the inertial response and the primary frequency control, and the power profile of the FFR can be customized instead of following a certain pattern, as illustrated in Figure 12c.

As to a grid-forming converter, it provides inherent frequency support since it emulates the SG dynamic response, i.e. with virtual inertia and load sharing capability. Concerning this last item, the current-source controlled and voltage-source controlled VSCs provide similar responses if sized and tuned accordingly [78]. However, if the DC-side of the converter is not adapted to provide this load sharing capability, this contribution may not be desired. This inherent frequency droop action of the grid-forming controller can thus be cancelled by using a high-pass filter or a frequency estimation $\tilde{\omega}$ from a PLL [79] instead of the nominal frequency ω_{ref} in the active power control loop given in Figure 10c. Another option is to replace the droop gain $m_{p\omega}$ by an IP controller [80].

About the inertia then, since the grid-forming controlled VSC is operated as a SG during the first instants following any kind of disturbances, it does provide some inertia to the grid. On the other hand, the inertia provided by the virtual inertia controller in current source mode from Fig. 12b is slightly different because it is an extra control loop that relies on the PLL speed, accuracy and the notch filter to deliver such inertia, meaning it will not be delivered at the very first instants following the disturbance.

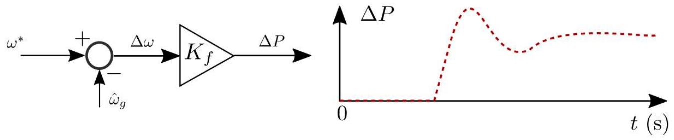

(a) Active power / frequency droop response

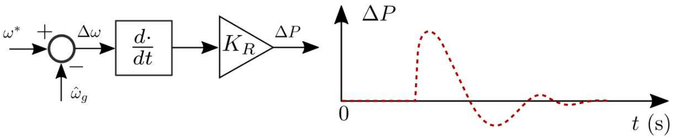

(b) Virtual inertia response

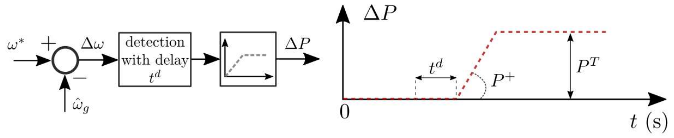

(c) Fast Frequency Response (FFR)

Fig. 12: Illustration of different potential supporting actions using a variation of power reference provided by a power converter.

B. *Reactive Power Support*

PE-based systems have been used for decades to provide AC voltage / reactive power support. One of the most famous examples are STATCOM systems [81], which are also based on VSC technology. Indeed, by controlling the reactive current of a converter, whether it is an HVDC grid, a FACTS or a system connected to an energy source, the VSC is capable of adjusting its reactive power to support the PCC voltage as described in Section 2.2. In the literature, there are different ways the VSC can control its reactive power to support the AC voltage. In addition to the reactive power loop from Figure 10b, there are other options which are given in Figure 13. In Figure 13a, another implementation of the reactive power loop is proposed to control the PCC bus voltage using PI control. In Figure 13b, the support is a power droop similar to the active power frequency droop in Figure 12a, which is used to provide a support proportional to the voltage magnitude deviation. In Figure 13c, the controller regulates the voltage magnitude at the PCC but the reference is changed dynamically with respects to the reactive power deviation. However, the two implementations from Figures 13a, 13c can be a problem if multiple VSCs with this type of control are connected to the same bus because the PI controllers will compete against each other, creating undesired oscillations.

For the grid-forming control, the behavior of the VSC is based on controlling the PCC voltage magnitude as shown earlier in Fig. 10d. However, as for the options given in Figures 13a, 13c, there is a problem if multiple converters are connected in parallel at the same bus. In practice, this is one of the advantages of implementing a virtual impedance as in Figure 9. Also, it is important to note that the grid-forming control is not only about maintaining the AC voltage magnitude but also its phase, as it is described in the next section.

C. *Contribution to system strength*

In the literature, it has been shown that PE-based converters controlled in current-source mode can be unstable when connected to a weak grid, i.e. where the SCR at the PCC is inferior to 3, due to the interactions between the line dynamics and the PLL [83]. To illustrate these interactions, a frequency analysis of the open-loop PLL given in Figure 8 is performed for different PLL gains. The analysis is carried out considering $k^{\alpha}_{p,pll} = \alpha . k_{p,pll}$ and $k^{\alpha}_{i,pll} = \alpha . k_{i,pll}$ for different values of α = {1, 2, 3... 20}, where $k_{p,pll} = -0.05\ p.u.$, $k_{i,pll} = -2.53\ p.u.$ and $\omega_{c,pll} = 200 rad/sec$, based on values from [68].

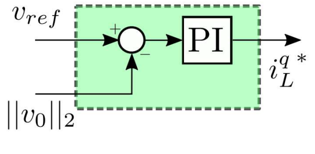

(a) AC voltage magnitude control [82].

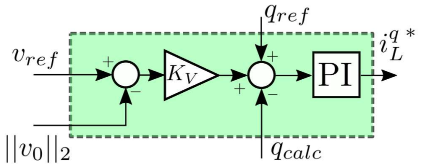

(b) AC voltage droop control [11].

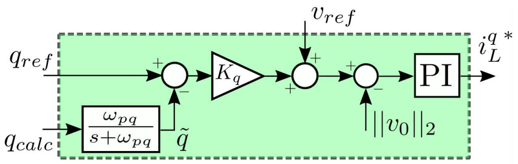

(c) AC voltage magnitude control with reactive power droop [72].

Fig. 13: Different implementations of AC voltage support using reactive power modulation in current-source mode.

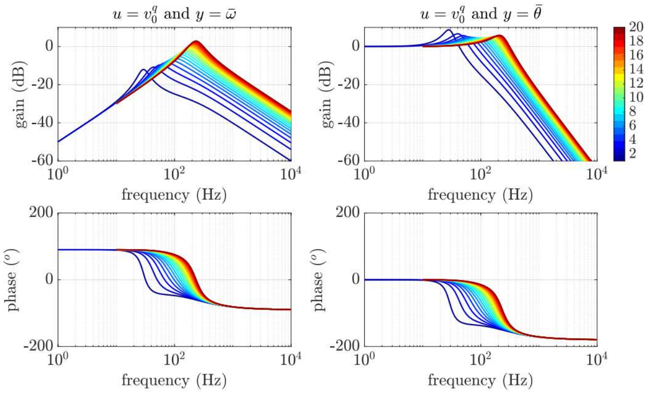

Fig. 14: Bode plots of the linearized PLL for different values of gain $k^{\alpha}_{p,pll}$ and $k^{\alpha}_{i,pll}$ with respect to the two outputs $\overline{\omega}$ (left-side) and $\overline{\theta}$ (right-side).

As shown in the Bode plots given in Figure 14, there is a trade-off between the speed of the tracking capability of the PLL and its robustness: if the PLL is fast enough to track any frequency changes, it is also more sensitive to disturbances. The resonance frequency of the PLL is found to be around 100 Hz, which is the order of magnitude of the transmission line dynamics [29], hence the negative interactions with the lines causing instability when the lines are too long, which correspond to weak grid conditions.

Nowadays, this weak grid issue is responsible for renewable energy curtailments in some power systems [84]. In the literature, there are three main solutions to allow more VSCs to be connected to weak grids:

- Introduce synchronous condensers to provide system strength to the weak regions [85]. However, this solution does not include any VSC-related function;
- Reinforce the weak grids, for example by grid-forming control in Figure 9. This is different from the services by FACTS that improve the long-term voltage stability by reactive power compensation [15]. However, it is possible to control STATCOMs using grid-forming control [86] to make them contribute to the system strength;

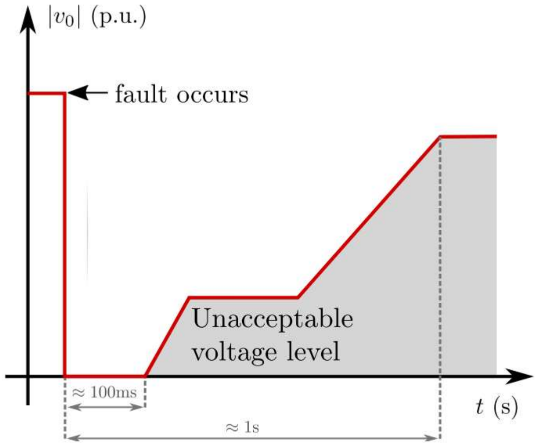

(a) Typical Low Voltage Fault-Ride-Through (LVFRT) profile imposed by a grid operator.

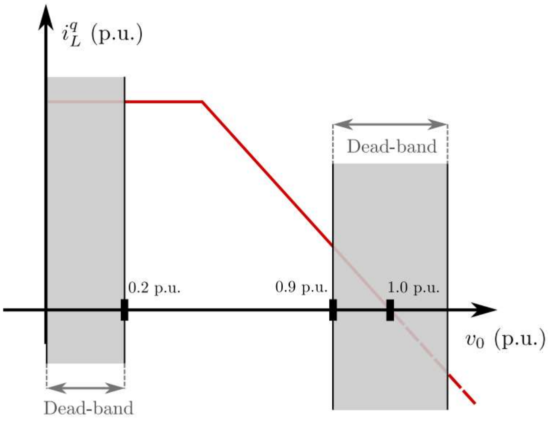

(b) Reactive fault current requirements depending on the voltage level. Based on [39] and [90].

Fig. 15: Synthesis of the expected voltage and current responses of a VSC following an AC-side fault.

- Develop novel PLL algorithms for weak and very weak grids, i.e. with a SCR ≤ 2 [68], [87] and keep the current-source control structure presented in Figure 7. Today, this current-source control has better performances than classical voltage-source controls in terms of power tracking for strong grid situations [88], [67], as illustrated in Figure 11. Therefore, the VSC owners and TSOs should reach an agreement on whether most, if not all, of the VSC should participate to some extent in this voltage control, as the SG used to do, or only some specific VSC should be required to ensure minimum service in this aspect.

Even though the notion of SCR was a consistent metric for short-circuit contributions and voltage stiffness in SG-based systems, it is not sufficient enough in PE-dominated systems since the fault-transient behavior and the system strength in normal operation are no longer coupled. Developing novel metrics to assess the system strength levels in PE-dominated grids is still an open-topic. Indeed, contrary to SGs, a VSC in grid forming does not maintain its voltage-source behavior at all time because of its limited overcurrent capability. Indeed, its contribution to the voltage stiffness strongly depends on the nature of the disturbance and its operating point, in particular its active and reactive power references. In that way, dynamic analysis are required to assess the voltage stiffness of a PE-dominated grid, while it was possible for SG-dominated grids to use only static analysis [85].

D. Short-circuit contributions

Unlike SGs whose high overcurrent capability makes it possible to contribute to short-circuits during AC faults, as described in Section 2.4, VSCs are highly sensitive to over currents due to their semiconductor devices. If no current limit is imposed, the conversion valves will be blocked and the VSC will be disconnected from the grid, hence interrupting its power conversion and making it unable to contribute to the short-circuit currents.

In consequence, we may require in the future that VSCs have a Fault-Ride through (FRT) capability where they remain connected when encountering large disturbances, such as a fault or a generation unit loss. The FRT capability is usually assessed by TSOs using a FRT profile which corresponds to the minimum voltage response of the equipment following a given fault to remain connected to the grid. There are many profiles which depend on the TSO grid codes [89]. A typical FRT is given in Fig. 15a. In addition to the voltage deviations, the VSC can still lose synchronism even though the voltage magnitude remains within the FRT profile. This transient stability needs to be assessed and is currently a topic of great concern by academia [90, 91].

Second, in addition to remaining connected, the VSC may also be asked to contribute to the short- circuit currents in order to help detecting the fault. In the literature, there have been some studies about developing strategies to make the VSCs in current-source mode remain connected and provide 1 p.u. of reactive current when the voltage drops below a certain level [92], [93], 90% of nominal voltage in [90]. However, in several grid codes, these contributions are not mandatory anymore if the PCC voltage, v0 in Fig. 15b, drops below 20% of its nominal value [39] as it is illustrated in Fig. 15b.

In the voltage-source mode, as in Figure 9, the FRT capability is more complex to achieve, because the branch current results directly from the voltage the VSC imposes at its terminal. In consequence, the VSC control must act quickly to avoid a fault current which would damage the conversion devices or force the interruption [45]. In the recent literature, two main ways of achieving FRT with a VSC controlled in voltage-source mode have emerged:

- Use of a backup PLL: When the control detects a current rise, it switches to an emergency current- source mode and keeps the synchronization through a backup PLL. The new power references are chosen in order to inject a fault current of 1 p.u. [52].
- Limitation of the voltage magnitude: The control keeps running in voltage source mode but the voltage reference is decreased to limit the branch current. One solution could be the implementation of a fault detector with a virtual

impedance control as in [94], [95].

For both the current-source mode and the voltage-source mode, the short-circuit contribution of a VSC is physically limited by the semiconductor devices. In consequence, the current way the TSOs detect and clear AC faults has to be re-defined for large penetration of PE-based sources scenario [45]. There are two tendencies that have emerged in the literature for AC fault detection:

- Enhance the fault response of PE-based sources: According to this conservative strategy based on the assumption that power grids will still rely on SGs, the fault detection algorithms are unlikely to change. On the other hand, the very limited overcurrent capability of VSCs, currently at approximately 110% as shown in Table 2, must be enhanced. One solution is to upgrade the thermal management system of the converter. There are examples in the literature of PE-based systems where the current is able to go up to 200% for less than 200µs [92]. Another solution is to integrate synchronous condensers in parallel with the VSC to enhance the fault response at the point of coupling [96].

- Change the AC grid fault detection strategy: Today the AC fault detection algorithm is based on differential functions, relying only on measurements of currents and Kirshoff's current law. However, with the recent advances in system identifications, new methods based on Dynamic State Estimation (DSE) make it possible to monitor a given protection zone without requiring large over currents or coordination between the zones [97].

However, the choice of relevant solutions requires the coordination of the different actors (TSOs, converter manufacturers, etc.) and is more a design problem rather than a control problem.

E. Power oscillation damping

Following the development of several embedded HVDC links in some interconnected systems, several studies have shown that VSC-interfaced power sources and VSC-HVDC links operating in current-source mode can provide a Power Oscillation Damping (POD) function if the active power reference are adjusted accordingly [98], [99], [100], and [101]. These power references can be changed according to the difference of the two-area frequencies $\Delta p^* = f(\omega_2 - \omega_1)$ or the difference between the reference and the local frequency $\Delta p^* = f(\omega^* - \omega_2)$ for instance, as illustrated in Figure 17a.

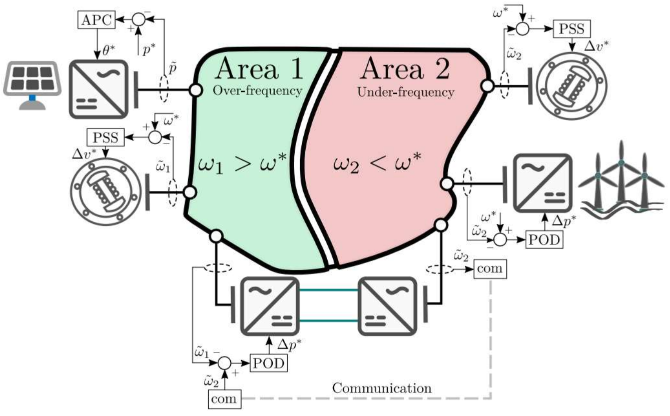

Fig. 16: Different manners of damping inter-area power oscillations in a single synchronized power system using synchronous generators, VSC-interfaced power sources and VSC-HVDC links.

In the former case, the system needs communication devices whereas the latter option only relies on local measurements. Both cases are illustrated in Figure 16. The POD function can also be achieved using reactive power reference modulation [102] or be applied to Multi-terminal HVDC (MTDC) embedded systems [103].

For grid-forming VSCs, also given in Fig. 16, since they have a SG-like behavior, they add supplementary electromechanical-like modes in the system. However, these modes can still be damped by adding an additional damping controller though. In this case, to damp the power oscillations, the power references p_{ref} and q_{ref}, defined in Figure 9, can be adjusted similar to a VSC working in current-source mode. In this way, the power-tracking capability of the grid-forming mode [67] is used to provide POD. Another option is to adapt the active power control loop to add a notch filter which eliminates the undesirable oscillations, as in [104, 105] and illustrated in Figure 17b.

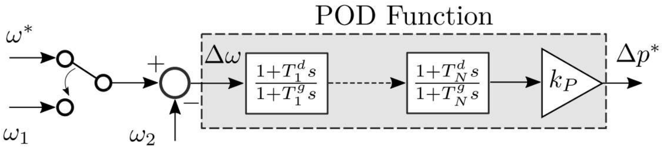

(a) POD control structure using active power modulation [100].

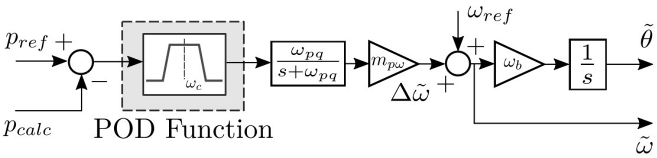

(b) POD control structure using modified droop-based grid-forming control [104].

Fig. 17: Options for POD functions depending on the VSC control mode.

Nevertheless, all these types of POD impose some constraints on the VSC:

- Some power headroom must be dedicated to POD at all time to be capable of acting on the power references. In consequence, the VSC cannot operate at its maximum apparent power.

- It impacts the transferred power of the VSC, which can generate market-related and operational issues if the HVDC system is between two distinct areas/countries.

V. DISCUSSIONS & CONCLUSIONS

The two VSC control modes, namely, the current-source control and the voltage-source control, were presented in Section 3, while the converter services to the grid were discussed in Section 4. As described in this last section, most of the grid support functions can be added to the grid-following scheme by slightly modifying the control, i.e. by adding current limitations or $\Delta p^*/\Delta q^*$ power references. As a consequence, the supporting action can be tuned accordingly to the available reserves from the DC side. On the other hand, voltage-source mode can provide most of the grid services since it is capable of emulating SG behavior. However, because of its voltage source behavior, the extracted power is a consequence of the imposed volt- age. Thus, it requires a large energy source to provide functions such as frequency support, system strength contribution or POD. The short-circuit contribution is however limited by the semiconductor device over- currents. Traditional SGs can provide the short circuit current thanks to their large over current capability, as shown in Section 2. These functions are included in the definition of grid-forming in some references [27] though, which can be misleading from a control point of view. To be properly integrated in the grid, the VSC control must consider the energy management algorithms of the power sources on the DC side that deliver this supplementary energy, which could be brought directly in DC or through another AC/DC converter. This extra energy can be provided by deloading PV arrays [75], wind power plants [106, 107, 108] or by storing it in an Energy Storage System (ESS) through Li/ion batteries [78, 109] or supercapacitors [110]. On the other hand, it is possible to control a VSC in grid-forming even though there is no dedicated storage unit, as for HVDC links interfacing two AC grids [111] or interconnecting offshore wind farms [112]. As a summary, the compatibility of the two control modes with the grid services is given in Table 3, where frequency support is split into virtual inertia and load sharing capability to highlight this.

This distinction between the different objectives of a grid-forming controlled VSC are an up-to-date topic. In [113], several categories of "grid-forming" were drawn such as:

- grid-forming: refers to VSCs controlled as constant voltage sources, which is equivalent to the vf control described in Section 3.2;
- synchronous grid-forming: refers to VSCs in grid-forming which are capable of synchronizing with other parallel-connected voltage sources (grid-forming VSCs, SGs or SCs);
- Virtual Synchronous Machine (VSM): refers to synchronous grid-forming VSCs which are capable of providing power from an extra source of energy and a short-circuit current during faults.

In this classification, grid-forming and synchronous grid-forming refer to control aspects: the VSC is seen as a voltage source from the grid perspective and the outer loop control inputs are a voltage magnitude and angle, as in Fig. 9. On the other hand, Virtual Synchronous Machine refers to the grid aspects because it includes some of the support functions described in Section 2. This terminology is compatible with Table 3 and shows the need to distinguish in the "grid-forming" related literature the control aspects which makes it possible to have a PLL-free synchronization from the grid aspects which replaces the functions of the SGs with VSCs. This understanding makes us realize that some inherent functions of SGs, such as inertia, whose shortage in future power systems was considered as the worst issue for European TSOs in 2017 [43], are less important than others, such as system strength reinforcement. In fact, it is clear now that weak grids is a significant challenge right now for islanded power systems such as Texas [84] or Australia [114] where weak grid issues were recently reported. In conclusion, the desired behavior of VSCs in the future might not be to emulate SGs but could be less restrictive since those PE-based sources are much more controllable.

The contributions of this article can be listed as follows:

- A comprehensive introduction to the upcoming challenges of AC transmission grids due to the increasing amount of renewables and the ongoing dismantlement of synchronous generators;
- An overview of the main VSC control modes and a front-

Table. III

COMPATIBILITY OF THE TWO MAIN VSC CONTROL MODES WITH THE DIFFERENT GRID SUPPORT FUNCTIONS

	Current-source mode		Voltage-source mode (Grid forming)	
	Grid-Following	Grid-Supporting	with extra energy.	w/o extra energy.
Converter-level				
synchronization	Uses an external PLL to capture the grid frequency and phase angle.		Observes the variations of active power to estimate the grid frequency and phase angle. The converter and the grid are naturally coupled by the synchronizing torque.	
power-tracking	Relies on strong grid assumptions. Quite good performances in power tracking when these conditions are met. See Fig. 11.		Not as good as current-source mode for power tracking in terms of both time response and static error [88],[67]	
current-limiting action	Current limiters can be implemented in the current controller.		No inherent current controller at first place. But cascaded structure with current controller is now widely used [51],[49].	
Grid-level				
virtual inertia	No. The VSC tracks power references.	Possible with virtual inertia control as in Fig. 12b. Not as well adapted as grid forming option [74].	Yes, due to the dynamics of the Low-Pass Filter (LPF) in the active power controller shown in Fig. 10c.	Yes, due to the LPF dynamics. Support is however limited by the quantity of available DC power.
load sharing capability	No. The VSC tracks power references.	Possible with active power / frequency droop control as in Figure 12a.	Yes, as shown in [51], [64].	Impossible if there is no dedicated storage system [112].
reactive power support	No. The VSC tracks power references.	Possible with the supporting actions described in Fig. 13	Yes, the VSC controls the PCC voltage magnitude and adjusts its reactive power accordingly as long as it respects its overcurrent limitations.	
system strength contribution	Impossible. The VSC is operated as a current-source and the PCC voltage is seen as an external disturbance.		Yes. The VSC is operated as a voltage source and the PCC voltage magnitude and phase angle are seen as control variables [11].	
short-circuit contribution	Can be implemented as in [25]. The contribution is limited by the thermal limits [45].		FRT must be taken care of because of the voltage source behavior. See [52] or [94], [95] for control options.	
power oscillation damping	No. The VSC tracks power references.	Possible using active or reactive power reference modulation as described in Fig. 17a. See [98], [99],[100], and [101].	Inherent damping based on SG emulation but can disturb the system as well. Compatible with SG's PSS.	POD actions can be added as in Figs. 17a ([98],[99], [100], [101]) - 17b ([104]). Needs some available energy for active power damping.

to-front comparison of the current-source and voltage-source modes, respectively the grid-following and grid-forming controls;

- A presentation of the main ancillary services that used to be realized by SGs and how the two types of VSC control modes can be adjusted and modified to provide some of these functions to the grid.

In future work, it should be primordial to investigate the compatibility of all the controllers with each other and how to dispatch the different control modes within a given grid.

Acknowledgments

This work is supported by the French Government under the program Investissements d'Avenir (ANEITE-002-01).

REFERENCES

[1] European Commission, EU Reference Scenario 2016 - Energy, transport and GHG emissions Trends to 2050, institutional website (Jul. 2016). https://ec.europa.eu/energy

[2] United Nations, Adoption of the Paris Agreement (2015). https://unfccc.int/process-and-meetings/the-paris-agreement/the-paris-agreement

[3] J. Glasdam, J. Hjerrild, L. H. Kocewiak, C. L. Bak, Review on multi-level voltage source converter based HVDC technologies for grid connection of large offshore wind farms, in: 2012 IEEE International Conference on Power System Technology (POWERCON), IEEE, 2012.

[4] ENTSO-E, High Penetration of Power Electronic Interfaced Power Sources and the Potential Contribution of Grid Forming Converters, Technical Report, ENTSO-E, Brussels, BE (2020).

[5] I. Oleinikova, E. Hillberg, micro vs mega: trends influencing the development of the power system, ISGAN (2020).

[6] B. Kroposki, Can smarter solar inverters save the grid?, IEEE Spectrum (Oct. 2016). https://spectrum.ieee.org/energy/renewables/can-smarter-solar-inverters-save-the-grid

[7] J. Ambrose, Solar farms can keep UK's lights on even at night, The Guardian (Nov. 2019). https://www.theguardian.com/environment/2019/nov/24/solar-farms-keep-uk-lights-on-at-night

[8] Y. G. Rebours, D. S. Kirschen, M. Trotignon, S. Rossignol, A survey of frequency and voltage control ancillary services—part i: Technical features, IEEE Transactions on Power Systems 22 (1) (2007) 350–357.

[9] Y. G. Rebours, D. S. Kirschen, M. Trotignon, S. Rossignol, A survey of frequency and voltage control ancillary services—part II: Economic features, IEEE Transactions on Power Systems 22 (1) (2007) 358–366. DOI: 10.1109/TPWRS.2006.888963

[10] P. Pinson, Ancillary services and regulation markets, in: Lecture at DTU, DTU, Technical University of Denmark - Center for Electric Power and Energy, 2018.

[11] J. Rocabert, A. Luna, F. Blaabjerg, P. Rodriguez, Control of power converters in AC micro grids, IEEE Transactions on Power Electronics 27 (11) (2012) 4734–4749.

[12] R. Ramachandran, S. Poullain, A. Benchaib, S. Bacha, B. Francois, AC grid forming by coordinated control of offshore wind farm connected to diode rectifier based HVDC link - review and assessment of solutions, in: 2018 20th European Conference on Power Electronics and Applications (EPE'18 ECCE Europe), IEEE, 2018.

[13] M. Yu, A. Dysko, C. D. Booth, A. J. Roscoe, J. Zhu, A review of control methods for providing frequency response in VSC-HVDC transmission systems, in: 2014 49th International Universities Power Engineering Conference (UPEC), IEEE, 2014.

[14] B. Luscan, S. Bacha, A. Benchaib, A. Bertinato, L. Chedot, J. Gonzalez-Torres, S. Poullain, M. Romero-Rodriguez, K. Shinoda, A vision of HVDC key role towards fault-tolerant and stable AC/DC grids, IEEE Journal of Emerging and Selected Topics in Power Electronics (2020). DOI: 10.1109/JESTPE.2020.3037016

[15] IEEE and CIGRE, Definition and Classification of Power System Stability IEEE/CIGRE Joint Task Force on Stability Terms and Definitions, IEEE Transactions on Power Systems 19 (3) (2004) 1387–1401. DOI: 10.1109/TPWRS.2004.825981

[16] Power System Dynamic Performance Committee Task Force on Stability definitions and characterization of dynamic behavior in systems with high penetration of power electronic interfaced technologies, Stability definitions and characterization of dynamic behavior in systems with high penetration of power electronic interfaced technologies, Technical Report 77, IEEE Power & Energy Society (Apr. 2020).

[17] Q. Peng, Q. Jiang, Y. Yang, T. Liu, H. Wang, F. Blaabjerg, On the stability of power electronics-dominated systems: Challenges and potential solutions, IEEE Transactions on Industry Applications 55 (6) (2019) 7657–7670. DOI: 10.1109/TIA.2019.2936788

[18] A. Tayyebi, D. Gross, A. Anta, F. Kupzog, F. Dorfler, Frequency Stability of Synchronous Machines and Grid-Forming Power Converters, IEEE Journal of Emerging and Selected Topics in Power Electronics 8 (2) (2020) 1004–1018. DOI: 10.1109/JESTPE.2020.2966524

[19] A. Crivellaro, A. Tayyebi, C. Gavriluta, D. Gross, A. Anta, F. Kupzog, F. Dorfler, beyond low-inertia systems: Massive integration of grid-forming power converters in transmission grids, in: 2020 IEEE Power & Energy Society General Meeting (PESGM), IEEE, Montreal, QC, Canada, 2020.

[20] P. Unruh, M. Nuschke, P. Strauß, F. Welck, Overview on Grid-Forming Inverter Control Methods, Energies 13 (10) (2020) 2589.

[21] K. M. Cheema, A comprehensive review of virtual synchronous generator (2020) 10.

[22] B. Hartmann, I. Vokony, I. Taczi, Effects of decreasing synchronous inertia on power system dynamics—overview of recent experiences and marketization of services, International Transactions on Electrical Energy Systems 29 (12) (Dec. 2019).

[23] X. Zhao, L. Chang, R. Shao, K. Spence, Power system support functions provided by smart inverters—a review, CPSS Transactions on Power Electronics and Applications 3 (1) (2018) 25–35.

[24] J. Fang, H. Li, Y. Tang, F. Blaabjerg, On the Inertia of Future More-Electronics Power Systems, IEEE Journal of Emerging and Selected Topics in Power Electronics 7 (4) (2019) 2130–2146.

[25] J. Jia, G. Yang, A. H. Nielsen, A review on grid-connected converter control for short-circuit power provision under grid unbalanced faults, IEEE Transactions on Power Delivery 33 (2) (2018) 649–661.

[26] Y. Han, H. Li, P. Shen, E. A. A. Coelho, J. M. Guerrero, Review of active and reactive power sharing strategies in hierarchical controlled micro grids, IEEE Transactions on Power Electronics 32 (3) (2017) 2427–2451. DOI: 10.1109/TPEL.2016.2569597

[27] T. Jouini, U. Markovic, D. Groß, New options for existing system services and needs for new system services (Dec. 2018).

[28] M. M. Siraj Khan, Y. Lin, B. Johnson, M. Sinha, S. Dhople, Stability Assessment of a System Comprising a Single Machine and a Virtual Oscillator Controlled Inverter with Scalable Ratings, in: IECON 2018 - 44th Annual Conference of the IEEE Industrial Electronics Society, IEEE, D.C., DC, USA, 2018, pp. 4057–4062.

[29] U. Markovic, O. Stanojev, E. Vrettos, P. Aristidou, G. Hug, Understanding stability of low-inertia systems, arXiv (2019).

[30] R. Mourouvin, J. C. Gonzalez-Torres, J. Dai, A. Benchaib, D. Georges, S. Bacha, Understanding the role of VSC control strategies in the limits of power electronics integration in AC grids using modal analysis, Electric Power Systems Research (2020) 106930.

[31] P. Kundur, Power System Stability and Control, Electric Power Research Institute Edition, 1, McGraw-Hill, 1994.

[32] X.-F. Wang, Y.-H. Song, M. Irving, Modern Power Systems Analysis, Springer, 2008.

[33] K. L. Anaya, M. G. Pollitt, Reactive Power Management and Procurement Mechanisms: Lessons for the Power Potential Project, Technical Report, National Grid ESO (2018).

[34] Elia, Overview of ancillary services for the power grid, Review report, Belgian High Voltage Grid Operator, Brussels, BE (Jan. 2008).

[35] J. Machowski, J. W. Bialek, J. R. Bumby, Power System Dynamics, wiley Edition, Chichesgter, West Sussex, UK, 2008.

[36] N. Xu, C. Yu, F. Wen, Valuation of reactive power support services based on sensitivity and risk analysis, Electric Power Systems Research 77 (5-6) (2007) 646–651. doi:10.1016/j.epsr.2006.06.004. URL https://linkinghub.elsevier.com/retrieve/pii/S0378779606001350

[37] National Grid, 2016 System Operability Framework, SOF, National Grid ESO, Warwick, UK (2016).

[38] NERC, Short-circuit modeling and system strength (Feb. 2018).

[39] Joint Working Group C4/C6.35, Modelling of inverter-based Generation For Power System Dynamic Studies, CI- GRE/CIRED, 2018.

[40] C. Liu, R. Yokoyama, K. Koyanagi, K. Y. Lee, PSS design for damping of inter-area power oscillations by coherency-based equivalent model, International Journal of Electrical Power & Energy Systems 26 (7) (2004) 535–544.

[41] ENTSO-E, Oscillation Event 03.12.2017, Tech. rep., ENTSO-E, Brussels, BE (Mar. 2018).

[42] F. Milano, F. D¨orfler, G. Hug, D. J. Hill, G. Verbic, Foundations and challenges of low-inertia systems (invited paper), in: Power Systems Computation Conference (PSCC), 2018.

[43] MIGRATE, Deliverable 1.1: Current and arising issues caused by increasing power electronics penetration (May 2017).

[44] J. Li, C. Liu, P. Zhang, Y. Wang, J. Rong, Difference between grid connections of large-scale wind power and conventional synchronous generation, Global Energy Interconnection 3 (5) (2020) 486–493.

[45] M.-S. Debry, G. Denis, T. Prevost, F. Xavier, A. Menze, Maximizing the penetration of inverter-based generation on large transmission systems: the MIGRATE project, in: 6th Solar Integration Workshop, 2016.

[46] S. Akkari, Control of a multi-terminal HVDC (MTDC) system and study of the interactions between the MTDC and the AC grids., PhD dissertation, University Paris Saclay (Oct. 2016).

[47] A. Zama, A. Benchaib, S. Bacha, D. Frey, S. Silvant, D. Georges, Linear feedback Dead-Beat Control for Modular Multilevel Converters: Validation under Faults Grid Operation mode, IEEE Transactions on Industrial Electronics (2020).

[48] Y. Lin, B. Johnson, V. Gevorgian, V. Purba, S. Dhople, Stability assessment of a system comprising a single machine and inverter with scalable ratings, in: 2017 North American Power Symposium (NAPS), IEEE, Morgantown, WV, 2017, pp. 1–6.

[49] U. Markovic, J. Vorwerk, P. Aristidou, G. Hug, Stability Analysis of Converter Control Modes in Low-Inertia Power Systems, in: 2018 IEEE PES Innovative Smart Grid Technologies Conference Europe (ISGT-Europe), IEEE, Sarajevo, Bosnia and Herzegovina, 2018.

[50] E. Sanchez-Sanchez, E. Prieto-Araujo, O. Gomis-Bellmunt, The role of the internal energy in MMCs operating in grid- forming mode, IEEE Journal of Emerging and Selected Topics in Power Electronics (2020).

[51] G. Denis, From grid-following to grid-forming: The new strategy to build 100 % power-electronics interfaced transmission system with enhanced transient behavior, PhD dissertation, Ecole Centrale Lille (Nov. 2017).

[52] L. Zhang, L. Harnefors, H.-P. Nee, Power-synchronization control of grid-connected voltage-source converters, IEEE Transactions on Power Systems 25 (2) (2010) 809–820.

[53] J. W. Simpson-Porco, F. D¨orfler, F. Bullo, Synchronization and power sharing for droop-controlled inverters in islanded microgrids, Automatica 49 (9) (2013) 2603–2611.

[54] T. Qoria, F. Gruson, F. Colas, G. Denis, T. Prevost, X. Guillaud, Inertia effect and load sharing capability of grid forming converters connected to a transmission grid, in: 15th IET International Conference on AC and DC Power Transmission (ACDC 2019), Institution of Engineering and Technology, 2019.

[55] Q.-C. Zhong, G. Weiss, Synchronverters: Inverters that mimic synchronous generators, IEEE Transactions on Industrial Electronics 58 (4) (2011) 1259–1267. DOI: 10.1109/TIE.2010.2048839

[56] S. D'Arco, J. A. Suul, O. B. Fosso, Control system tuning and stability analysis of virtual synchronous machines, in: 2013 IEEE Energy Conversion Congress and Exposition, IEEE, 2013, pp. 2664–2671.

[57] M. Guan, W. Pan, J. Zhang, Q. Hao, J. Cheng, X. Zheng, Synchronous generator emulation control strategy for voltage source converter (VSC) stations, IEEE Transactions on Power Systems 30 (6) (2015) 3093–3101.

[58] Q. Cossart, F. Colas, X. Kestelyn, Model reduction of converters for the analysis of 100% power electronics transmission systems, in: 2018 IEEE International Conference on Industrial Technology (ICIT), IEEE, 2018, pp. 1254–1259. DOI: 10.1109/ICIT.2018.8352358

[59] J. Roldan-Perez, A. Gonzalez-Cajigas, A. Rodriguez-Cabero, M. Prodanovic, P. Zumel, Design and analysis of a current- controlled virtual synchronous machine for weak grids, in: 2019 IEEE Applied Power Electronics Conference and Expo- sition (APEC), IEEE, 2019, pp. 1459–1465. DOI: 10.1109/APEC.2019.8722044

[60] U. Markovic, Z. Chu, P. Aristidou, G. Hug-Glanzmann, LQR-based adaptive virtual synchronous machine for power systems with high inverter penetration, IEEE Transactions on Sustainable Energy 10 (3) (2019) 1501–1512. DOI: 10.1109/TSTE.2018.2887147

[61] D. Groß, M. Colombino, J.-S. Brouillon, F. Dorfler, The effect of transmission-line dynamics on grid-forming dispatchable virtual oscillator control, IEEE Transactions on Control of Network Systems 6 (3) (2018) 1148–1160. DOI: 10.1109/TCNS.2019.2921347

[62] C. Arghir, T. Jouini, F. D¨orfler, Grid-forming control for power converters based on matching of synchronous machines, Automatica 95 (2018) 273–282. https://doi.org/10.1016/j.automatica.2018.05.037

[63] B. Johnson, M. Rodriguez, M. Sinha, S. Dhople, Comparison of virtual oscillator and droop control, in: 2017 IEEE 18th Workshop on Control and Modeling for Power Electronics (COMPEL), IEEE, Stanford, CA, USA, 2017, pp. 1–6. DOI: 10.1109/COMPEL.2017.8013298

[64] R. Ofir, U. Markovic, P. Aristidou, G. Hug, Droop vs. Virtual inertia: Comparison from the perspective of converter operation mode, in: 2018 IEEE International Energy Conference (ENERGYCON), IEEE, 2018, pp. 1–6. DOI: 10.1109/ENERGYCON.2018.8398752

[65] A. Tayyebi, D. Groß, A. Anta, F. Kupzog, F. Dorfler, Interactions of grid-forming power converters and synchronous machines – a comparative study, arXiv (2019).

[66] H. Yu, M. A. Awal, H. Tu, I. Husain, S. Lukic, Comparative Transient Stability Assessment of Droop and Dispatchable Virtual Oscillator Controlled Grid-Connected Inverters, IEEE Transactions on Power Electronics 36 (2) (2021) 2119–2130.

[67] E. Rokrok, T. Qoria, A. Bruyere, B. Francois, X. Guillaud, Classification and dynamic assessment of droop-based grid-forming control schemes: Application in HVDC systems, Electric Power Systems Research 189 (Dec. 2020).

[68] M. Molinas, J. Suul, S. D'Arco, P. Rodriguez, Extended stability range of weak grids with voltage source converters through impedance-conditioned grid synchronization, in: 11th IET International Conference on AC and DC Power Transmission, Institution of Engineering and Technology, 2015.

[69] S. Akkari, M. Petit, J. Dai, X. Guillaud, Interaction between the voltage-droop and the frequency-droop control for multi-terminal HVDC systems, in: 11th IET International Conference on AC and DC Power Transmission, IET, 2015. DOI: 10.1049/cp.2015.0036

[70] C. Collados-Rodriguez, M. Cheah-Mane, E. Prieto-Araujo, O. Gomis-Bellmunt, Stability analysis of systems with high VSC penetration: Where is the limit?, IEEE Transactions on Power Delivery (Dec. 2019).

[71] J. Fradley, R. Preece, M. Barnes, Adaptive fast frequency response for power electronic connected energy sources, in: 2019 IEEE Milan PowerTech, IEEE, 2019. DOI: 10.1109/PTC.2019.8810597

[72] G. S. Misyris, J. Mermet-Guyennet, S. Chatzivasileiadis, T. Weckesser, Grid Supporting VSCs in Power Systems with Varying Inertia and Short-Circuit Capacity, in: 2019 IEEE PES Power Tech, IEEE, Milano, Italy, 2019. DOI: 10.1109/PTC.2019.8810979

[73] D. Duckwitz, B. Fischer, Modeling and design of df/dt-based inertia control for power converters, IEEE Journal of Emerging and Selected Topics in Power Electronics 5 (4) (2017) 1553–1564.

[74] B. K. Poolla, D. Gros, F. Dorfler, Placement and implementation of grid-forming and grid-following virtual inertia and fast frequency response, IEEE Transactions on Power Systems 34 (4) (2019) 3035–3046.

[75] C. Rahmann, A. Castillo, Fast frequency response capability of photovoltaic power plants: The necessity of new grid requirements and definitions, Energies 7 (10) (2014) 6306–6322.

[76] Q. Hong, M. Nedd, S. Norris, I. Abdulhadi, M. Karimi, V. Terzija, B. Marshall, K. Bell, C. Booth, Fast frequency response for effective frequency control in power systems with low inertia, The Journal of Engineering (16) (2019) 1696–1702.

[77] National Grid ESO, Enhanced frequency response FAQs (Mar. 2016).

[78] Y. Zuo, M. Paolone, F. Sossan, Effect of voltage source converters with electrochemical storage systems on dynamics of reduced-inertia bulk power grids, in: Power Systems Computation Conference (PSCC), IEEE, 2020.

[79] E. Rokrok, T. Qoria, A. Bruyere, B. Francois, X. Guillaud, Effect of using PLL-based grid-forming control on active power dynamics under various SCR, in: IECON 2019 - 45th Annual Conference of the IEEE Industrial Electronics Society, IEEE, 2019, pp. 4799–4804.

[80] A. Narula, M. Bongiorno, M. Beza, J. R. Svensson, X. Guillaud, L. Harnefors, Impact of steady-state grid-frequency deviations on the performance of grid-forming converter control strategies, in: 2020 22nd European Conference on Power Electronics and Applications (EPE'20 ECCE Europe), IEEE, Lyon, France, 2020.

[81] ENTSO-E, Static Synchronous Compensation (STATCOM). URL https://www.entsoe.eu/Technopedia/techsheets/static-synchronous-compensation-statcom

[82] S. Kovacevic, D. Jovcic, S. S. Aphale, P. Rault, O. Despouys, Analysis of potential low frequency resonance between a 1GW MMC HVDC and a nearby nuclear generator, Electric Power Systems Research 187 (2020) 106491.

[83] J. Z. Zhou, H. Ding, S. Fan, Y. Zhang, A. M. Gole, Impact of Short-Circuit Ratio and Phase-Locked-Loop Parameters on the Small-Signal Behavior of a VSC-HVDC Converter, IEEE Transactions on Power Delivery 29 (5) (2014) 2287–2296.

[84] J. Matevosyan, Experience in Texas with declining inertia, in: IEA - Technical secure integration of large shares of converter based power sources, ERCOT, Paris, France, 2020.

[85] E. Marrazi, G. Yang, P. Weinreich-Jensen, Allocation of synchronous condensers for restoration of system short-circuit power, Journal of Modern Power Systems and Clean Energy 6 (1) (2018) 17–26.

[86] Phi-Long Nguyen, Q.-C. Zhong, F. Blaabjerg, J. M. Guerrero, Synchronverter-based operation of STATCOM to mimic synchronous condensers, in: 2012 7th IEEE Conference on Industrial Electronics and Applications (ICIEA), IEEE, 2012, pp. 942–947.

[87] A. A. A. Radwan, Y. A.-R. I. Mohamed, Improved vector control strategy for current-source converters connected to very weak grids, IEEE Transactions on Power Systems 31 (4) (2016) 3238–3248.

[88] L. Harnefors, F. M. M. Rahman, M. Hinkkanen, M. Routimo, Reference-feedforward power-synchronization control, IEEE Transactions on Power Electronics (2020).

[89] L. D´ıez-Maroto, L. Rouco, F. Fernandez-Bernal, Fault ride through capability of round rotor synchronous generators: Review, analysis and discussion of European grid code requirements, Electric Power Systems Research (2016) 10.

[90] M. G. Taul, X. Wang, P. Davari, F. Blaabjerg, An Overview of Assessment Methods for Synchronization Stability of Grid-Connected Converters Under Severe Symmetrical Grid Faults, IEEE Transactions on Power Electronics 34 (10) (2019) 9655–9670.

[91] X. Wang, M. G. Taul, H. Wu, Y. Liao, F. Blaabjerg, L. Harnefors, Grid-Synchronization Stability of Converter-Based Resources An Overview, IEEE Open Journal of Industry Applications (2020).[92] J. Keller, B. Kroposki, Understanding Fault Characteristics of Inverter-Based Distributed Energy Resources, nrel Edition, 2010.

[93] J. Jia, G. Yang, A. H. Nielsen, E. Muljadi, P. Weinreich-Jensen, V. Gevorgian, Synchronous condenser allocation for improving system short circuit ratio, in: 2018 5th International Conference on Electric Power and Energy Conversion Systems (EPECS), IEEE, 2018, pp. 1–5.

[94] G. Denis, T. Prevost, M.-S. Debry, F. Xavier, X. Guillaud, A. Menze, the Migrate project: the challenges of operating a transmission grid with only inverter-based generation. A grid-forming control improvement with transient current-limiting control, IET Renewable Power Generation 12 (5) (2018) 523–529. https://doi.org/10.1049/iet-rpg.2017.0369

[95] T. Qoria, F. Gruson, F. Colas, G. Denis, T. Prevost, X. Guillaud, Critical clearing time determination and enhancement of grid-forming converters embedding virtual impedance as current limitation algorithm, IEEE Journal of Emerging and Selected Topics in Power Electronics (2019).

[96] H. Biellmann, M. Buquet, P. Chay, A. Schwery, V. Costan, J. Drommi, G. Prime, The benefits of implementing Syn- chronous Compensators in grids with high penetration of Renewables, in: 2020 CIGRE Session, CIGRE, Paris, 2020.

[97] M. Paolone, A. Monti, T. Gaunt, T. Van Cutsem, X. Guillaud, V. Vittal, M. Liserre, C. Vournas, S. Meliopoulos, Fundamentals of Power Systems Modelling in the Presence of Converter-Interfaced Generation, in: 2020 Power Systems Computation Conference (PSCC), IEEE, Porto, Portugal, 2020, p. 35.

[98] R. Eriksson, Coordinated control of multiterminal DC grid power injections for improved rotor-angle stability based on lyapunov theory, IEEE Transactions on Power Delivery 29 (4) (2014) 1789–1797.

[99] J. Renedo, A. Garcia-Cerrada, L. Rouco, Active power control strategies for transient stability enhancement of AC/DC grids with VSC-HVDC multi-terminal systems, IEEE Transactions on Power ystems 31 (6) (2016) 4595–4604. DOI: 10.1109/TPWRS.2016.2517215

[100] O. Kotb, M. Ghandhari, J. Renedo, L. Rouco, R. Eriksson, On the design and placement of a supplementary damping controller in an embedded VSC-MTDC network, in: 2017 IEEE PES Innovative Smart Grid Technologies Conference Europe (ISGT-Europe), IEEE, 2017.

[101] J. C. Gonzalez-Torres, G. Damm, V. Costan, A. Benchaib, F. Lamnabhi-Lagarrigue, Transient stability of power systems with embedded VSC-HVDC links: stability margins analysis and control, IET Generation, Transmission & Distribution 14 (17) (2020) 3377–3388.

[102] J. Renedo, L. Rouco, A. Garc´ıa-Cerrada, L. Sigrist, A communication-free reactive-power control strategy in VSC-HVDC multi-terminal systems to improve transient stability, Electric Power Systems Research 174 (Sep. 2019).

[103] J. C. Gonzalez-Torres, G. Damm, V. Costan, A. Benchaib, F. Lamnabhi-Lagarrigue, A novel distributed supplementary control of multi-terminal vsc-hvdc grids for rotor angle stability enhancement of ac/dc systems, IEEE Transactions on Power Systems (2020).

[104] P. Rodriguez Cortes, J. I. Candela Garcia, J. Rocabert Delgado, R. Teodorescu, Virtual Controller of Electromechanical Characteristics for Static Power Converters (2012).

[105] G. N. Baltas, N. B. Lai, L. Marin, A. Tarraso, P. Rodriguez, Grid-Forming Power Converters Tuned through Artificial Intelligence to Damp Subsynchronous Interactions in Electrical Grids, IEEE Access (2020). DOI: 10.1109/ACCESS.2020.2995298

[106] H. A. Pereira, V. F. Mendes, L. Harnefors, R. Teodorescu, Comparison of 2l-VSC and MMC-based HVDC converters: Grid frequency support considering reduced wind power plants models, Electric Power Components and Systems 45 (18) (2017) 2007–2016.

[107] H. T. Nguyen, G. Yang, A. H. Nielsen, P. H. Jensen, Combination of synchronous condenser and synthetic inertia for frequency stability enhancement in low inertia systems, IEEE Transactions on Sustainable Energy (2018). DOI: 10.1109/TSTE.2018.2856938

[108] C. R. Shapiro, J. Meyers, C. Meneveau, D. F. Gayme, Wind farms providing secondary frequency regulation: evaluating the performance of model-based receding horizon control, Wind Energy Science 3 (1) (2018) 11–24. DOI: 10.1088/1742-6596/753/5/052012

[109] U. Markovic, V. Haberle, D. Shchetinin, G. Hug, D. Callaway, E. Vrettos, Optimal sizing and tuning of storage capacity for fast frequency control in low-inertia systems, in: 2019 International Conference on Smart Energy Systems and Technologies (SEST), IEEE, 2019.

[110] F. Errigo, P. Venet, L. Chedot, A. Sari, Optimal supercapacitor pack sizing for modular multilevel converter with integrated energy storage system, in: 2018 IEEE International Conference on Industrial Technology (ICIT), IEEE, Lyon, 2018, pp. 1760–1766.

[111] L. Zhang, L. Harnefors, H.-P. Nee, Interconnection of two very weak AC systems by VSC-HVDC links using power- synchronization control, IEEE Transactions on Power Systems 26 (1) 344–355.

[112] R. Mourouvin, K. Shinoda, J. Dai, A. Benchaib, S. Bacha, D. Georges, AC/DC Dynamic Interactions of MMC-HVDC in Grid-Forming for Wind-Farm Integration in AC Systems, in: 2020 22nd European Conference on Power Electronics and Applications (EPE'20 ECCE Europe), IEEE, Lyon, France, 2020. DOI: 10.23919/EPE20ECCEEurope43536.2020.9215668

[113] J. Gleadow, G. Love, H. Saad, T. Rauhaia, C. Barker, A. Canelhas, M. Barnes, G. Denis, S. Bartlett, E. Prieto-Araujo, X. Chen, S. Iftekharul, V. Pathirana, K. Schonleber, J. Rittinger, K. Koreman, J. Paquin, J. Sakamuri, AC fault response options for VSC HVDC converters, CIGRE Science & Engineering 15 (2019) 105 – 110.

[114] N. Modi, B. Badrzadeh, A. Halley, A. Louis, A. Jalali, Operational manifestation of low system strength conditions – Australian experience, in: 2020 CIGRE, C2, CIGRE, Paris, France, 2020, p. 11.

Rayane Mourouvin obtained the M.Eng degree from Ecole Centrale Lyon, Ecully, France and and the M.Sc degree in Electrical Engineering from jointly Ecole Centrale Lyon and Claude Bernard University in Lyon, France, both in 2018. He pursued his PhD studies at SuperGrid Institute and University of Grenoble Alpes, France, where he obtained the Ph.D degree in 2021. He is now working at Aalto University, Espoo, Finland as a postdoctoral researcher. His main research interests include control applications for grid-connected converters, power system modelling and stability analysis.

Jing Dai received his Master's degree in Power Engineering from Supelec, France in 2007 and the University of Paris-Sud in 2008. He earned the Ph.D. degree from Supelec in 2011. Since 2013, he is an assistant professor at CentrleSupelec, France. Since 2014, he is partially seconded to join SuperGrid Institute. His research is on the control of high voltage direct current (HVDC) systems.

Seddik Bacha was born in Ighram, Algeria in 1958. He received the Engineering and Magister degrees from the National Polytechnic School of Algiers, in 1982 and 1990. He joined the Grenoble Electrical Engineering Laboratory (G2Elab) and received the PhD and HDR degrees in 1993 and 1998, respectively. He served as Assistant Professor during six years in Algeria at the National Polytechnic School of Algiers and University of Bejaïa-Bgayet. In 2013 he has been appointed Assistant Professor at Grenoble University and got Full Professor position in 1998. He has been leading the power System Group inside G2Elab during more than 10 years ; He served as deputy director of the GDR SEEDS. He is currently Program Scientific Director and Scientific Council Chairman at the SuperGrid Institute of Energy Transition (France). His research interests are based on the modelling and control of electrical energy processes: Renewable energy systems, Intelligent buildings, V2G, microgrids and HVDC super grids.

Didier Georges was born in Epinal, France in 1961. He received the Engineering degree from ESIEE Paris, France in 1984, the Docteur-Ingénieur degree in automatic control and applied mathematics from Mines ParisTech, France, in 1987, and the Habilitation à Diriger des Recherches degree from the Institut National Polytechnique de Grenoble, France, in 1997.He is a full Professor at Grenoble INP, Ecole Nationale Supérieure de l'Energie, de l'eau et de l'Environnement, Grenoble, France and GIPSA-lab. He is mainly interested in closed-loop nonlinear optimal control (predictive control, numerical solutions), modelling, estimation and control of complex systems governed by partial differential equations or systems in networks, with applications to environmental and power systems. From January 2018 to December 2021, he was in charge of the Cross-Disciplinary Project RISK@Univ. Grenoble Alpes dedicated to Assessment and Management of

Risk, gathering 100 researchers belonging to 15 research labs in Grenoble and funded by IDEX Université de Grenoble (Initiative of Excellence). From November 2018 to December 2021, he was researcher at SuperGrid Institute Villeurbanne. Since July 2022, he has been scientific co-director of national research program IRIMa (Integrated Risk Management) funded by the French program of investments for the future (PIA4). Didier Georges has published more than 190 communications in books, journals, or international conferences, in the field of automatic control and its applications.

Abdelkrim Benchaib received his Ph.D. from the Automatic Systems Laboratory, Picardie University, France, in December 1998 and in 2014 his HDR (French postdoctoral degree allowing its holder to supervise PhD students) from Paris-Orsay University. He joined Alstom in July 2000 where he has been working as a power quality and smart grid project leader and thereafter with GE Grid solutions. Currently, he is seconded by GE to work with the SuperGrid institute where he is a Sub-program group leader for real-time strategies of super grids AC/DC control and dispatch. His expertise and research interests include automatic control, AC and DC power systems and power electronics. He is an associate Professor at the Cnam (Conservatoire National des Arts et Metiers) teaching wind energy and power network. He has been General Chairman of the EPE ECCE Europe Conference for its 2020 edition (EPE conference is one of the bigest events in the world for Power Electronics with up to 1000 participants).

Beneficiation of Oolitic Iron Ore Sourced from Gara Djebilet using Coal-Based Direct Reduction prior to Magnetic Separation

Farid Aghilasse Mansour, Malek Ould Hamou, Amira Merchichi, and Nabil Babahoum

Abstract−A process involving coal-based direct reduction followed by wet low-intensity magnetic separation is presented in this paper with the objective of promoting the Fe content and reducing the P assay of phosphorus-rich oolitic iron ore. A final direct reduced iron powder assaying 92.5 wt% Fe and 0.2 wt% P at a recovery rate of 95.9% was obtained when a mixture of ore-coal-CaO was reduced at 1200°C during 60 min in the presence of 7.5% sodium sulfate. In addition, microscopic analyses reported that the oolitic texture was completely destroyed, and most of the iron occurred in the metallic state. These findings suggest the ease utilisation of the ore mined from Gara Djebilet in the steelmaking industry as a substitute to scrap steel in electric arc furnace.

***Keywords*− Direct reduction, Gara Djebilet, magnetic separation, oolitic iron ore.**

NOMENCLATURE

AAS	Absorption atomic spectroscopy
BT	Billion Tones.
CBDR	Coal-based direct reduction.
DRI	Direct reduced iron
EAF	Electric Arc Furnace.
EDS	Energy dispersive spectroscopy
SEM	Scanning electron microscopy.
WLIMS	Wet low-intensity magnetic separation.
XRF	X-ray fluorescence.

I. INTRODUCTION

Owing to the depletion of easy-to-process iron resources and the rapid increase in need for iron in steelmaking industry, the iron extraction from various refractory iron ores has become a focus of research [1]. One of the most important occurrences of refractory iron ores is the oolitic iron ore [2]. This type distributes in Algeria as plentiful deposits of huge reserves such Gara Djebilet (5 Bt) and Mecheri Abdelaziz (3 Bt) [3]. Gara Djebilet has not yet been commercially exploited since its processing has run into the inability of iron oxides beneficiation by the conventional routes due to many problems related to its complex texture resulted from the finely dissemination of iron minerals in those of gangue and the presence of phosphorus in excessive content [4]. Therefore, current attentions are turned towards the pyrometallurgical methods as an alternative to the hydrometallurgical ones for iron extraction and phosphorus removal. The coal-based direct reduction (CBDR) prior to EAF is a promising route for iron recovery by using coal as reductant at temperatures below the melting point of iron [5]. During this process, the iron oxides are reduced to metallic iron with grain growth and then recovered by subsequent grinding and wet low-intensity magnetic separation (WLIMS) [6]. In this study, ironstone samples sourced from Gara Djebilet underwent various treatment experiments including WLIMS, CBDR-WLIMS without any additives, and CBDR-WLIMS in the presence of Na_2SO_4. The concentrate product of each experiment is subjected to chemical analyses to assay their iron and phosphorus content. In addition, SEM-EDS were performed to study the morphology and microstructure of the DRI as well as identify local composition.

II. MATERIALS

The ironstone samples were collected from Gara Djebilet field which is located in the Tindouf province of Algeria. Chemical composition and Phase of a homogenized sample from Gara Djebilet West is presented in Table I and Fig. 1, respectively.

Table I.
CHEMICAL COMPOSITION OF THE RAW ORE (WT%)

SiO_2	6.45	FeO	13.0
Al_2O_3	4.90	P_2O_5	1.80
Fe_2O_3	64.5	Loss On Ignition (LOI)	7.35

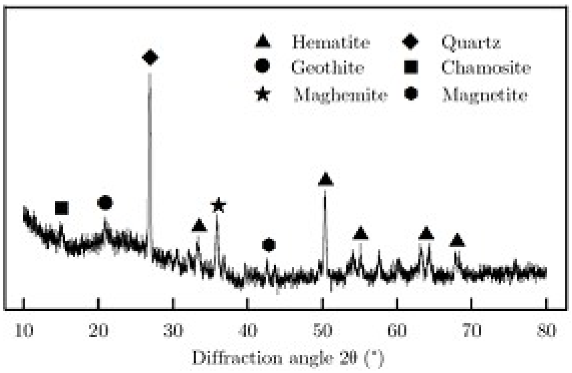

Fig. 1: XRD pattern of raw ore

The total iron grade amounts to 55.30 wt%. However, the P content is as high as 0.8 wt%. Fig. 2 presents the microstructure of selected ironstone observed under a reflected light microscope. Obviously, the typical oolitic texture is generated of ooids with alternating hematite, goethite, and chamosite

Manuscript received November 2, 2021; revised December 27, 2022.

F. A. Mansour, M. Ould Hamou and A. Merchichi are with the Mining Engineering Department, Ecole Nationale Polytechnique, Algiers, ALGERIA. (e-mails: farid_aghilasse.mansour@g.enp.edu.dz, malek.ould_hamou@g.enp.edu.dz, amira.merchichi@g.enp.edu.dz)

N. Babahoum is with SONATRACH Inc., ALGERIA. (email: nabil.babahoum@g.enp.edu.dz)

Digital Object Identifier (DOI): 10.53907/enpesj.v2i2.66

laminae that are embedded in chamositic matrix.

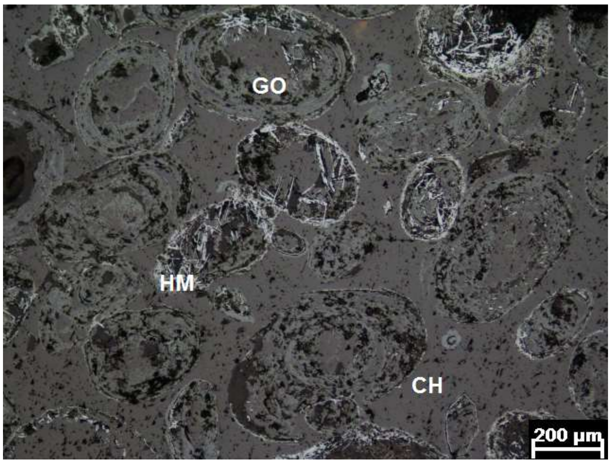

Fig. 2: Photomicrograph of the raw ore
CH—Chamosite; GO—Goethite; HM—Hematite

The bituminous coal used as reductant is taken from Bechar province of Algeria. Its components are reported in Table. II. The burnt lime (CaO) used as flux, and the additive of sodium sulfate (Na_2SO_4), are of reagent grade (AR) and their particle size is less than 74 µm.

Table II.
PROXIMATE ANALYSIS OF COAL (%)

Fixed carbon	Ash	Volatile matter	Moisture
49.5	6.20	45.3	14.9

III. METHODS

Three experiments were designed to investigate the efficiency of each route in iron recovery and phosphorus removal. The iron ore and coal were crushed separately to 100% less than 1 mm using a laboratory jaw crusher. For requirement to the first experiment, a certain amount (60 g) was taken from the crushed raw ore and milled to 80% less than 74 µm using a planetary ball mill (Retsch pm100). Then, a sample weighting 20 g was subsequently slurried to 20wt% solids by weight (20 g powder by 100 mL distilled water) and subjected to WLIMS through a Davis tube (KHD Humboldt Wedag International AG GmbH, Germany) under a magnetic field intensity of 0.14 T. The main operating variables are the wash-water flowrate which is set at 2.5 $L \cdot min^{-1}$ and the running period of time which is set to be 10 minutes. While the conception variables are the glass tube slop which is set at 45° from the horizontal and the agitation cycles which is set at 60 cycles per minute. Regarding the remaining trials, the rest of the raw ore was mixed with coal and CaO according to specific proportions. Each experiment requires 20 g iron ore, 15 g coal, and 1 g CaO. An additional amount of 1.5 g Na_2SO_4 was added to the mixture during the last experiment. Next, the mixtures were charged into heat-resistance graphite crucibles, and then reduced inside a high-temperature electric resistance muffle furnace at 1200°C for 60 min. Once the reduction achieved, the mixtures were withdrawn from the furnace and cooled down to room temperature under an air-isolated environment. After that, the samples were milled to 80% less than 74 µm using a vibratory disc mill. Then, a representative sample weighting 20 g taken from each milled product was slurried to 20 wt% solids by weight and subjected to WLIMS through the aforementioned device under the same conditions. The concentrate produced from each experiment was subjected to chemical analyses to assay their iron and phosphorus content using both XRF and AAS methods. Moreover, both reduced powder and DRI were subjected to SEM-EDS analyses to investigate their microstructure and identify their local composition.

IV. RESULTS AND DISCUSSION

The outputs of WLIMS and the chemical composition of the magnetic material are summarised in the Table III. The Fe Content (TFe) amounts to 72.80wt% whereas the P content is as high as 0.5wt%. Despite the efficiency of WLIMS in recovery of iron, its uncompetitive in dephosphorisation is evident.

Table III.
RESULTS OF WLIMS FOR THE FIRST TEST

Product	Yield (%)	Fe content (wt%)	Fe recovery (%)
Concentrate	51.35	72.80	67.60
Tailing	48.65	36.82	32.40
Total	100	-	100

For the experiment involving CBDR-WLIMS without any additives, the outputs of the WLIMS are reported in Table. IV. The chemical analyses of the DRI using AAS reported that the TFe amounts to 79.20 wt% whereas the P content reaches a value as high as 1.25 wt%. Obviously, subsequent grinding and WLIMS obtain a phosphorus-rich DRI. This is because the reduction, at this high temperature and for a long period, causes the dissolution of the elemental phosphorus into the hot metallic iron (Fe), rather than emitting to the atmosphere and generating the Fe_xP alloy. The latter is then turned towards the concentrates during WLIMS [7].

Table IV.
RESULTS OF WLIMS FOR THE SECOND TEST

Product	Yield (%)	Fe content (wt%)	Fe recovery (%)
Concentrate	68.35	81.20	92.5
Tailing	31.65	14.21	07.5
Total	100	-	100

For the experiment involving CBDR-WLIMS in the presence of 7.5% Na_2SO_4, the outputs are presented in Table. V. The TFe amounts to 93.5wt% while the P content is 0.2wt%.

Table V.
RESULTS OF WLIMS FOR THE THIRD TEST

Product	Yield (%)	Fe content (wt%)	Fe recovery (%)
Concentrate	78.65	93.50	97.40
Tailing	21.35	09.19	02.60
Total	100	-	100

It is clear that the Fe-P separation is intensified in the presence of Na_2SO_4. The microstructure and composition of the DRI produced during the presence of 7.5% Na_2SO_4 was investigated using SEM-EDS analysis and the result is presented in Fig. 3. The EDS analysis of the spot indicated in the figure reported that iron is the main element present in the DRI suggesting that a nearly monophased material has been acquired through the third test.

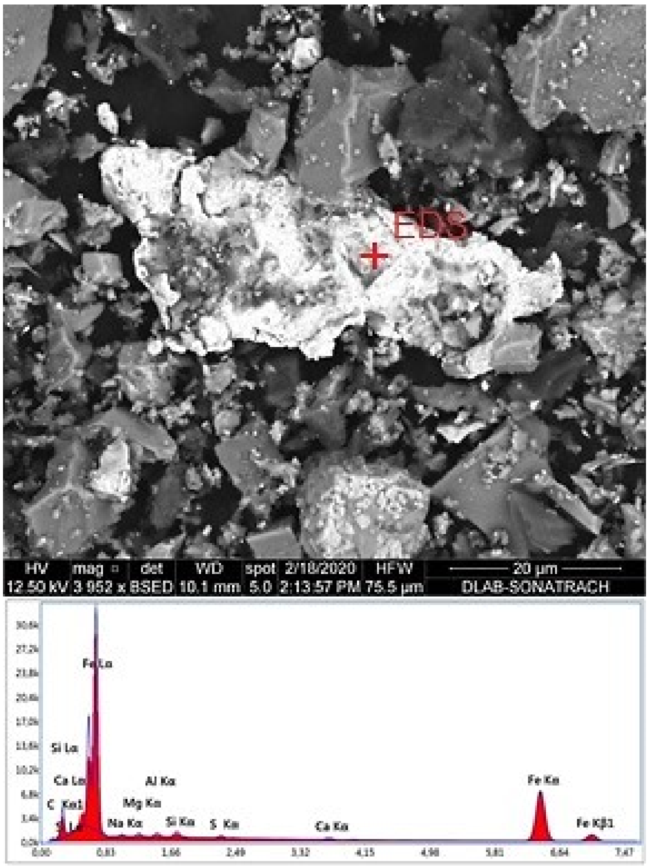

Fig. 3. Microstructure and EDS measurement of the magnetic material output of the third experiment

However, there was found few amounts of Al, Ca, Mg, Si, and S which are part of some fine size impurities such as fayalite Fe_2SiO_4, hercynite $FeAl_2O_4$, and troïlite FeS, which are turned into, concentrates along with iron grains via the magnetic reunion phenomena (Table. VI) [8].

Table VI.
EDS QUANTITATIVE ANALYSIS DATA OF THE SELECTED SPOT FROM THE MAGNETIC MATERIAL OUTPUT OF THE THIRD TEST

Elt.	%mass	%atomic	Elt.	%mass	%atomic
C	1.57	6.43	Si	0.75	1.71
O	1.62	5.08	P	0.21	0.33
Na	0.33	0.18	S	0.62	0.98
Mg	0.27	0.14	Ca	0.35	0.11
Al	0.69	1.50	Fe	93.59	84.15

V. CONCLUSION

Throughout this study, a series of experiments were carried out for iron enrichment and phosphorus removal from Gara Djebilet ironstone samples. A magnetic product assaying 72.5 wt% Fe and 0.5 wt% P was acquired by WLIMS of -74 µm raw ore. This material is not suitable for steelmaking industry via the blast furnace route due to its high phosphorus content. Without any dephosphorisation agent, a DRI assaying 81.2 wt% Fe and 0.25 wt% P was obtained by WLIMS of a reduced ore-coal-CaO mixture at 1200°C for 60 min. This high phosphorus-containing metallic iron powder could then be converted to steel by a steelmaking duplex process, and the phosphorus-rich steelmaking slag containing more than 10wt% P_2O_5 could be used as phosphate fertilizer [9]. In the presence of a dephosphorisation agent, a DRI assaying 93.5 wt% Fe and 0.2 wt% P was acquired via WLIMS of a reduced ore-coal-CaO-Na_2SO_4 mixture at 1200°C for 60 min. This product is suitable for steelmaking industry as substitute to scrap steel in EAF.

REFERENCES

[1] Y. Sun et al., "Size distribution behavior of metallic iron particles in coal-based reduction products of an oolitic iron ore," Min. Proc. Ext. Met. Rev., vol. 36, no. 4, pp. 249-257, Aug 2015, 10.1080/08827508.2014.955611.

[2] Y. Sun et al., "Recovery of iron from high phosphorus oolitic iron ore using coal-based reduction followed by magnetic separation," Int. J. Min. Met. Mater., vol. 20, no. 5, pp. 411-419, Mar 2013, 10.1007/s12613-013-0744-1.

[3] S. Guerrak, "Geology of the Early Devonian oolitic iron ore of the Gara Djebilet Field, Saharan Platform, Algeria," Ore Geol. Rev., vol. 3, no. 4, pp. 333-358, Aug 1988, 10.1016/0169-1368(88)90026-1.

[4] J. Gao et al., "Separation of P phase and Fe phase in high phosphorus oolitic iron ore by ultrafine grinding and gaseous reduction in a rotary furnace," Metall. Mater. Trans. B, vol. 46, no. 5, pp. 2180-2189, Jul 2015, 10.1007/s11663-015-0400-4.

[5] J. Kou et al., "Coal-based direct reduction and magnetic separation of lump hematite ore," Miner. Metall. Proc., vol. 31, no. 3, pp. 150-161, Aug 2014, 10.1007/BF03402272.

[6] W. Yu et al., "Effect of coal type on the reduction and magnetic separation of a high-phosphorus oolitic hematite ore," ISIJ Inter., vol. 55, no. 3, pp. 536-543, Dec 2015, 10.2355/isijinternational.55.536.

[7] J. Cha et al., "Distribution behavior of phosphorus and metallization of iron oxide in carbothermic reduction of high-phosphorus iron ore," Metall. Mater. Trans. B, vol. 46, no. 5, pp. 2165-2179, Jun 2015, 10.1007/s11663-015-0399-6.

[8] Y. Zhang et al., "Recovery of iron from cyanide tailings with reduction roasting-water leaching followed by magnetic separation," J. Hazard. Mater., vol. 213-214, no. pp. 167-174, Apr 2012, 10.1016/j.jhazmat.2012.01.076.

[9] G. F. Li et al., "Enrichment of phosphorus in reduced iron during coal based reduction of high phosphorus-containing oolitic hematite ore," Ironmaking & Steelmaking, vol. 43, no. 3, pp. 163-170, Mar 2016, 10.1179/1743281214Y.0000000262.

Farid Aghilasse Mansour (November 29, 1989 in Mahdia, Tiaret). He received the degrees of Ingénieur d'Etat and Master en Génie Minier from the Ecole Nationale polytechnique in 2014. Currently, he is a PhD student in Génie Minier at the Ecole Nationale Polytechnique of Algiers, Algeria.

Malek Ould Hamou is a professor at Ecole Nationale Polytechnique. He was the head of mining engineering department and the director of the mining engineering laboratory of the same establishment. His research interests are in mineralurgy, bioprocessing and mining environment.

Amira Merchichi is an assistant professor at Ecole Nationale Polytechnique since 2014. Her research interests are in mining environment, mineral processing, biomining.

Nabil Babahoum received the degree of Engineer and Master's degree in 2014 and Ph.D in 2022 in mining engineering from Ecole Nationale Polytechnique. He is a WellSite Geologist at SONATRACH since 2015.